



Project no. TIP5-CT-2006-031415

INNOTRACK

Integrated Project (IP)

Thematic Priority 6: Sustainable Development, Global Change and Ecosystems

D4.4.2 - Operational evaluation of an inspection demonstrator (phase 1: laboratory and static tests)

Due date of deliverable: 2008/06/30

Actual submission date: 2009/02/05

Start date of project: 1 September 2006

Duration: 36 months

Organisation name of lead contractor for this deliverable: SNCF

Revision: Final

Project co-funded by the European Commission within the Sixth Framework Programme (2002-2006)		
Dissemination Level		
PU	Public	X
PP	Restricted to other programme participants (including the Commission Services)	
RE	Restricted to a group specified by the consortium (including the Commission Services)	
CO	Confidential, only for members of the consortium (including the Commission Services)	

Table of Contents

Table of figures	3
Glossary	7
1. Executive Summary	9
2. Introduction	10
3. Main section	11
3.1 Description of tests performed.....	11
3.1.1 <i>Practical requirements</i>	11
3.1.2 <i>Samples</i>	12
3.1.3 <i>Details of new experimental methods performed on rail defects</i>	13
3.1.4 <i>Comparison of results for common test rails</i>	83
3.1.5 <i>Applicability of methods for industrial exploitation</i>	84
3.2 Mapping to infrastructure assets	86
4. Conclusions	93
5. Bibliography	94
6. Annexes	95
6.1 APPENDIX 1- Laser acoustics	95
6.1.1 <i>Principle of sound excitation</i>	95
6.1.2 <i>Methods of defects detection</i>	97
6.1.3 <i>Optical methods for ultrasound detection</i>	100
6.1.4 <i>Optical detection of ultrasound for industrial applications.</i>	107
6.1.5 <i>Laser ultrasonics for rails testing; prototypes</i>	111
6.1.6 <i>Bibliography on laser ultrasonics study</i>	113
6.2 APPENDIX 2 – SICOR	114
6.3 APPENDIX 3– ProRail requirements list	119

Table of figures

Figure 1 – Demonstration of skew angle and tilt angle	8
Figure 2 – Shadowing effect.....	11
Figure 3 – Illustration of the current method of characterisation	11
Figure 4 – Results of numerical simulations.....	12
Figure 5 - Photos of Squats. Examples of surface appearance (dark spot) and transverse crack development	13
Figure 6 - Illustration of the development of Squat.....	14
Figure 7 - Measurement of the length of the squat	14
Figure 8 - Illustration of the inspected area	15
Figure 9 - Illustration of the depth measurement.....	15
Figure 10 - Simulation of the depth measurement	16
Figure 11 - Illustration of the shadowing effect.....	16
Figure 12 - Simulation of the shadowing effect	17
Figure 13 - Illustration of the skewed effect.....	17
Figure 14 - Simulation on a skewed defect.	18
Figure 15 - Description of the angular scanning.....	18
Figure 16 - Simulation of ultrasonic fields radiated by the matrix phased array probe	19
Figure 17 - Description of defects defined in CIVA.	20
Figure 18 - Simulation of defect response– Result on the no skewed defect	21
Figure 19 - Simulation of defect response– Result on the 35°-skewed defect	21
Figure 20 - Description of the acquisition.	22
Figure 21 - Acquisition on the 0°-skewed defect – Bscan angular scan/time.	23
Figure 22 - Acquisition on the 0°-skewed defect – Cscan extracted from the 0°-skew shot.....	24
Figure 23 - Acquisition on the 35°-skewed defect – Bscan angular scan/time.	24
Figure 24 - Acquisition on the 35°-skewed defect – Cscan extracted from the 45°-skew shot.....	25
Figure 25 - Photo of the rail CER310-07	25
Figure 26 - Acquisition on sample 310-07 – C-scan and B-scans extracted from the 0°-skew shot.	26
Figure 27 - Acquisition on sample 310-07 –Comparison between the 0°-skew shot and the cumulated Cscan of all shots.....	26
Figure 28 - Acquisition on sample 310-07 –Comparison between the 0°-skew shot and the cumulated Cscan of all shots.....	27
Figure 29 - Photo of the rail CER295-07	27
Figure 30 - Acquisition on sample CER295-07 –Comparison between the 0°-skew shot and the cumulated C-scan of all shots.	28
Figure 31 - Principle of the transmission method	28
Figure 32 - Electronic commutation – Examples of sequences	29
Figure 33 - Simulation of fields received by the receptor.	30
Figure 34 - Calibration of the through transmission method	31
Figure 35 - Description of the mechanical displacements of the probes.....	31
Figure 36 - Acquisition in through transmission technique before surface preparation.	32
Figure 37 - Acquisition in through transmission technique before after surface preparation (paint removed)	33
Figure 38 - Photos of head checking. Examples of surface appearance and transverse crack development	34
Figure 39 - Illustration of the development of Head checking	34
Figure 40 - Illustration of the measurement of the depth.....	35

Figure 41 - Illustration of the shadowing effect.....	36
Figure 42 - Illustration of the skew effect.....	36
Figure 43 - Description of the position of the probe	37
Figure 44 - Description of the electronic scanning	38
Figure 45 - Photo of the rail CER212-04	38
Figure 46 - Acquisition on sample CER212-04. Cscan and Bscan views for the 45°-shot/ rail axis.....	39
Figure 47 - Acquisition on sample CER212-04. C-scan (Time limited in depth) and B-scan views for the -10°-shot/ rail axis.....	41
Figure 48 - Photo of the rail 3506A.....	41
Figure 49 - Acquisition on sample 3506A. Cscan and Bscan views for the 45°-shot/ rail axis	42
Figure 50. Acquisition on sample 3506A. C-scan (Time limited in depth) and B-scan views for the 25°-shot/ rail axis.....	43
Figure 51 - Photograph and picture of the Transmit-Receive probe	44
Figure 52 - Photograph and picture of the magnetic flux leakage probe	44
Figure 53 - Photograph of the flexible probe and evaluation in the case of the inspection of the gauge corner	45
Figure 54 - Eddy current signal obtained at 290Hz with transmit-receive probe in the case of the detection of the flaws located in the rail 1	46
Figure 55 - Eddy current signal obtained at 290Hz with magnetic flux leakage probe in the case of the detection of the flaws located in the rail 1.....	46
Figure 56 - Eddy current signal obtained at 290Hz with magnetic flux leakage probe in the case of the detection of the flaws located in rail 3.....	47
Figure 57 - CSCAN mapping obtained at 2MHz for eddy current examination of the cracked area of the 3506A rail mock-up.....	47
Figure 58 - CSCAN mapping obtained at 2MHz for eddy current examination of the cracked area of the CER 212_04 rail mock-up	48
Figure 59 - Experimental set-up for the study of defects in rail.....	49
Figure 60 - Configuration of defects on the rail (Table 61).....	49
Figure 61 – A. Surface wave. The width of line source (mm) is on the right part of each curve / B. Corresponding spectra normalized on their maximum.....	50
Figure 62 - Surface wave on the rail with 3 (A) and 6 mm (B) deep vertical defect. The width of the line-source in mm is marked on the right side of each curve	50
Figure 63 - First (A) and second (B) configuration of the defect probing by the surface wave	51
Figure 64 - Surface wave on the rail with 3 (A) and 6 mm (B) deep defect (45 deg., first configuration). The width of the line-source in mm is marked on the right side of each curve.....	51
Figure 65 - Surface wave on the rail with 3 (A) and 6 mm (B) deep defect (45 deg, second configuration). The width of the line-source in mm is marked on the right side of each curve	52
Figure 66 -Acoustic pulses in rail without (1) and with defect (2). The echo from the defect is marked as L. 52	
Figure 67 - Definition of field directions and co-ordinate system used in ACFM.....	53
Figure 68 - a) The ACFM walking stick, b) the under-side of the walking stick.....	55
Figure 69 - Optical micrograph of a typical RCF crack10.....	55
Figure 70 - The spinning rail rig at Birmingham University.....	56
Figure 71 - Plan view schematic of sample rails and induced defects (vd = vertical depth, va = vertical angle, ha = horizontal angle)	57
Figure 72 - ACFM C-scan obtained for rail 8.....	58
Figure 73 - ACFM C-scan for test rail 1	59
Figure 74 - ACFM C-scan for test rail 2.....	60
Figure 75 - ACFM C-scan for test rail 3.....	61

Figure 76 - ACFM C-scan for test rail 4.....	62
Figure 77 - ACFM C-scan for test rail 5.....	63
Figure 78 - ACFM C-scan for test rail 6.....	64
Figure 79 - ACFM C-scan for test rail 7.....	65
Figure 80 - C-scan for three railhead pieces containing actual RCF cracking.....	66
Figure 81 - C-scan for railhead piece containing actual RCF damage.....	67
Figure 82 - Photographs of samples containing actual RCF cracking tested with the ACFM walking stick array.....	68
Figure 83 - Rotary test piece with spark eroded notches.....	69
Figure 84 - Experimental configuration for the turning lathe tests.....	69
Figure 85 - ACFM data at 20.25km/h and 121.5km/h at a lift-off of 0.8mm.....	70
Figure 86 - ACFM signal with increasing lift-off at 81km/h.....	71
Figure 87 - Normalised ACFM plots showing the effect of increasing lift-off.....	72
Figure 88 - Experimental setup for the spinning rail rig tests. The ACFM probe can be seen in the foreground.....	73
Figure 89 - An alternative view of the experimental setup for the spinning rail rig tests.....	73
Figure 90 - Probe lift-off variation for the spinning rail rig tests.....	74
Figure 91 - Plot showing the ACFM signal for test rails #3 and #5.....	75
Figure 92 - Plot showing the ACFM signal for test rails #3 and #5.....	76
Figure 93 - Plot showing the ACFM signal for test rail #8.....	77
Figure 94 - Schematic showing the EMAT experimental setup.....	78
Figure 95 - EMATs: transmitted ultrasound on Rail 1. (a) Frequency B-scan, (b) two A-scans, (c) the change in normalised Rayleigh-wave amplitude during the scan.....	80
Figure 96 - Rail 4 (clustered defects). (a) Shows a frequency B-Scan, (b) shows the normalised signal amplitude, and (c) shows normalised FFTs in the cracked regions.....	81
Figure 97 - Rail 6 (two angles). (a) Frequency B-Scan made up of normalised FFTs; (b) normalised signal amplitude.....	82
Figure 98 - Layout of the current software NAVIRE platform.....	86
Figure 99 - Display of infrastructure features (tunnels in a selected area near Marseille).....	87
Figure 100 - Satellite view of selected infrastructure features (Figure 99).....	88
Figure 101 - Display of railway infrastructure features (stations).....	89
Figure 102 - Hybrid satellite image of the same area (L'Estaque station near Marseille).....	90
Figure 103 - Examples of other railway cases (1/2).....	91
Figure 104 - Examples of other railway cases (2/2).....	92
Figure 105 - Sound pulse excitation by thermoelastic (A) and ablation (B) mechanisms [8].....	96
Figure 106 - The diagram of sound excitation by a laser line source. A – thermoelastic; B – ablation regimes [8].....	96
Figure 107 - Time-of-flight technique for defects detection. P, S, R are direct compression, shear and Rayleigh waves; PP is P wave reflected as compression wave, dPP is P wave diffracted as compression wave (other details are in the text of the review) [8].....	97
Figure 108 - The experimental set-up for the detection of defects based on the shadowing of ultrasound beam [11].....	98
Figure 109 - Near and far shadow zones on the surface due to the blocking of ultrasonic rays.....	99
Figure 110 - Shadow pattern provided by a transverse defect in rail [11].....	100
Figure 111 - Optical heterodyne interferometer [14].....	101
Figure 112 - Long-path interferometer [8].....	102
Figure 113 - The design of Fabry-Pérot interferometer [14].....	103

Figure 114 - The ultrasonic frequency response of a Fabry-Pérot interferometer	103
Figure 115 - Set-up of a heterodyne interferometer with Double Phase Conjugate Mirror [17].....	104
Figure 116 - A: Optical design of a multi-channel quadrature interferometer. f1 is a collimation lens. B: comparison of quadrature interferometers with 1, 4 and 25 detectors [18]......	105
Figure 117 - Beam deflection technique of ultrasound detection [15]	105
Figure 118 - PIE-830 optical set-up [21].....	106
Figure 119 - Attenuation of 15 MHz ultrasound and Austenite of the steel vs. the temperature [29].....	108
Figure 120 - Ultrasound velocity in steel vs. the temperature [31]	109
Figure 121 - The schematic of laser ultrasonic equipment used at Algoma Steel company [32]	109
Figure 122 - The thickness profile of pipe wall [32]	110
Figure 123 - SOPRANO system [25].....	110
Figure 124 - Laser-Air Hybrid Ultrasonic (LAHU) system [33].....	111
Figure 125 - Basic principle of LURI [35].....	112
Figure 126 - Optimised configurations of pump and probe for LURI system [35]	113
Figure 127 – Rail zones for ultrasonic inspection.....	119
Table 1 – Samples.....	13
Table 2 - Main probe parameters.	22
Table 3 - Main probe parameters.	29
Table 4 - EC signal magnitude values obtained for the detection of flaws in rail 1 in the case of transmit-receive and magnetic flux leakage probes	46
Table 5 EC signal magnitude values obtained for the detection of flaws in rail 3 in the case of magnetic flux leakage probe	47
Table 6 - Parameters of the defects	49
Table 7 - Actual and ACFM calculated depths for the pocket-shaped artificial defects	57
Table 8 – Normalised results of innovative techniques	83
Table 9 –Capability table	84
Table 10 - Comparison of ultrasound detection systems	107
Table 11 - Commercially available interferometric systems	108

Glossary

Abbreviation/acronym	Description
A-Scan	A method of data presentation utilising a horizontal baseline that indicates distance, or time , and a vertical deflection from the bas line which indicates amplitude (ASTM)
ACFM	Alternating Current Frequency Method
B-Scan	A means of ultrasonic data presentation which displays a cross section of the specimen indicating the approximate length (as detected per scan) of reflectors and their relative position (ASTM).
UNIBHAM	University of Birmingham
C-Scan	An ultrasonic data presentation which provides a plain view of the test object, and discontinuities therein (ASTM)
CEA	Atomic Energy Commission
CER	(Centre d'Expertise des Rails) Acronym defined by SNCF for internal use to identify its own samples
CIVA	Software to analyse non destructive testing results
EC	Eddy Current
Echo	Acoustic reflection of an emitted signal
EMAT	Electro-Magnetic Acoustic Transducer
GCC	Gauge Corner Cracking
GERIM	A common platform for non destructive testing and evaluation
Head Checking	Cracks on the rail head gauge corner (see GCC)
LMP	Mechanical and Physics Laboratory at the University of Bordeaux
NDE	Non destructive evaluation
NDT	Non destructive testing
P Wave	Bulk compressive, acoustic wave
Phased Array	An electronically driven collection of acoustic transducers arranged in a common matrix
R Wave	Surface propagating Rayleigh waves
RCF	Rolling Contact Fatigue
S Wave	Bulk shear acoustic
Shadow Effect	The masking of a shorter crack by a longer crack
Skew angle	Following sketch describes skew and tilt angles
Squat	Cracks on the rail head which generally occur in alignment (see RCF)
Time of Flight	Elapsed time between transmission and reception of a signal
Tilt angle	cf. skew angle

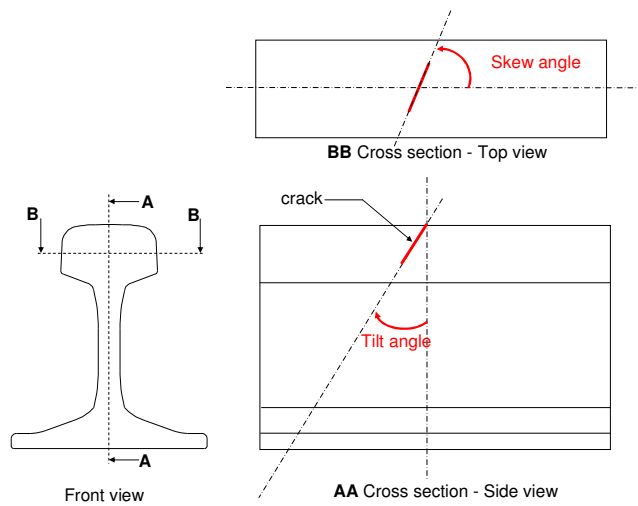


Figure 1 – Demonstration of skew angle and tilt angle

1. Executive Summary

Rails are periodically surveyed by non-destructive manual or train-borne inspections in order to detect crack initiation and to ensure that crack expansion remains within a preset threshold. These periodic surveys are mandatory to maintain the required level of railway safety. As they tend to be more frequent on high standard infrastructure (higher loads or speed), rail inspection techniques and strategies are a challenging issue for future infrastructure maintenance.

The cost of these routine control operations is fairly high for various reasons:

- many manual operations are required (either because no inspection train is available, or because post inspection crack characterisation and periodic control are carried out manually);
- many hand operations are necessary to transfer the results from site inspection to remote databases and vice-versa, resulting in commonly observed inaccuracies in defect positioning;
- track availability is reduced because train-borne inspections can only be performed at reduced speeds, causing limitations to track availability.

The objective of improving rail inspection methods thus strongly contributes to the overall aim of reducing infrastructure maintenance costs.

Future inspection processes should also guarantee the highest level of security for operators and, if possible, improve operating conditions (exposure to weather, communication with remote databases, defect positioning) as well as improving environmental aspects (use of fluid coupling products).

To better respond to these objectives, it is necessary to evaluate and use the best relevant techniques currently available on an inspection demonstrator, which will be tested in the last phase of this work package.

2. Introduction

The current use of specialised inspection cars or specific trolleys is the main difficulty which this task should try to overcome. The ultimate objective, which is currently unachievable, would be to operate internal rail inspection from revenue trains. This would reduce overall track occupancy as well as improve detection and monitoring because of a higher inspection periodicity, possibly at a lower cost. This process is already applied to track geometry measurements by some railway infrastructure operators.

The existing proven methods are based upon non-destructive ultrasonic techniques with sliding probes. These techniques suffer from two drawbacks:

- probes are generally focused to one point, so that only a part of the rail (the railhead) is properly scanned by the acoustic beam;
- the practical inspection speed is restricted to approximately 50 or 60 km/h, due to coupling and also to avoid probe damages caused by shocks between the probe-bearer and the rail at higher speeds.

In the first stage, numerical simulation methods will be used, which provide guidance for building probes which are best fitted to specific defects and defect locations (instead of try and fail methods with different probes). Along with these evaluations, static laboratory (GERIM platform) and dynamic simulation tests (University of Birmingham rolling rig) will be performed with artificial and real defects.

Different techniques will be used to overcome the existing drawbacks of industrial inspection techniques:

- phased arrays, to improve scanning of the railhead for any defect position;
- laser and eddy current to try to avoid the sliding probes.

In addition, information is included on a new technique being explored by Deutsche Bahn (a WP4.4 partner). Details of the "Speed Induced Current On Rails" (SICOR) method are included in Appendix 2

In the second stage, a track test will be performed using a trolley equipped with at least one of the techniques selected from the static tests in phase 1.

3. Main section

3.1 Description of tests performed

3.1.1 Practical requirements

The first practical requirement is to avoid two common phenomenon linked to the presence of successive defects, such as in this case (Figure 2) (common for surface defects), or inappropriate orientation of the acoustic beam, which is commonly observed when the defects tend to shift towards the rail side. This is generally the case for head-checking, but is often observed for internal defects, specifically in curves (Figure 3).

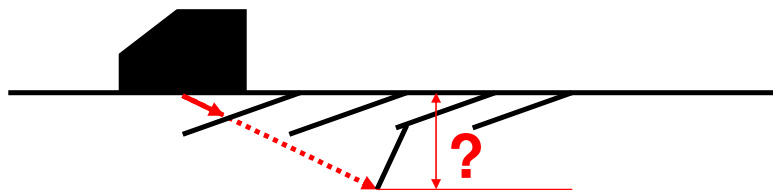


Figure 2 – Shadowing effect

Determination of the depth:

Depth is calculated from the crack tip

Shear waves-70°

Longitudinal waves-0°

The 70° probe will detect branches at longer range

The 70° probe will also detect shallow cracking (indications at less than 1.5 divisions on the time base)

With US there will be a loss of bottom echo with the 0° probe where cracks exist

U14

U3

The 10mm offset means that U14 will detect a defect located here before U3 can, giving more time for action.

Defects detected by both U14 and U3 are potentially very large

Anything found by U14 that has started from the main crack will

With these options in mind, the action required is based upon whether the crack is detected by

- U14 alone
- by both U3 and U14 and
- where the crack has started from.

Figure 3 – Illustration of the current method of characterisation

Numerical simulation will help in understanding the irregularities which rail or defect form and orientation may cause to direct acoustic propagation.

The following figures were obtained by such numerical simulations. As already outlined, simulation can help to gain an understanding of the inefficiency of existing inspection methods, at a reduced cost.

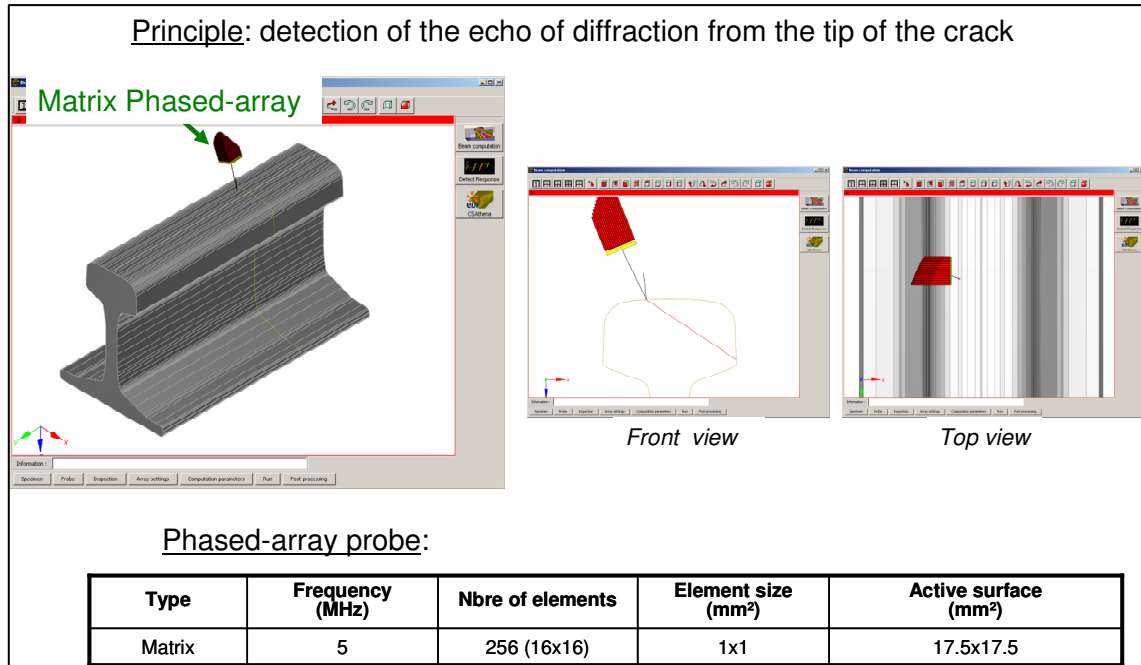


Figure 4 – Results of numerical simulations

Inspection time should be reduced as far as possible both for manual and for train-borne inspections.

Defect inspection has to be performed from the top of the rail, firstly because this part is always free for probe access and secondly because it does not suffer from corrosion. This enables good coupling at the probe/rail interface. Preliminary rail cleaning is not performed because it would cause additional delays in the case of manual inspection, or, in the case of train inspection, would require additional equipment which is not yet available.

The above operational constraints are only valid for production runs. In specific cases, with the relevant expertise, some of these constraints could be released.

3.1.2 Samples

Drawing to explain the following definitions

The dimension is given by the manufacturing process or by X ray or destructive inspection

Number	Manufactured/Real	Inclination	Skew	Shadow effect	Dimension	Industrial results
UNIBHAM 1	Manufactured	0°	0°	no	2, 4, 6, 10 mm	Not evaluated
UNIBHAM 3	Manufactured	25°	0°	no	2, 4, 6, 10 mm	Not evaluated
UNIBHAM 6	Manufactured	25°	35°	no	2, 4, 6, 10 mm	Not evaluated

Number	Manufactured/Real	Inclination	Skew	Shadow effect	Dimension	Industrial results
CER 310-07 (SNCF)	Real Squat	-	-	-	-	No detection of defect
CER 295-07 (SNCF)	Real Squat	-	-	-	-	No detection of defect
CER 212-04 (SNCF)	Real Head Checking	-	-	-	-	No detection of defect
3506A (SNCF)	Real Head Checking	-	-	-	-	No detection of defect

Table 1 – Samples

3.1.3 Details of new experimental methods performed on rail defects

Squat characterisation by UT-inspection

Description of the defect

The squat defect is rolling contact fatigue damage. It occurs on straight track and shallow curves and is initiated in the deformed metal on the running band. A dark spot can be found on the running surface and a small piece of material can become detached.



Figure 5 - Photos of Squats. Examples of surface appearance (dark spot) and transverse crack development

Sketches of Figure 6 show the development of the squat into the head. From the point of initiation, cracks first propagate at a shallow angle to the surface. When the shallow angled cracks reach a depth of about 3 to 5 mm they may propagate downwards into the head to form quasi-transverse cracks [1].

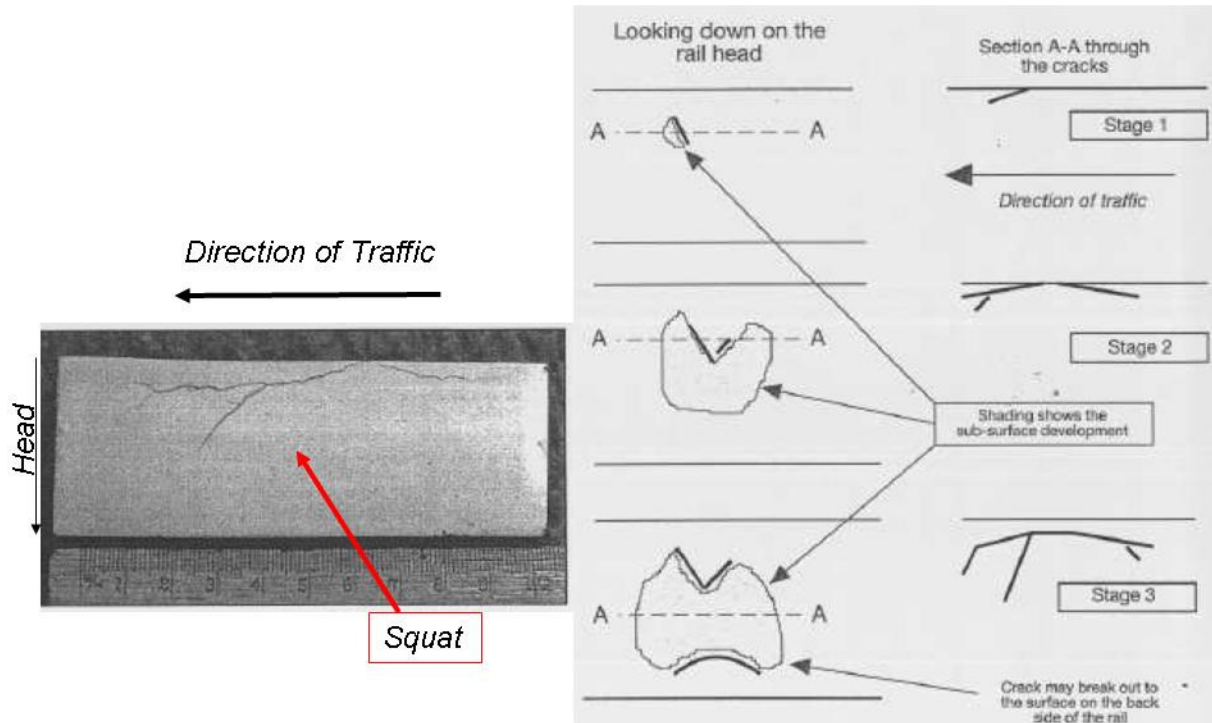


Figure 6 - Illustration of the development of Squat

Current method of characterisation

Length Measurement

The method of measurement of the length is illustrated on Figure 7. A 0°-longitudinal waves probe is used to detect the backwall echo from the rail foot. The probe is moved above the defect and the distance between the point where the backwall echo has decreased to its half amplitude (by 6 dB) and the point at which it regains half of its amplitude is considered as the length of the horizontal crack.

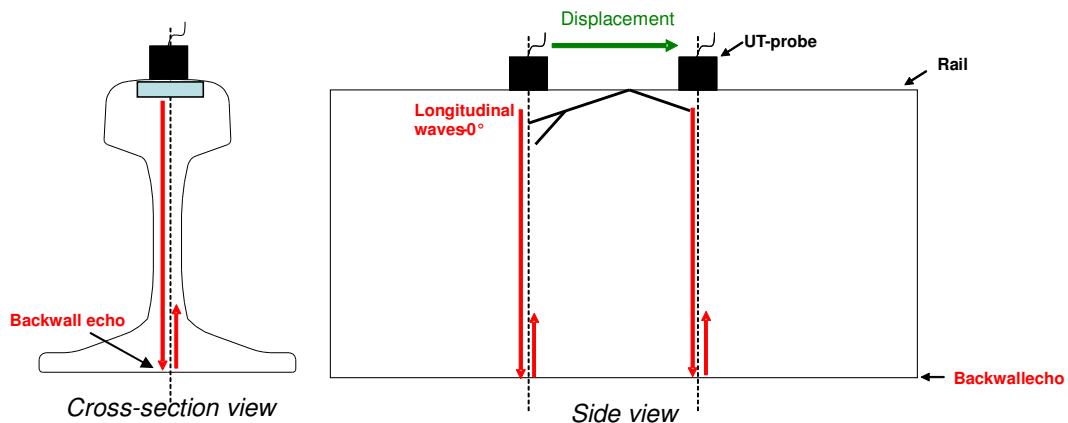


Figure 7 - Measurement of the length of the squat

As Figure 8 shows, one can note that the area of inspection is limited to the width of the web.

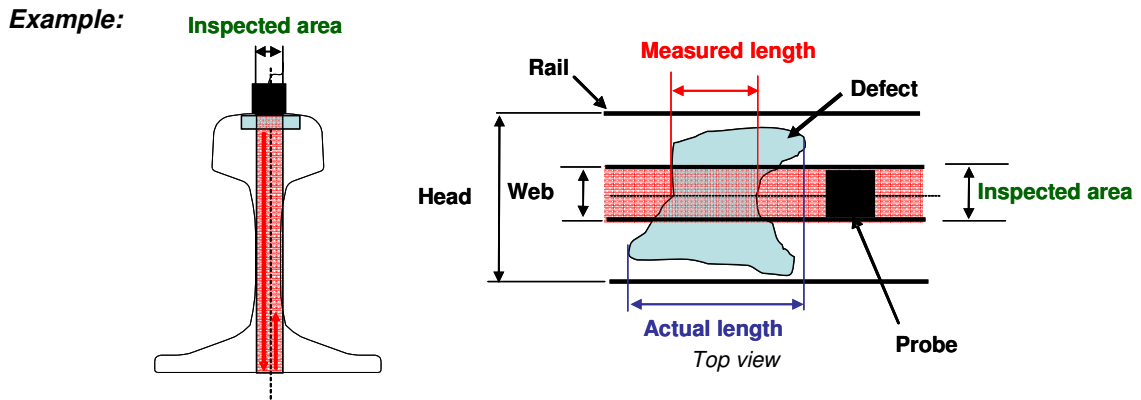


Figure 8 - Illustration of the inspected area

Depth Measurement: The depth of the defect is measured using a 68°-shear waves transducer. As illustrated in Figure 9, the depth is deduced from the point where the amplitude of the crack decreased by half its amplitude (by 6 dB). Inspection is made in both directions in the longitudinal plane.

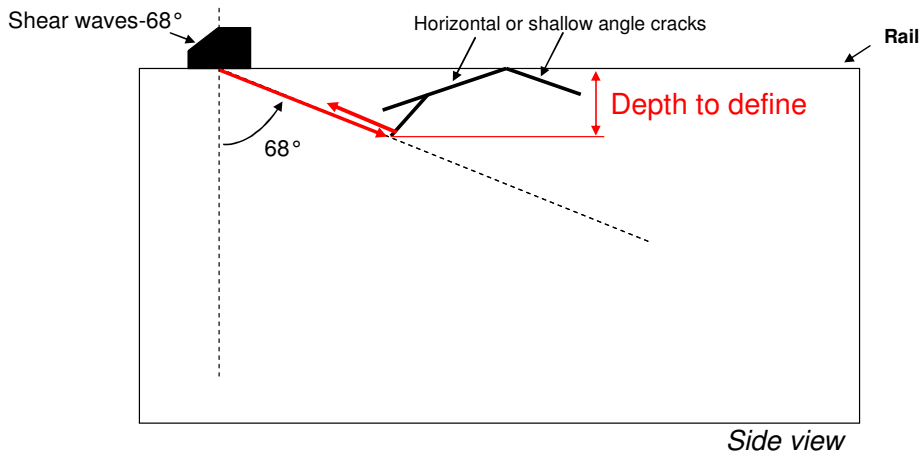


Figure 9 - Illustration of the depth measurement

This method was simulated using CIVA-software tools. Figure 10 shows an example of the existing method carried out to size a 25 mm-crack depth. We observe that in such a case, the depth can be correctly measured using this method.

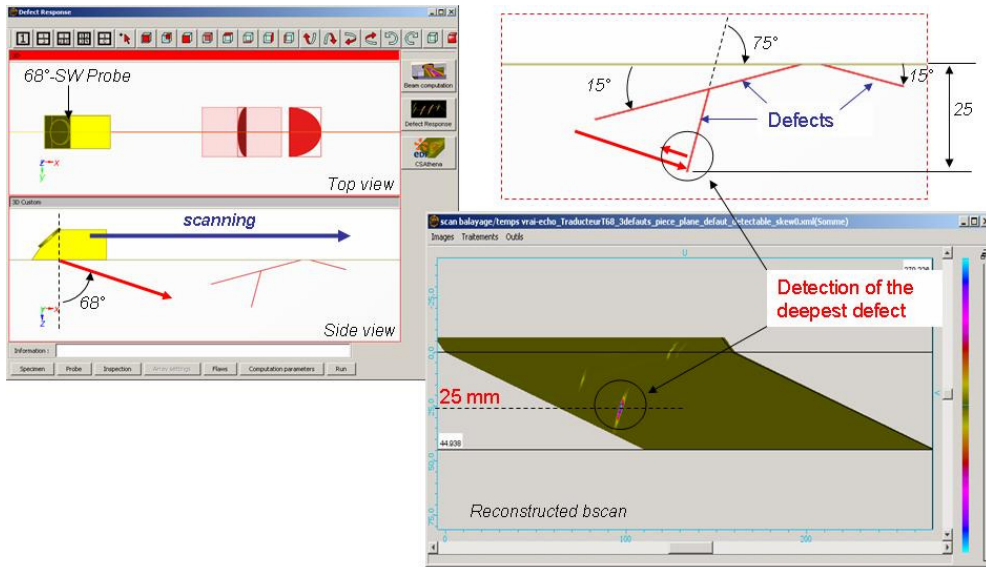


Figure 10 - Simulation of the depth measurement

Limitations of the existing measurement method

The method of depth measurement presents two main limitations according to the characteristics of the cracks: the shadowing effect and the skew effect.

Shadowing effect

Figure 11 illustrates a case in which a transverse crack is missed by the 68°-probe. A similar configuration was simulated with CIVA (Figure 12), where the shadowing effect is highlighted. The deepest crack cannot be detected due to the presence of the shallow angle defects. In such a case, the crack cannot be characterised in depth.

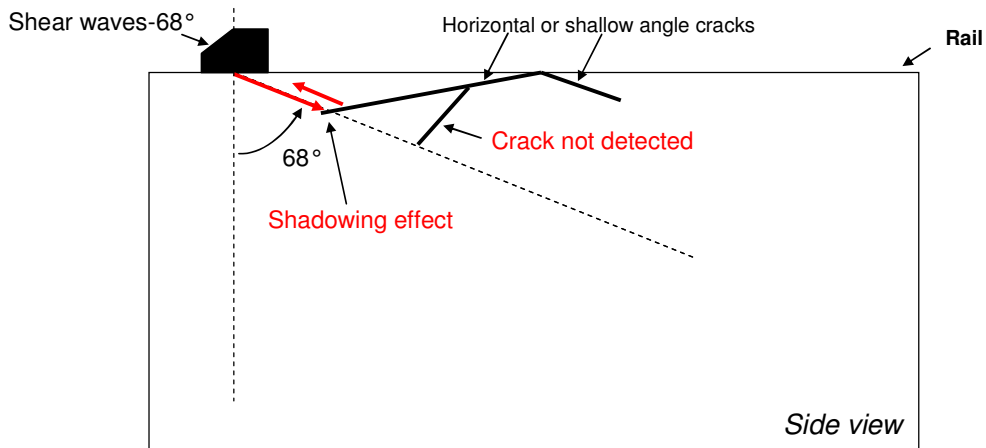


Figure 11 - Illustration of the shadowing effect

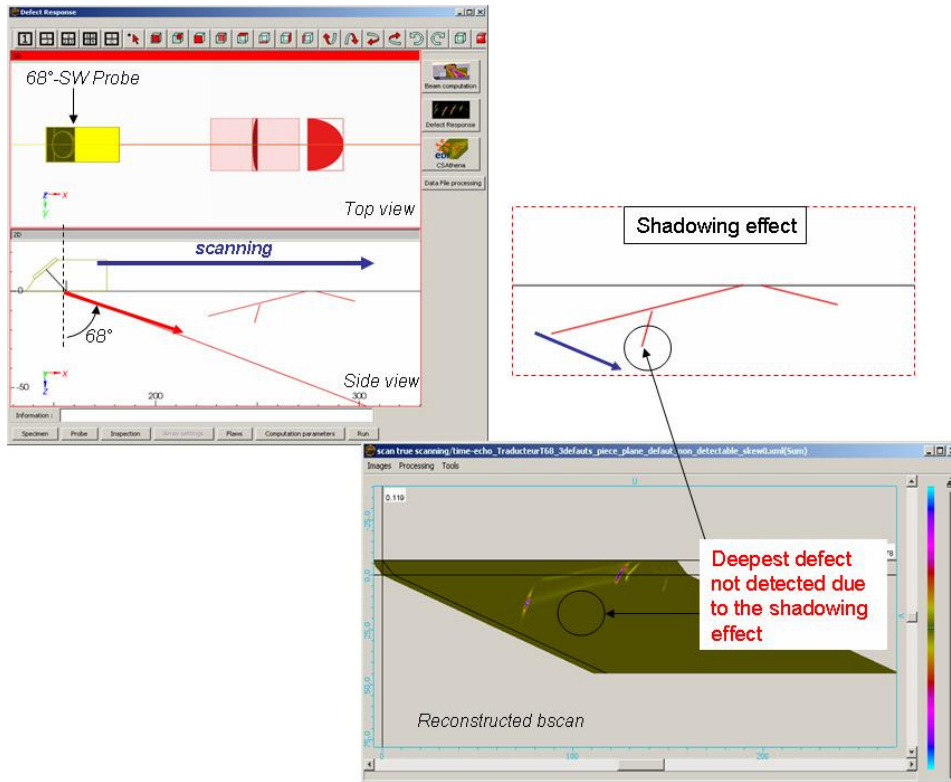


Figure 12 - Simulation of the shadowing effect

Skewed defect

Another limitation comes from the possible disorientation of the defect in the transverse plane (skewed defect). The sketch in Figure 13 and the simulation in Figure 14 illustrate such a limitation. We note that the existing method is not sensitive to skewed defects.

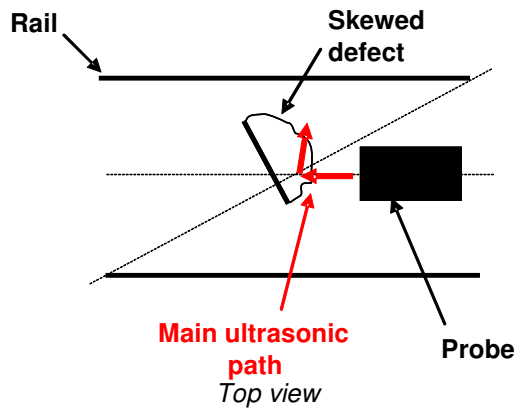


Figure 13 - Illustration of the skewed effect

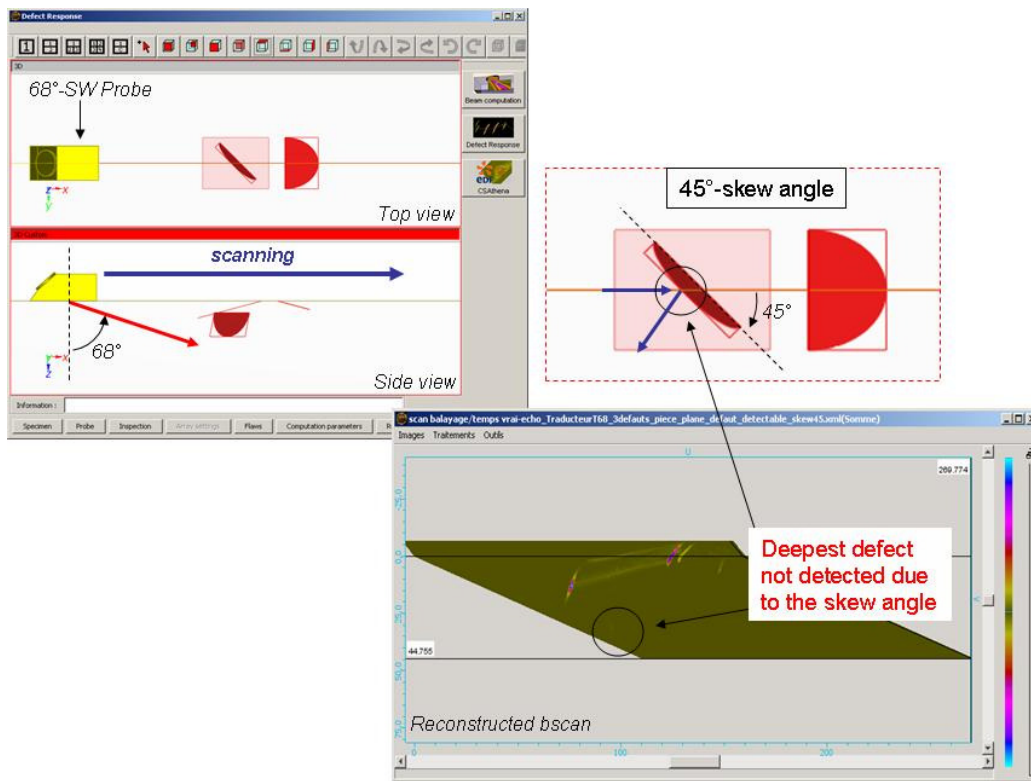


Figure 14 - Simulation on a skewed defect.

Evaluation of innovative methods

3D-electronic scanning

Description of the method

The method carried out in this work is based on a matrix phased array transducer. This probe makes it possible to generate various inspection angles. The active surface is made up of several elements which can be individually excited. By applying appropriate delays in transmission and in reception to each element, it is possible to modify the refracted angle and the depth focusing.

In this application, the matrix generates 45°-shear waves in the rail axis, while angular scanning is done from +45° to -45° in the transverse plane (cf. Figure 15).

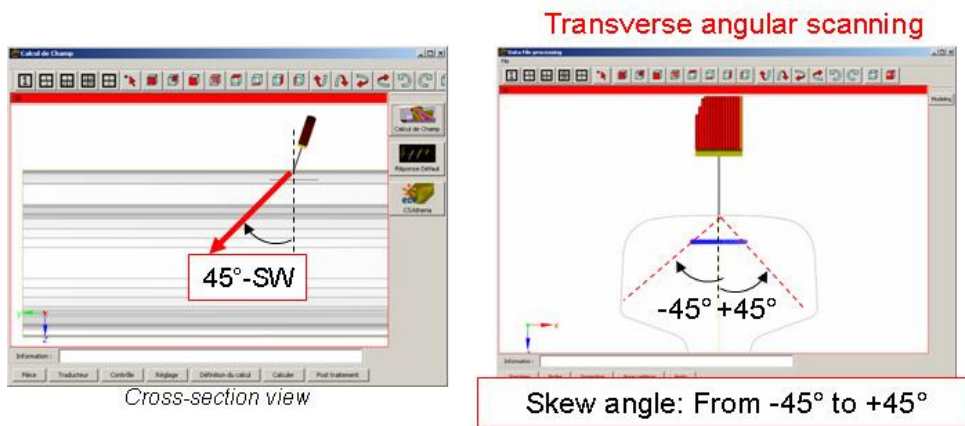
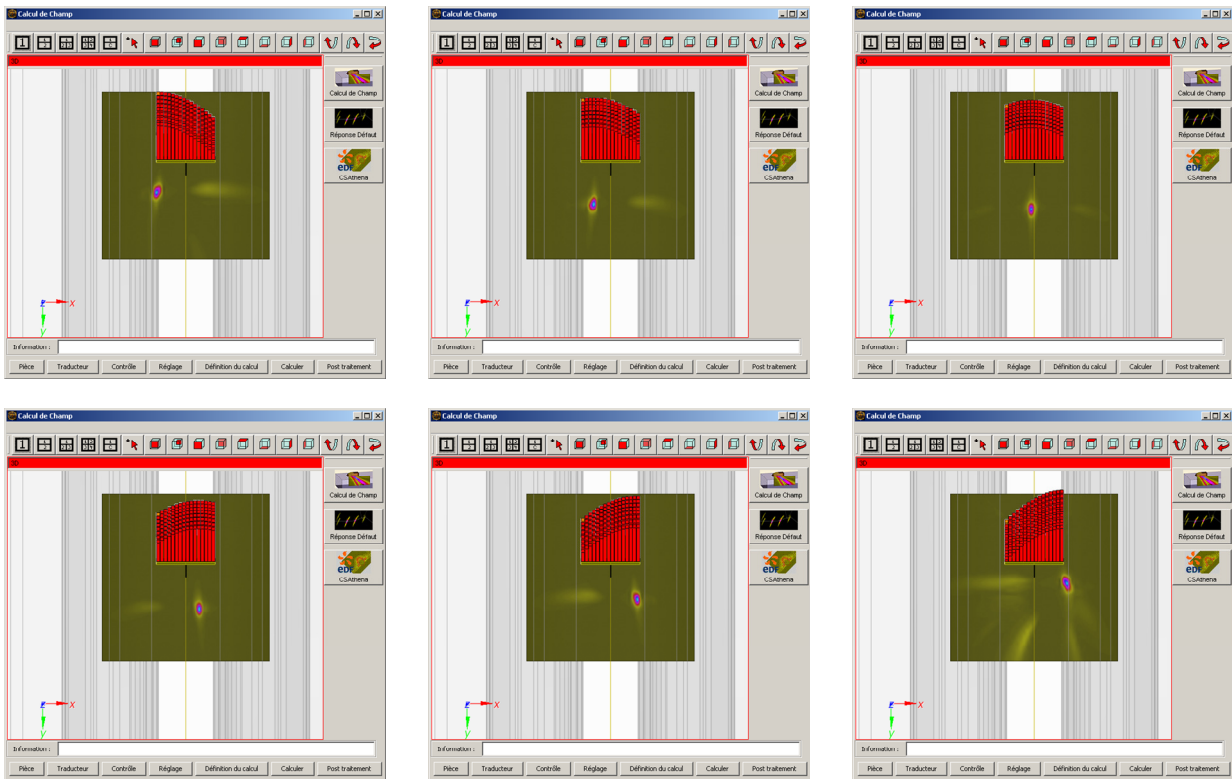


Figure 15 - Description of the angular scanning.

Figure 16 shows examples of ultrasonic fields radiated in the rail for several inspection angles in the transverse plane. We note that in all cases, the focal spot diameter is about 3 mm.



Top views

Figure 16 - Simulation of ultrasonic fields radiated by the matrix phased array probe

Evaluation of the method by simulation

The method previously described was evaluated using simulation. Two defects among those included in rails from the University of Birmingham were defined in the simulation. As shown in Figure 17, defects have a 25°-tilt angle, the first one has no skew angle, the second has a 35°-skew angle.

Rails from University of Birmingham

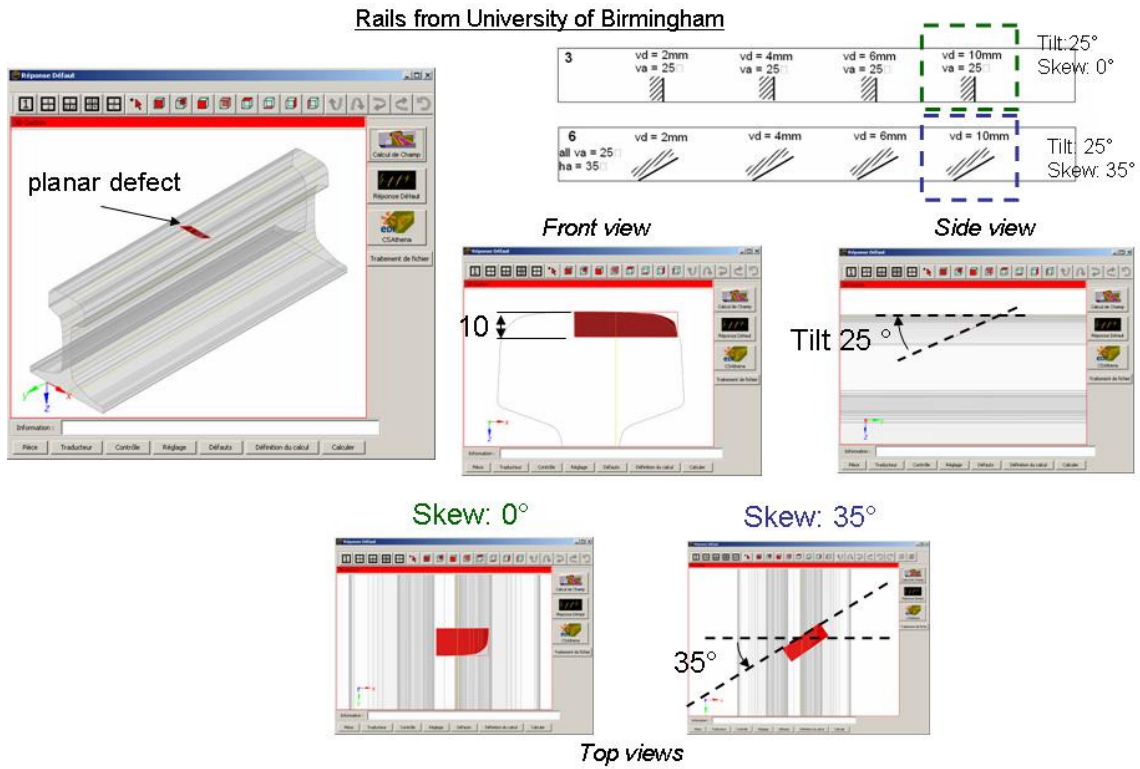


Figure 17 - Description of defects defined in CIVA.

Figure 18 and **Erreur ! Source du renvoi introuvable.** show simulation results of defect responses obtained on both defects. These images show angular scanning extracted at the positions where tip diffraction echoes were detected. In the first case, we observe that the maximum amplitude is obtained for the 0°-shot, while in the second case, the maximum is obtained for the 35°-shot.

These results show that the method is able to correctly detect skewed defects.

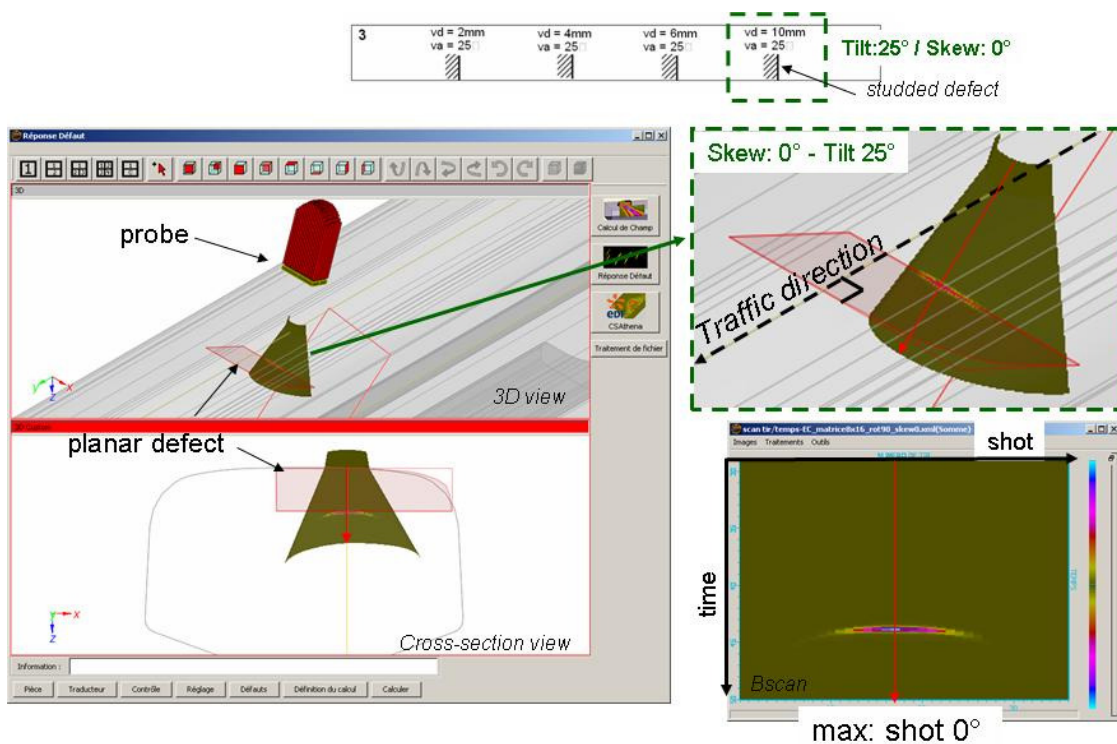


Figure 18 - Simulation of defect response– Result on the no skewed defect

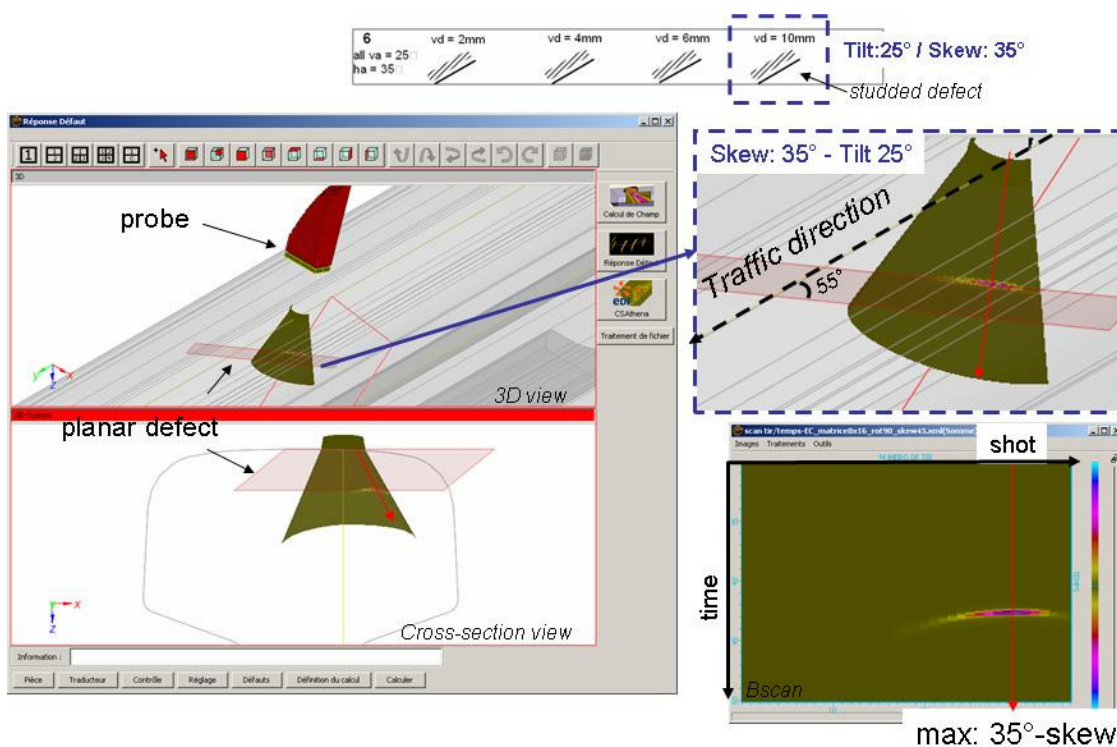


Figure 19 - Simulation of defect response– Result on the 35°-skewed defect

Experimental evaluation of the method on artificial defects

Acquisitions were carried out with a 128 elements phased array matrix (cf. Table 2, driven by a M2M acquisition system from GERIM platform. For this first feasibility study, inspections were made in an immersion tank and a XY mechanical scan was done above the running band, while an angular scanning was done at each position.

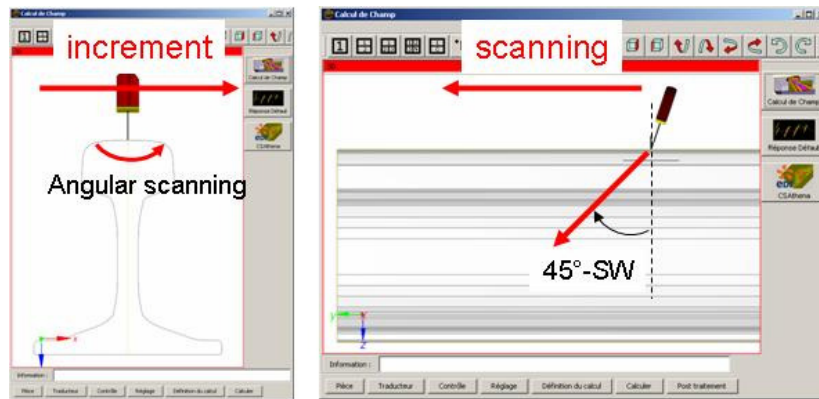
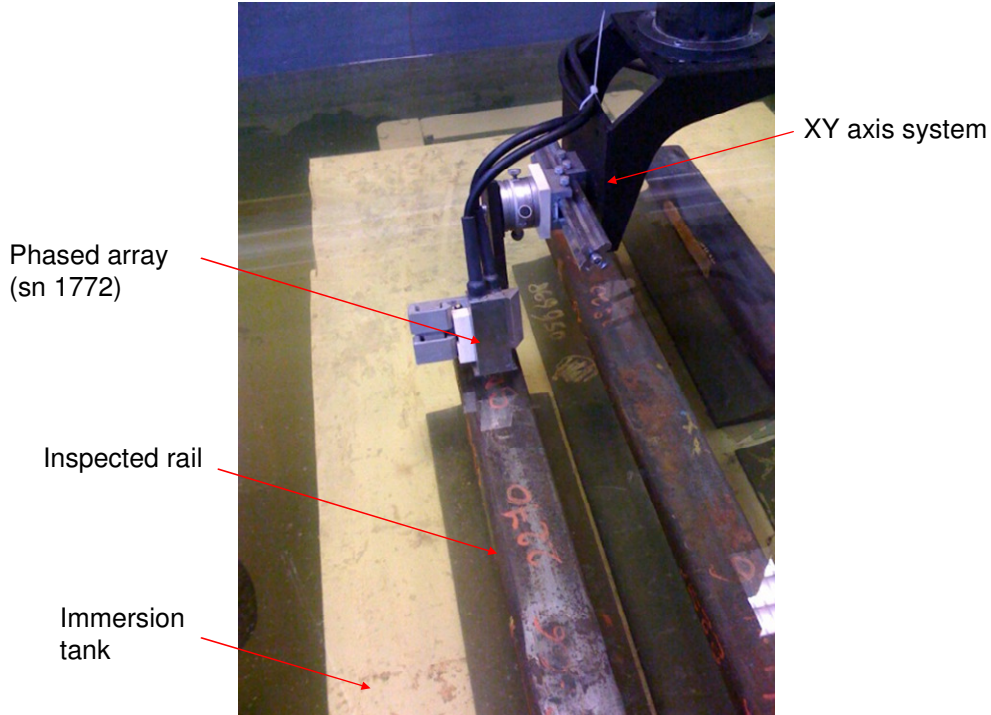


Figure 20 - Description of the acquisition.

Type	Frequency (MHz)	Nbr of elements	Element size (mm ²)	Active surface (mm ²)	SN
Matrix	5	128 (8x16)	1x1	8.7x17.5	1772

Table 2 - Main probe parameters.

Acquisition on the 0°-skewed defect

Figure 21 shows a B-scan shot/time extracted from acquisition made on the 0°-skewed defect. We observe that the maximum amplitude is obtained for the shot at 0° in the transversal plane. This experimental result is in accordance with simulation.

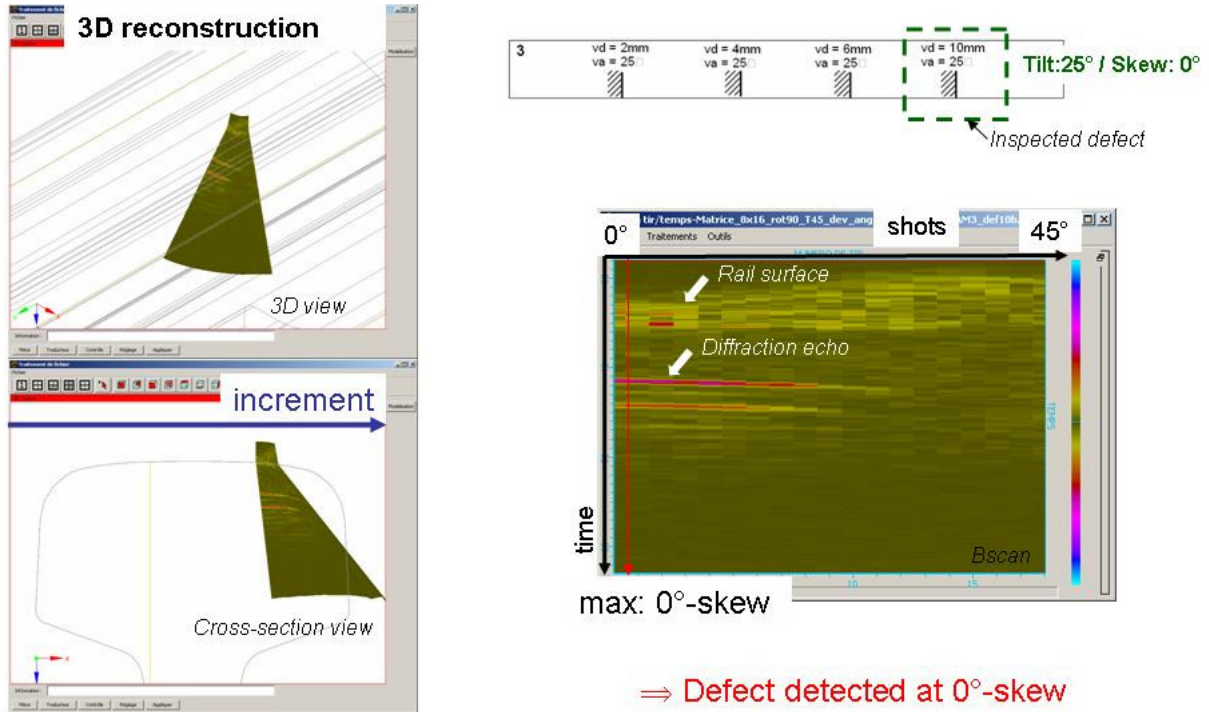


Figure 21 - Acquisition on the 0°-skewed defect – Bscan angular scan/time.

From this acquisition, it is possible to extract data from only one shot. Thus, when we extract acquisition from the 0° shot, we observe the C-scan and B-scans shown on Figure 22. Extraction of B-scans at several positions of increment allows the depth of the crack to be evaluated. In that case, the crack is between 7 and 11 mm-depth.

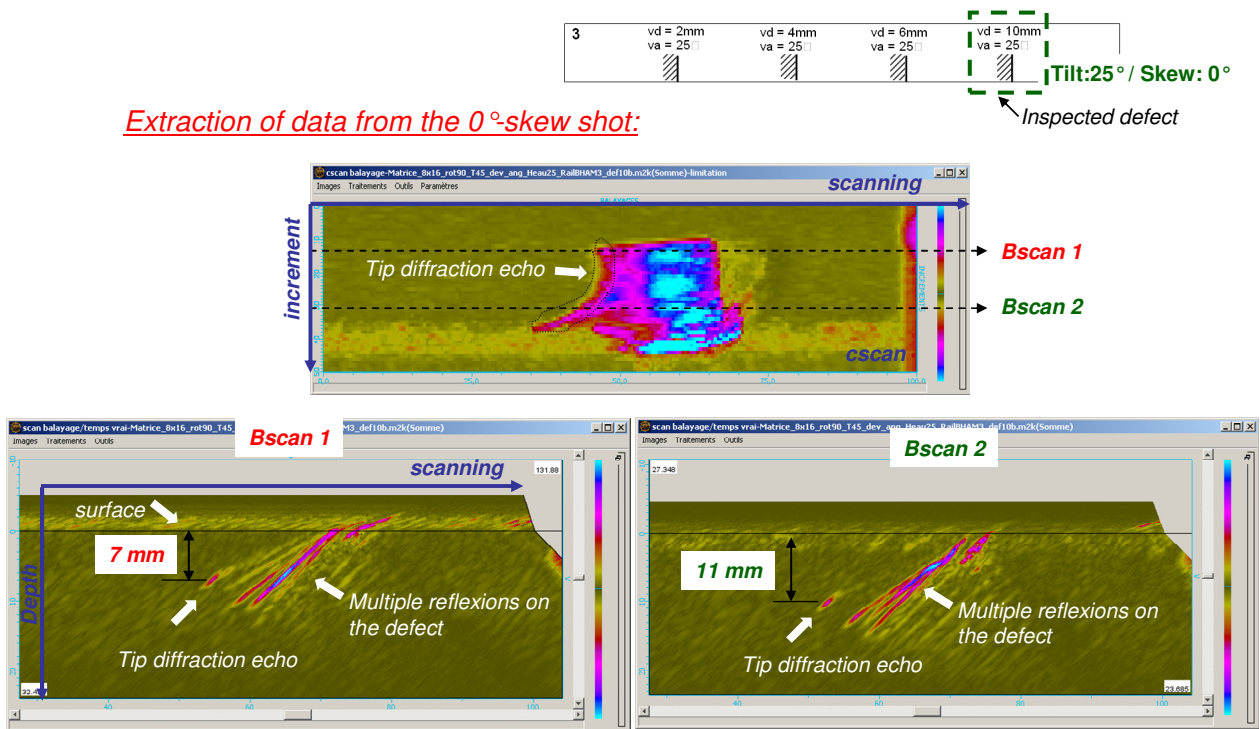


Figure 22 - Acquisition on the 0°-skewed defect – Cscan extracted from the 0°-skewed shot

Acquisition on the 35°-skewed defect

Acquisitions were made on the second defect as previously. Figure 23 shows that the maximum amplitude of the tip diffraction echo is obtained for the 45°-shot in the transverse plane.

Experimental results

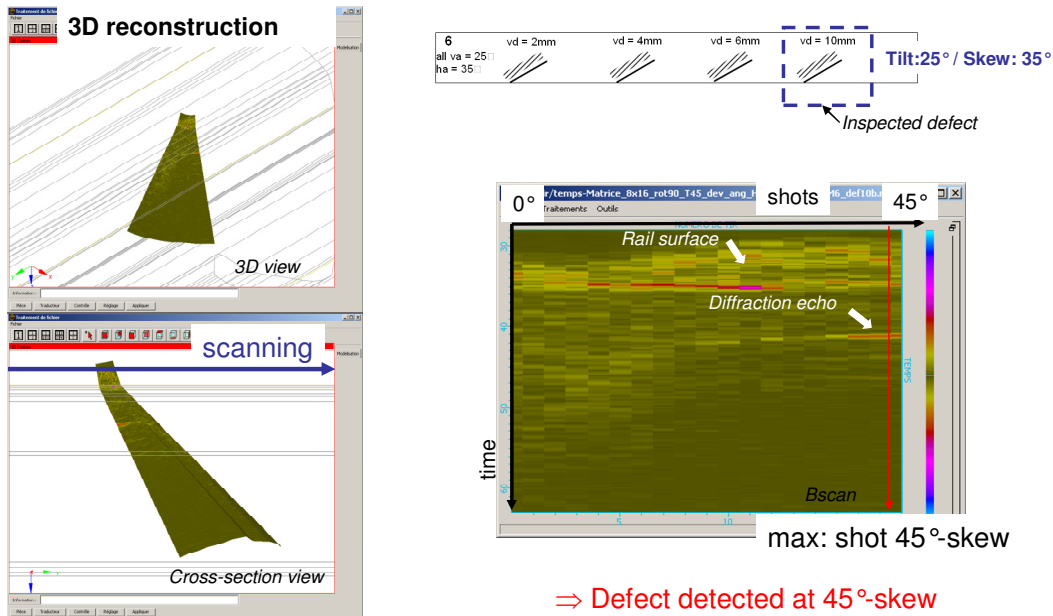


Figure 23 - Acquisition on the 35°-skewed defect – Bscan angular scan/time.

From observations made on the angular scanning, data were extracted for the 45°-shot. We observe that this skewed defect can correctly be detected and characterised, from 7 to 9 mm-depth.

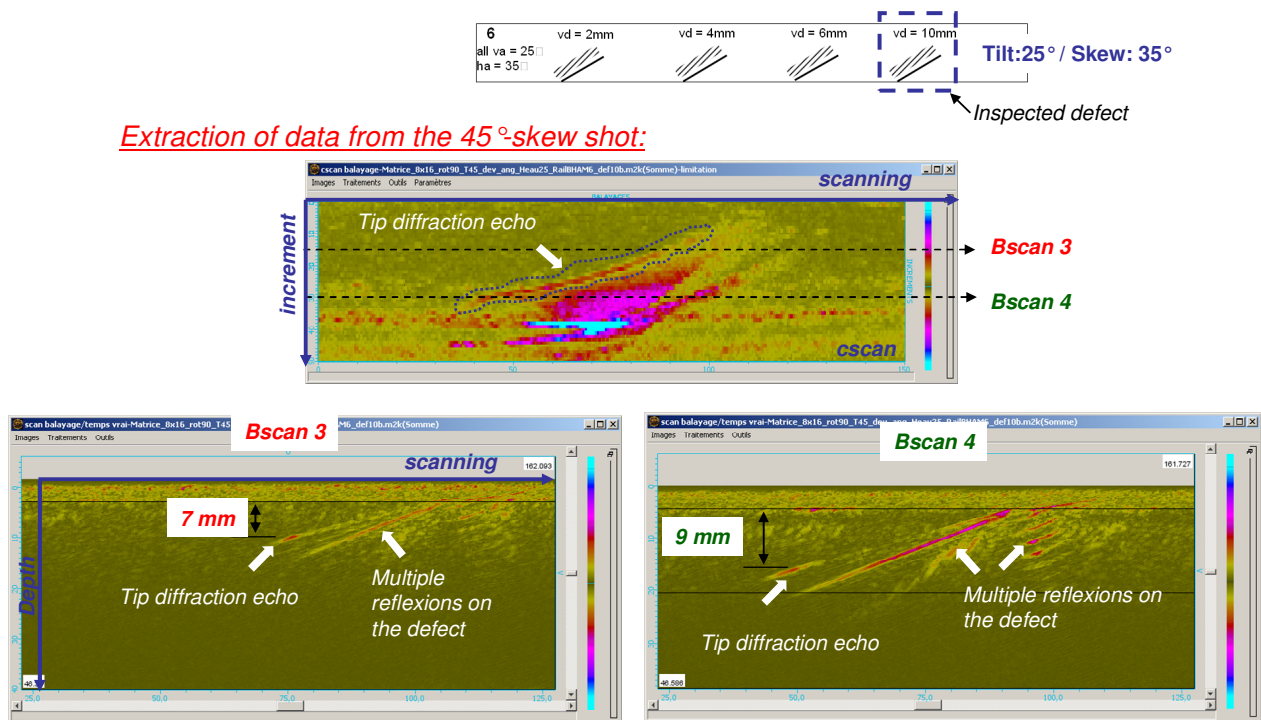


Figure 24 - Acquisition on the 35°-skewed defect – Cscan extracted from the 45°-skew shot.

Experimental evaluation of the method on real defects

Rail CER310-07

Acquisitions were carried out on a real squat defect contained in the sample CER310-07. The photo in Figure 25 shows a dark spot and surface breaking cracks.

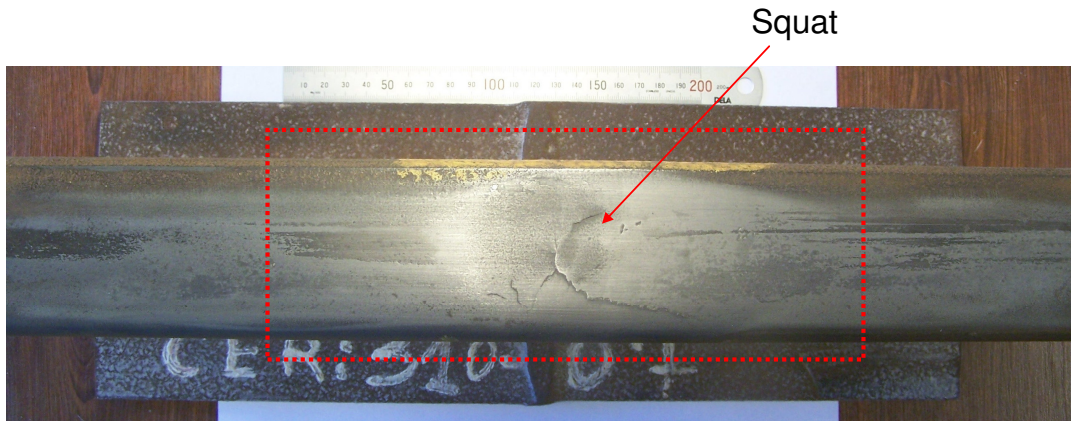


Figure 25 - Photo of the rail CER310-07

Images presented in Figure 26 were extracted from the 0°-shot. We observe that for the position of increment of B-scan 5, a tip diffraction echo detected a 6 mm depth. At the increment position of the B-scan 6, no tip diffraction echo is detected. This last image illustrates, once again, the limitation of an inspection method with only one angle of inspection in the transversal plane.

Extraction of data from the 0°-shot:

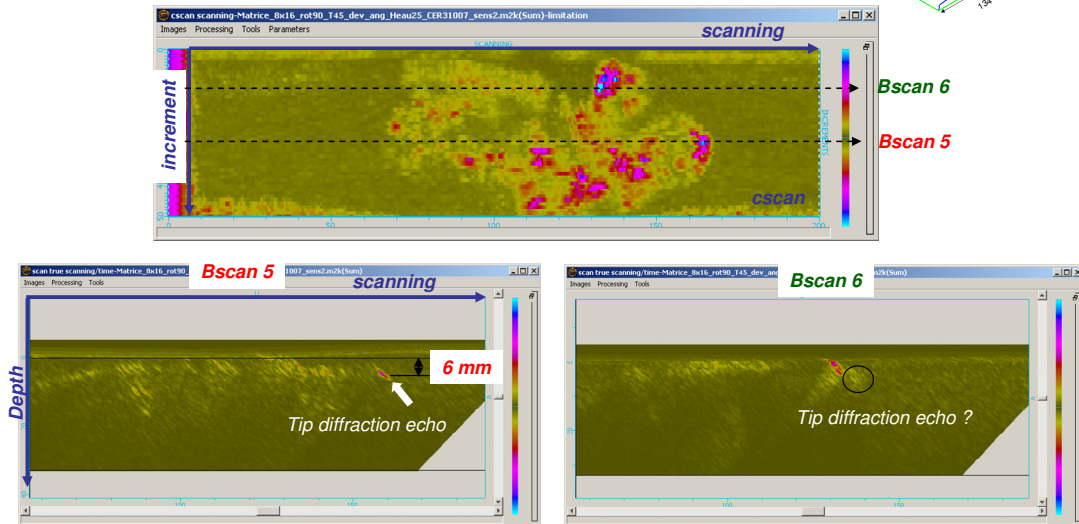
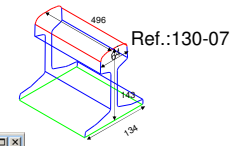


Figure 26 - Acquisition on sample 310-07 – C-scan and B-scans extracted from the 0°-skew shot.

Figure 27 shows a comparison of the c-scan of the 0°-shot and a c-scan composed by the superimposition of all shots. We observe that for the same position of increment, the tip diffraction echo is not detected with the 0°-shot, but with the 15°-shot. A similar observation can be made in Figure 28.

These results show that angular scanning significantly increases the possibility of detecting tip diffraction echoes of skewed defects.

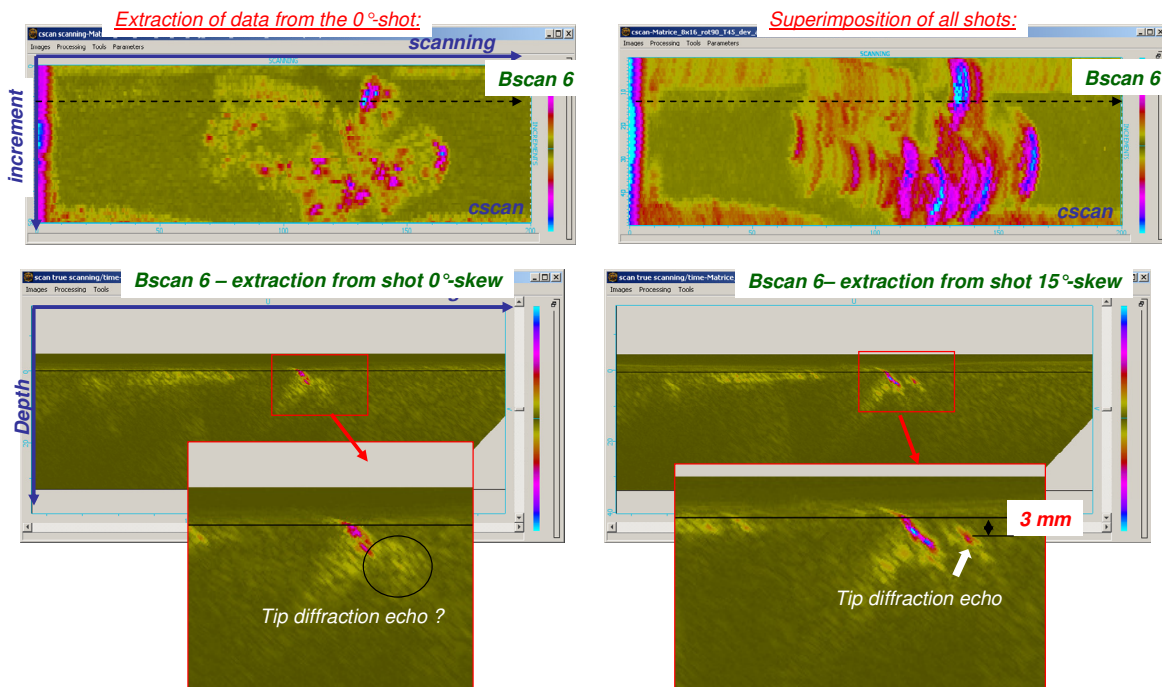


Figure 27 - Acquisition on sample 310-07 –Comparison between the 0°-skew shot and the cumulated Cscan of all shots.

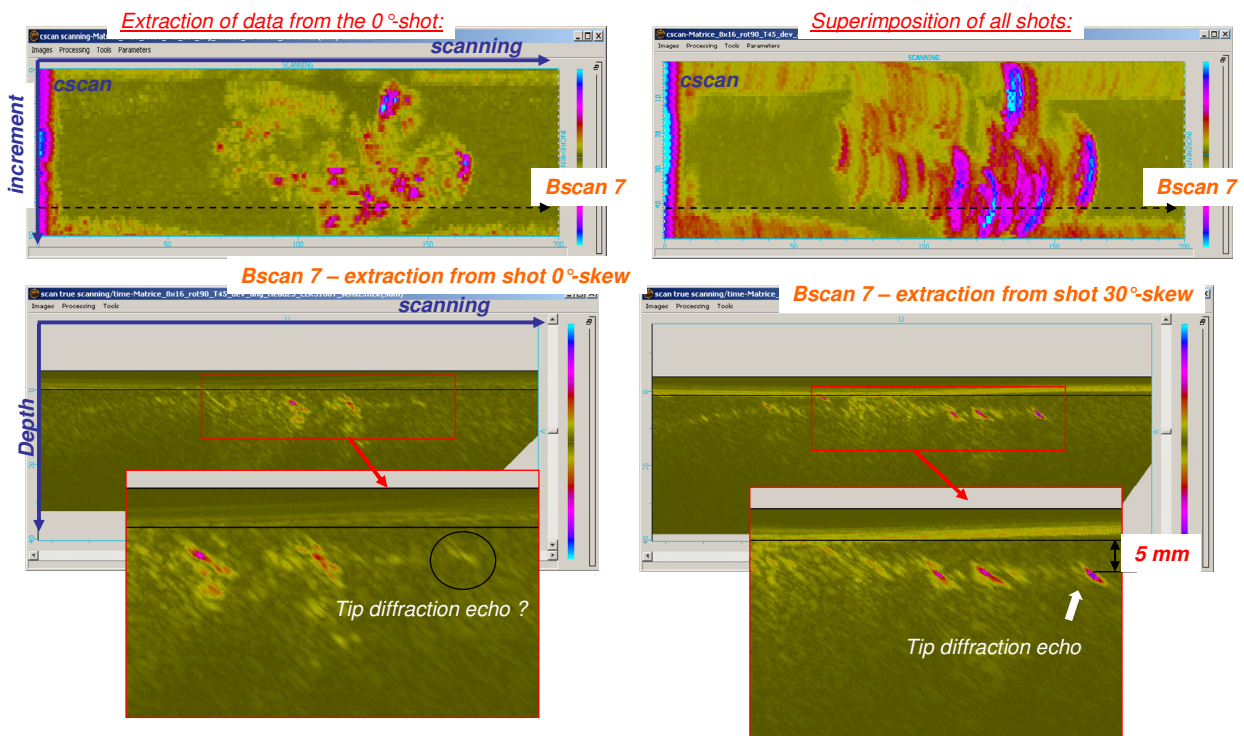


Figure 28 - Acquisition on sample 310-07 –Comparison between the 0°-skew shot and the cumulated Cscan of all shots.

Rail CER295-07

Acquisitions were carried out on another real defect contained in the sample CER295-07. In Figure 25 we can also observe the dark spot and surface breaking cracks.



Figure 29 - Photo of the rail CER295-07

Figure 30 shows the results of acquisition performed on sample CER295-07. We can see on B-scan 8 that for the 0°-shot, the tip diffraction echo is not detected. On the other hand, the 14°-shot shows that at the same probe position, a tip diffraction echo is detected.

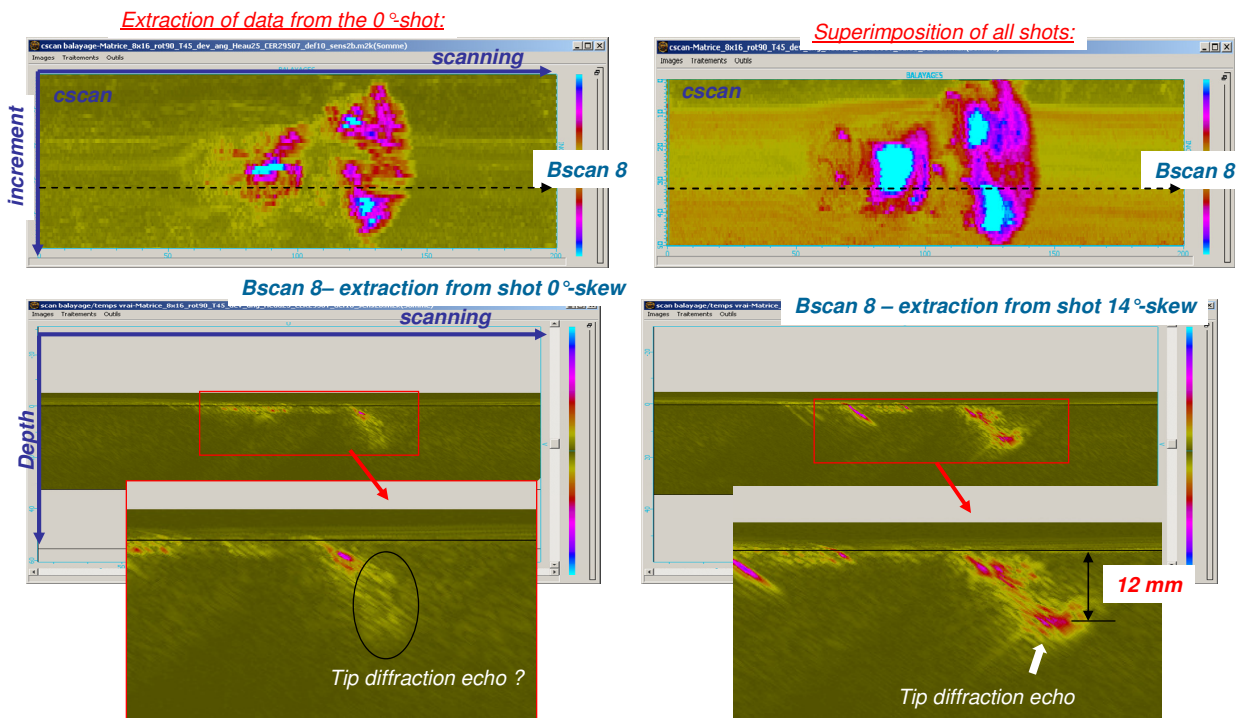


Figure 30 - Acquisition on sample CER295-07 –Comparison between the 0°-skew shot and the cumulated C-scan of all shots.

All of these results show the advantage of generating angular scanning in the transversal plane. This method allows skewed defects to be detected. Nevertheless shadowing effects can be compensated in some, but not all cases.

Through transmission method

Description of the method

Aim: to compensate for both shadowing and skewed orientation.

Principle: one phased-array probe as transmitter and one phased-array probe as receiver. Obscuration of the signal by the defect between the transmitter and the receiver

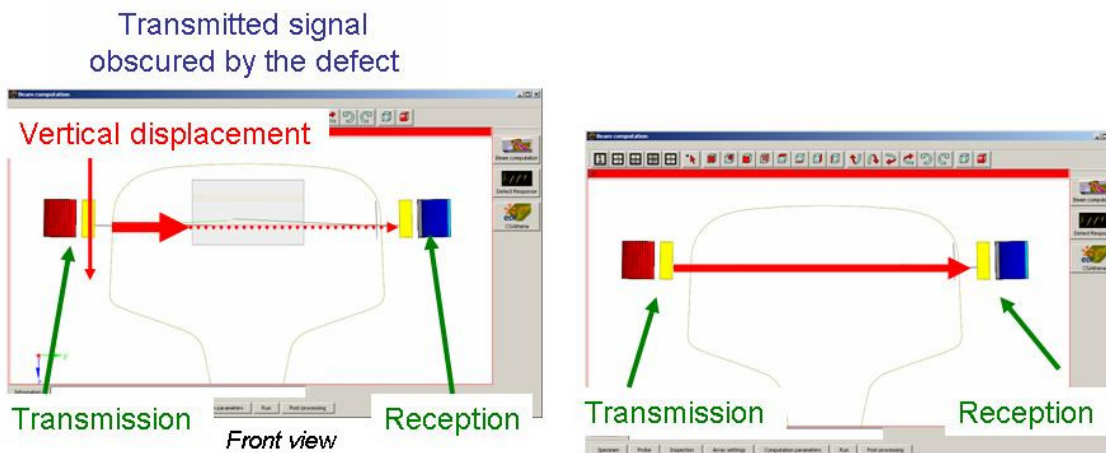


Figure 31 - Principle of the transmission method

To detect skewed defects, an electronic commutation is simultaneously applied on both transducers. (Figure 32)

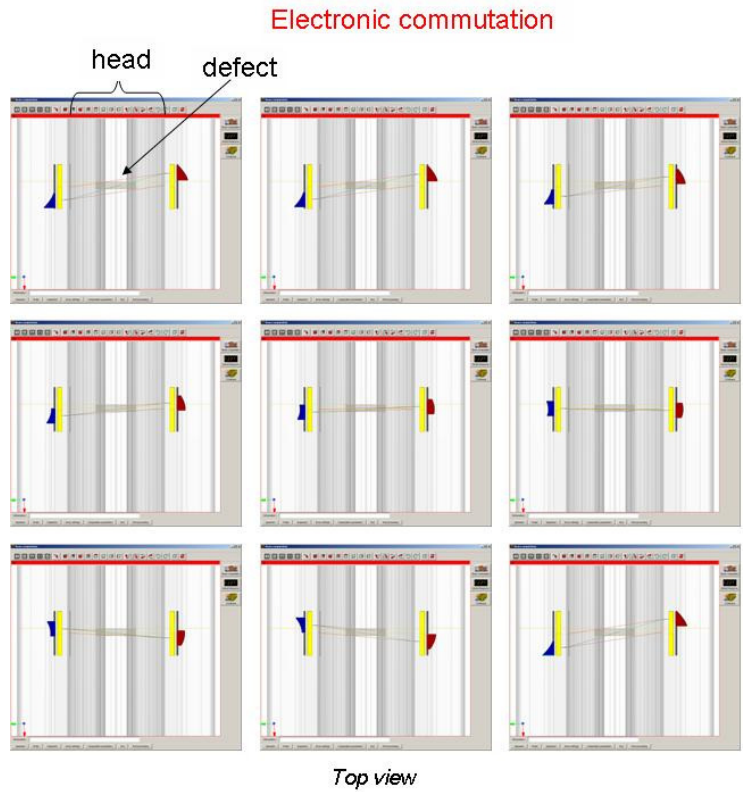
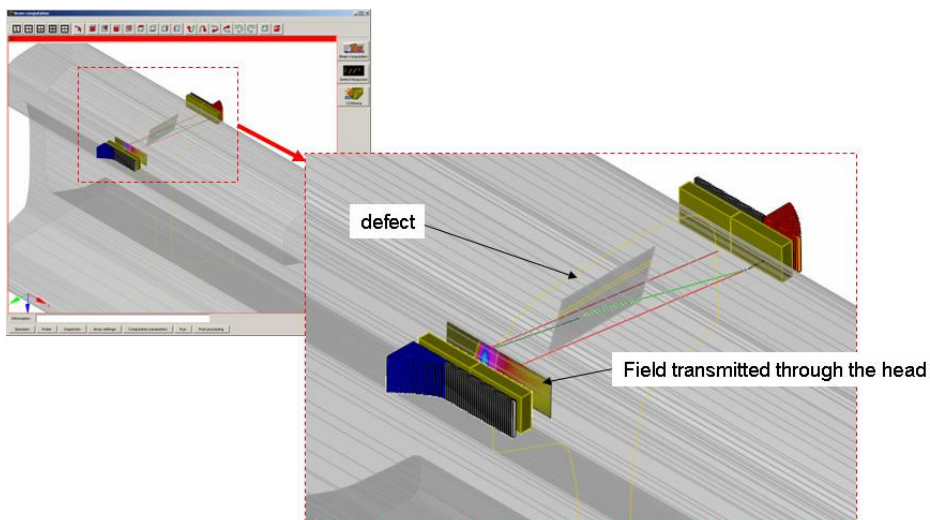


Figure 32 - Electronic commutation – Examples of sequences

Type	Frequency (MHz)	Nbre of elements	Element size (mm ²)	Active surface (mm ²)
Linear	5	48	0.6x10	33.5x10

Table 3 - Main probe parameters.



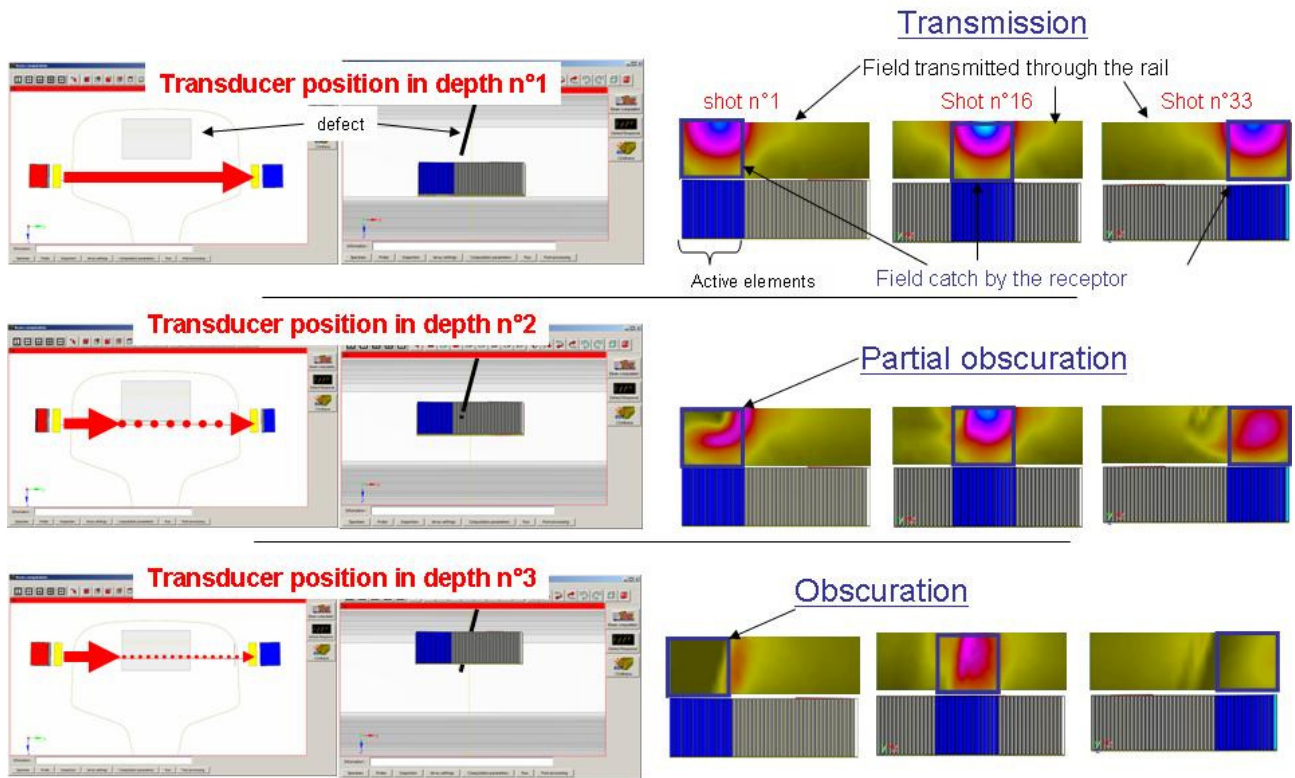


Figure 33 - Simulation of fields received by the receptor.

Experimental evaluation of the through transmission method

1. Calibration

Description: acquisition on a parallelepiped sample with regular surfaces.

Results:

- variation lower than 1dB for one sequence during the displacement
- variation lower than 3 dB between all sequences

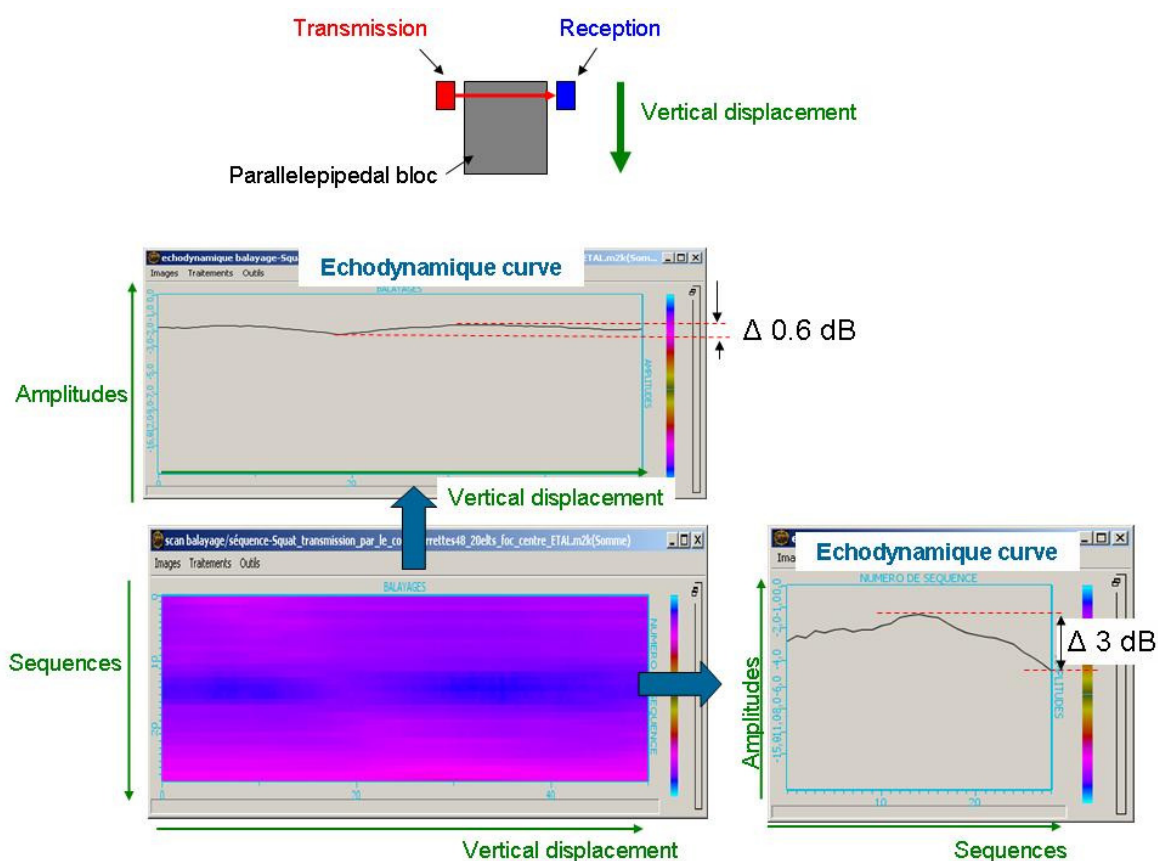


Figure 34 - Calibration of the through transmission method

2. Evaluation of the method on a real defect (CER310-07)

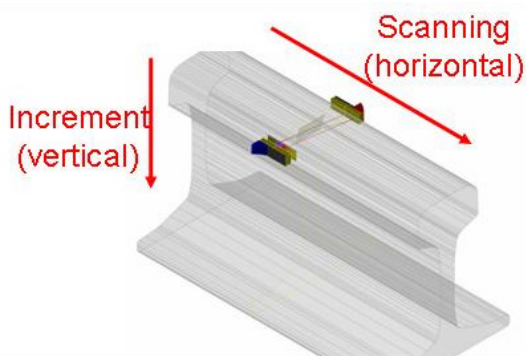


Figure 35 - Description of the mechanical displacements of the probes

In this method, a defect is detected due to the loss of the signal from the transmitter. It is then necessary to ensure that the loss of signal is due to the presence of a defect and it has not been caused by another source.

The aim of these tests is to evaluate this method in realistic conditions.

Tests:

- Acquisition 1: test without surface preparation
- Acquisition 2: test with surface preparation (paint removed from the side of the head).

Results:

- Figure 36: acquisition 1 – example of b-scan scanning/sequences where two main areas have a loss of 5 to 6 dB which may indicate one or several defects in the rail.
- Figure 37: acquisition 2 – b-scan scanning/sequences at the same position as in Figure 36. By comparison with acquisition 1, we observe that one area where the amplitude decreased has disappeared.

Conclusion: the method is sensitive to the state of surface. It is necessary to have surface preparation of the head sides.

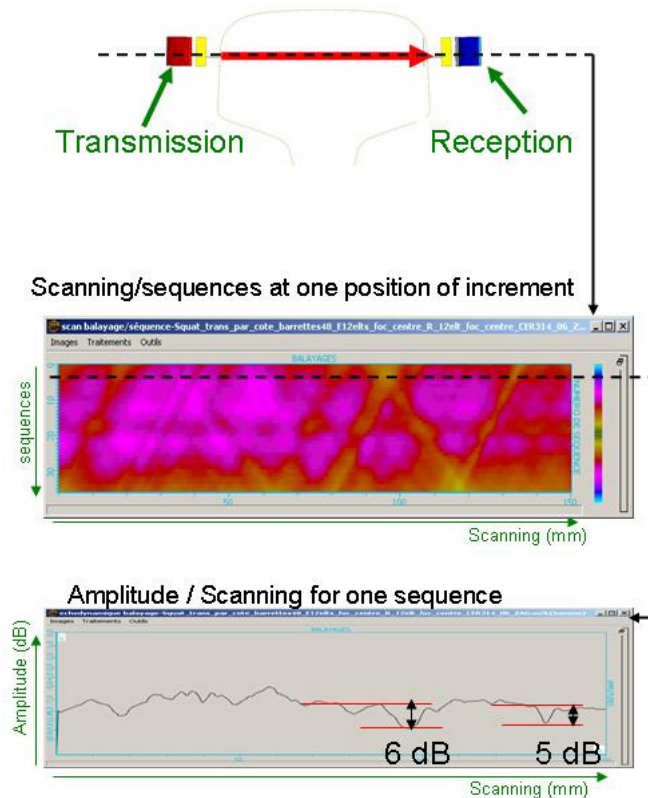


Figure 36 - Acquisition in through transmission technique before surface preparation.

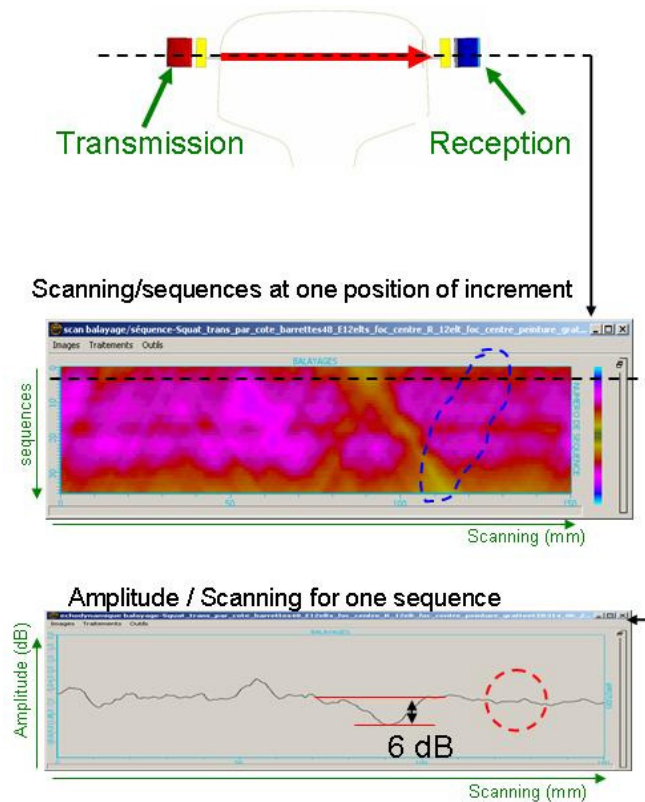


Figure 37 - Acquisition in through transmission technique before after surface preparation (paint removed)

Conclusion on innovative UT-method for squat characterisation

3D-electronic scanning:

Acquisitions have shown that this method allows detection of the skewed defect. Tip cracks are detected in depth. Unfortunately, the shadowing effect can still exist with this method.

Through transmission method:

This method appears to be free from the shadowing effect and would be able to detect skewed defects thanks to the electronic commutation.

The first tests have shown that this method is sensitive to the state of surface of the head. This is disagreed with requirements described in part 3.1.1. This method appears to be difficultly used in the track for continuous measurement.

Head Checking Characterisation by UT-Inspection

Description of the defect

Head checking defects are generally positioned in the gauge corner and appear as cracks either regularly or irregularly spaced, from 1 mm to several cm.

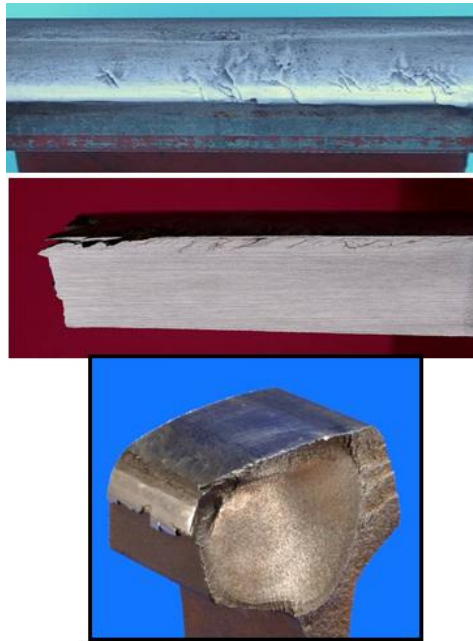


Figure 38 - Photos of head checking. Examples of surface appearance and transverse crack development

Head checks are very difficult to detect at the earliest stage of development because the cracks are small and fine. Head checks come in a variety of shapes on the surface of the rail, so they develop in a variety of patterns sub-surface. Sketches in Figure 39 show the development of head checking into the head [1].

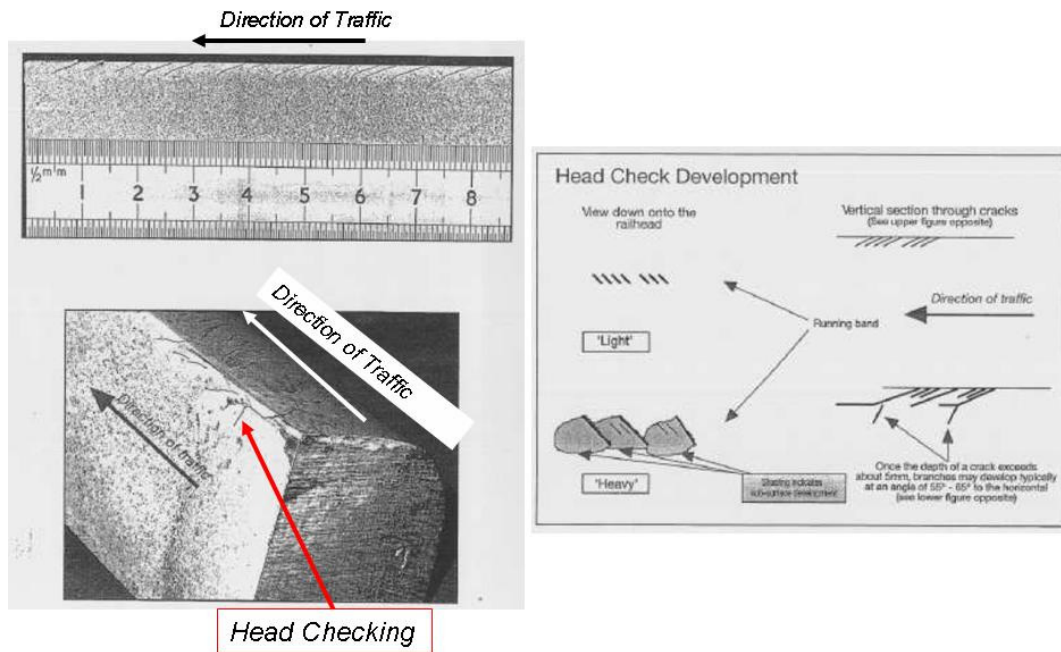


Figure 39 - Illustration of the development of Head checking

Current method of characterisation

Depth measurement

Inspection involves both the visual classification of the head checking and ultrasonic examination. The significant visible crack length is 20 mm. If the surface length is 20 mm or greater it is possible that a downward branch has developed with a significant breakage risk. A visible crack length of less than 20 mm is considered to be a low risk situation.

Depth measurement of head checking requires the use of a 68°-shear wave probe. The probe is positioned as far as possible from the centre line (~20 mm) towards the gauge corner to detect branches of the cracks at longer range.

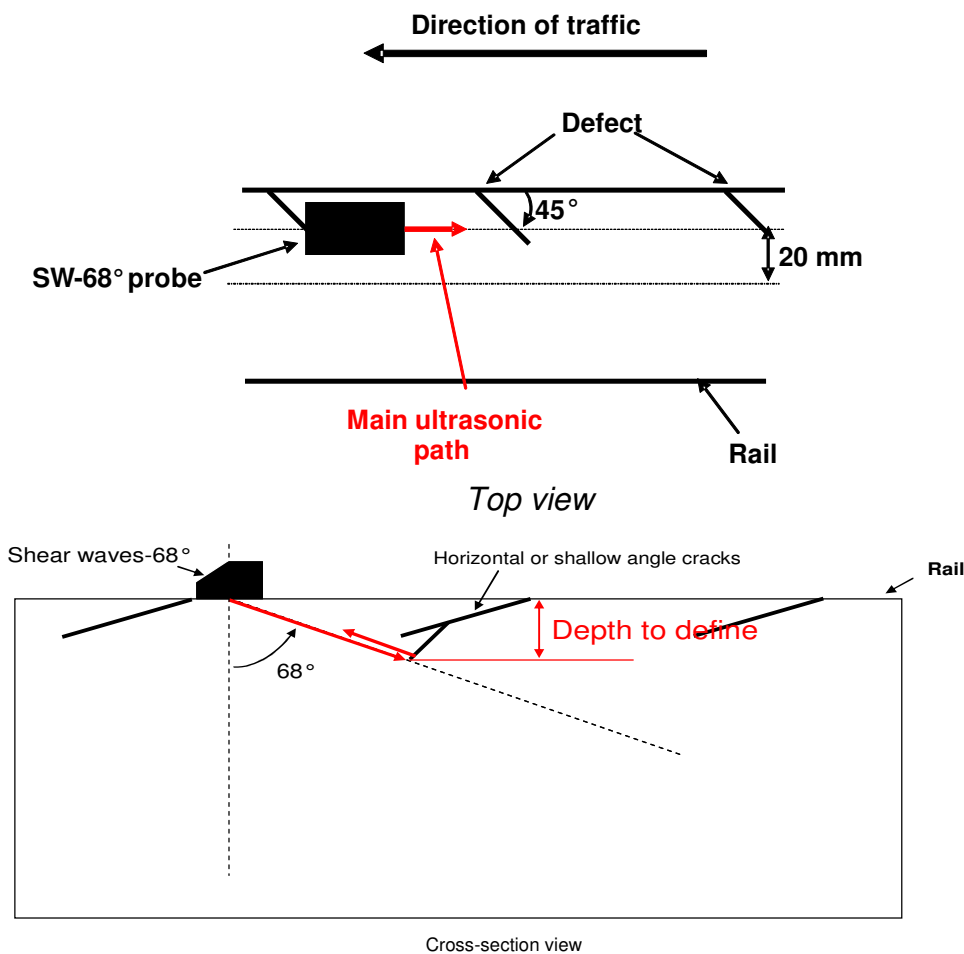


Figure 40 - Illustration of the measurement of the depth

Limitations of the actual methods of measurement

The method of depth measurement presents two main limitations according to the characteristics of the cracks: shadowing and skew effects.

Shadowing effect

A particular risk is the fact that one crack could hide deeper one, which means that the shadowing effect can exist, which prevents the characterisation of cracks in depth.

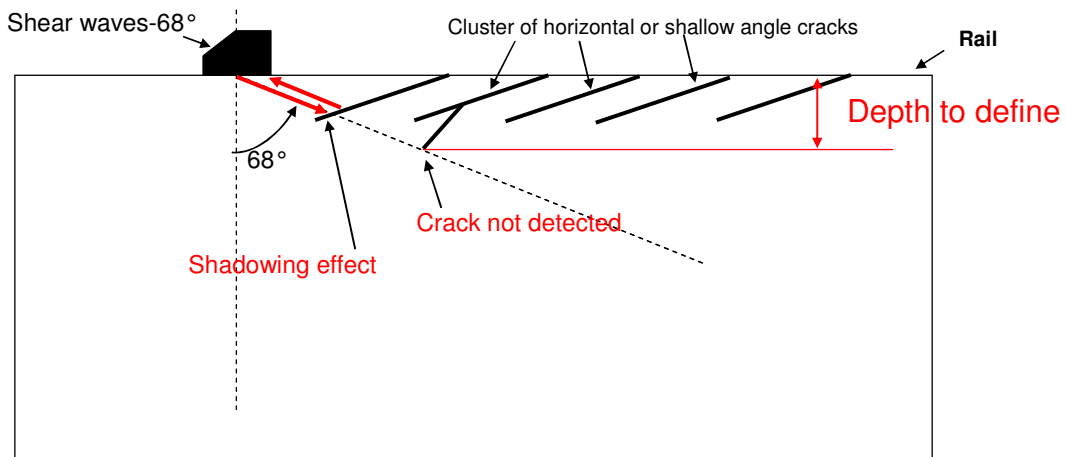


Figure 41 - Illustration of the shadowing effect

Skewed defect

Head checking cracks are generally skewed as illustrated in Figure 42. For this reason, a pulse-echo method with a plane of incidence parallel to the longitudinal axis of the rail cannot detect the deepest tip of the crack in that case.

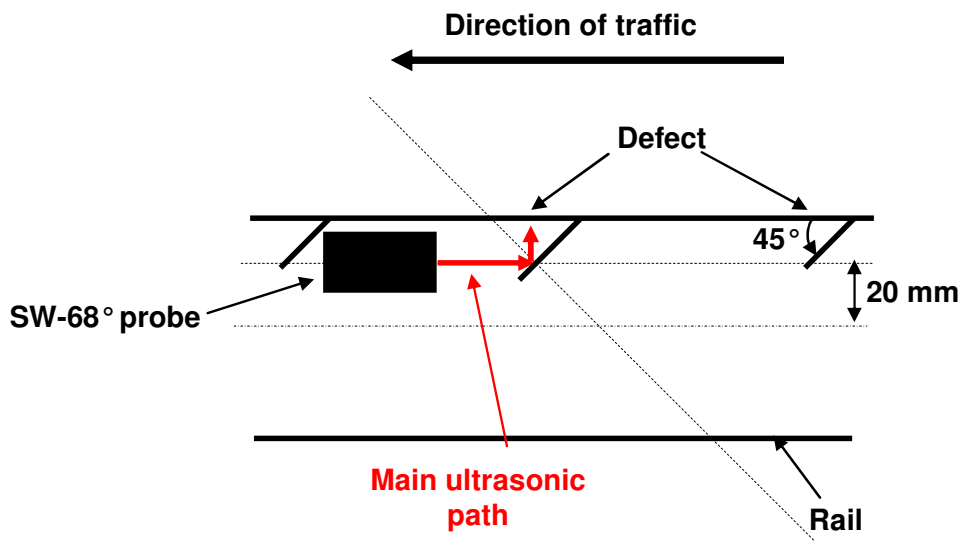


Figure 42 - Illustration of the skew effect.

Evaluation of innovative methods

3D-electronic scanning :

A 3D-electronic scanning technique was evaluated to characterise head checking defects. This method is similar to the one evaluated on the squat defect which means that the matrix generates 45°-shear waves in the vertical plane of the rail, while electronic angular scanning is done horizontally from +45° to -45° in the transverse plane. In the specific case of head checking inspection, the plane of incidence of the probe is oriented at 45° from the longitudinal axis of the rail in the horizontal plane to take into account the skew angle of the defects.

Acquisitions were made with a 128 elements phased array matrix (cf. Figure 43 and Figure 44), driven by a M2M acquisition system from GERIM platform. A XY mechanical scan was done above the running band while an angular scan was performed at each position.

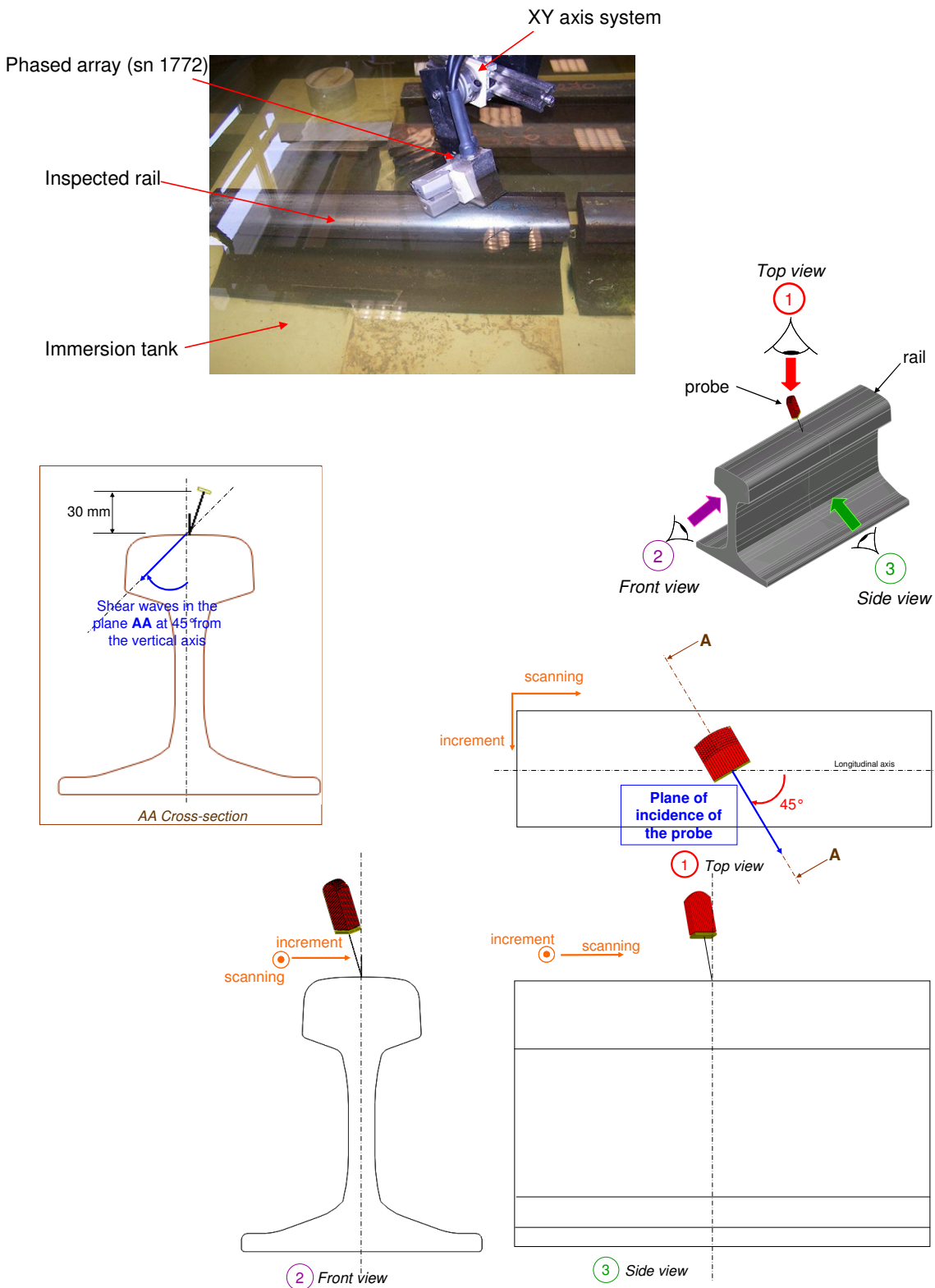


Figure 43 - Description of the position of the probe

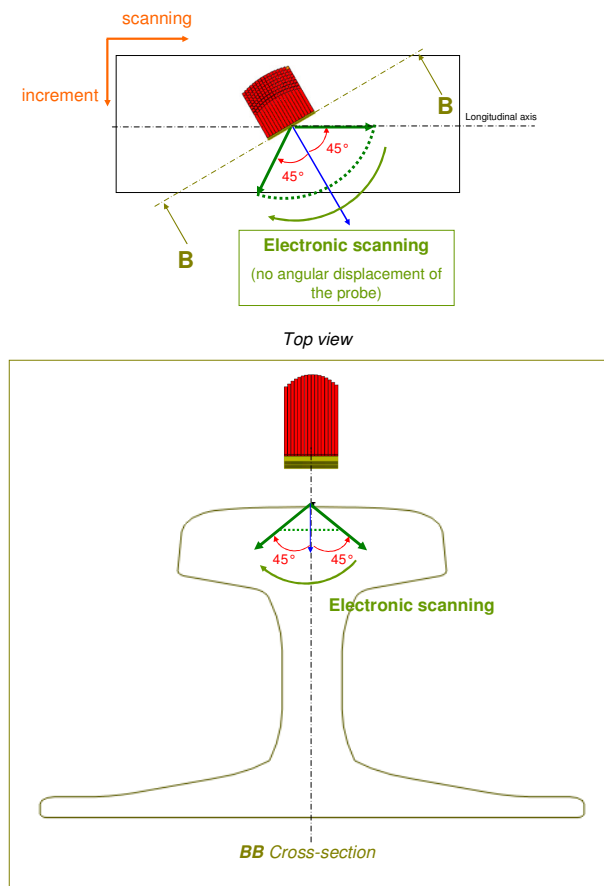


Figure 44 - Description of the electronic scanning

Sample CER212-04

A visual observation shows that cracks are spaced from 3 to 8 mm. Acquisition was made above the damaged gauge corner on all the length of this sample i.e. 500 mm.

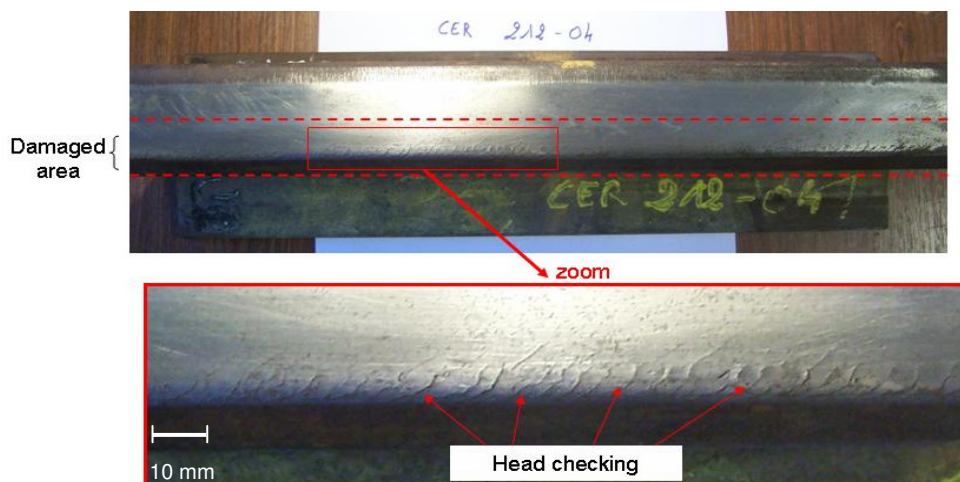


Figure 45 - Photo of the rail CER212-04

Some results are shown in Figure 46. The image at the top corresponds to a C-scan where data are extracted at 45° towards the longitudinal axis of the rail. All indications come from surface breaking cracks in

the damaged area. The image at the bottom corresponds to a B-scan extracted from the above C-scan at the dotted line. We note that almost all cracks have the same size with a maximum depth of 9 mm in depth and one crack is detected at a deeper depth.

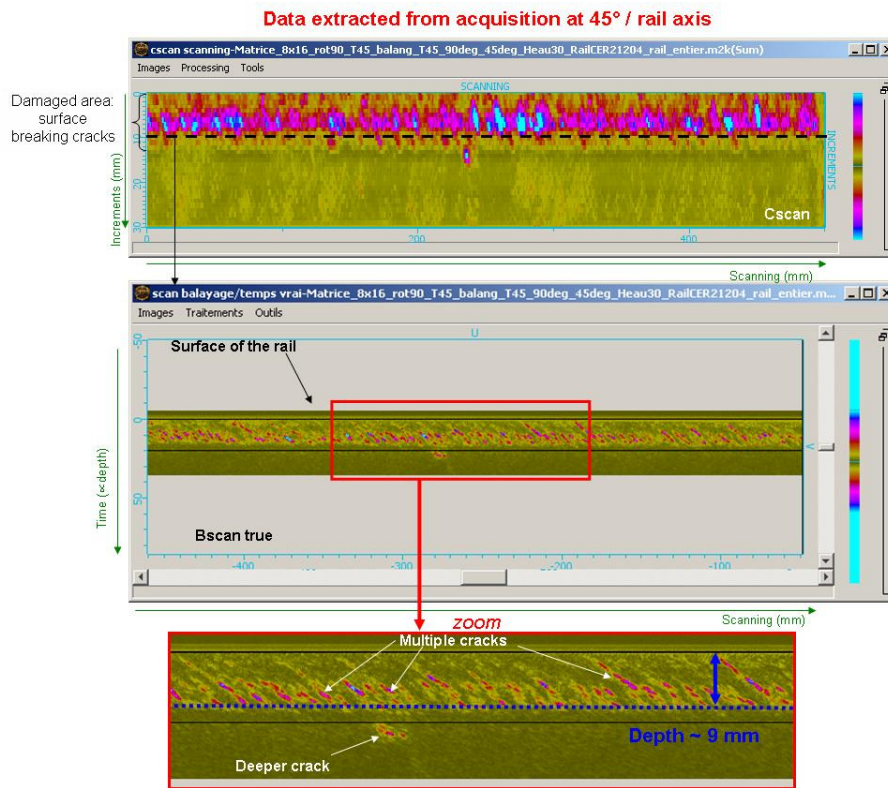
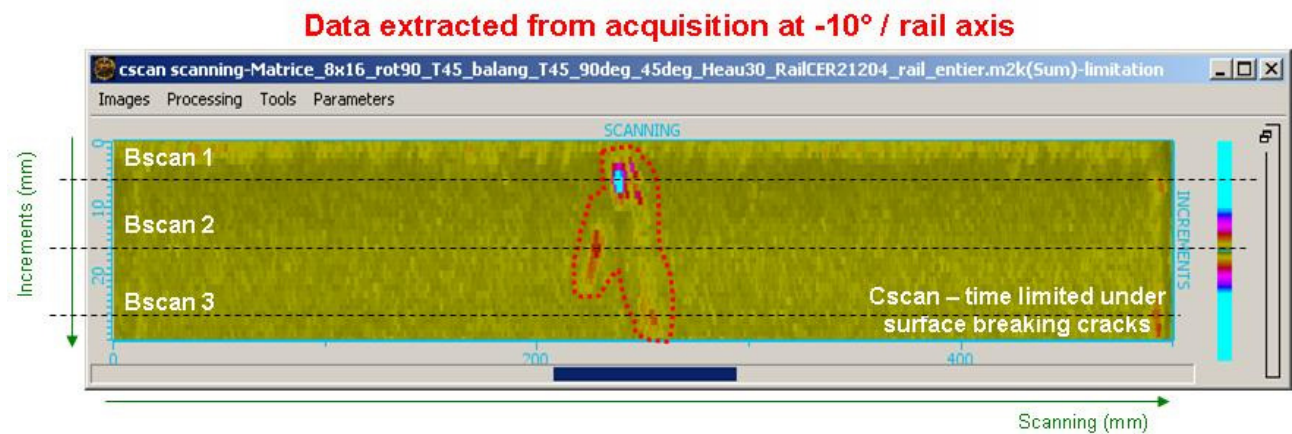
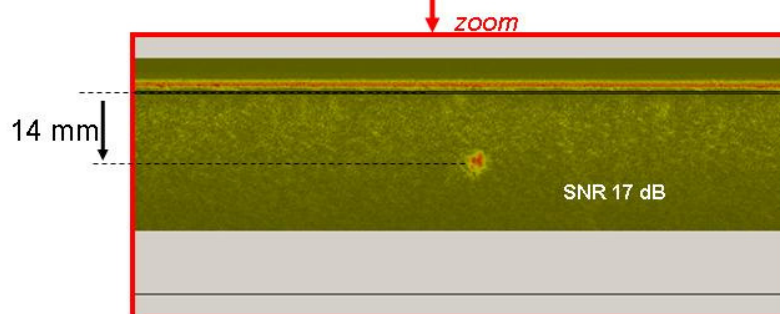
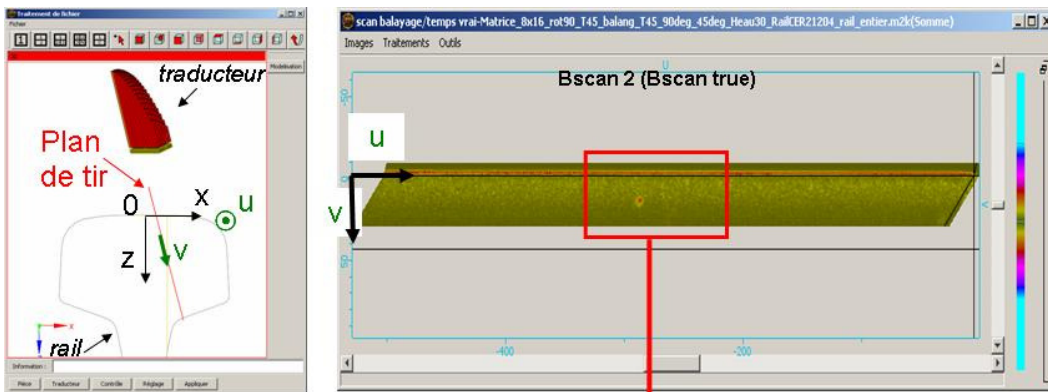
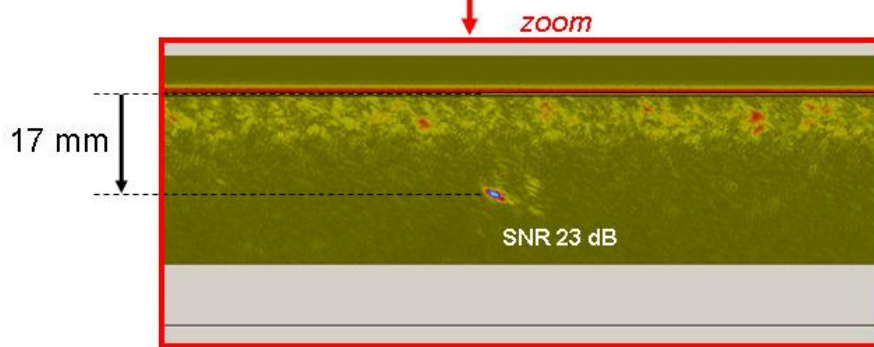
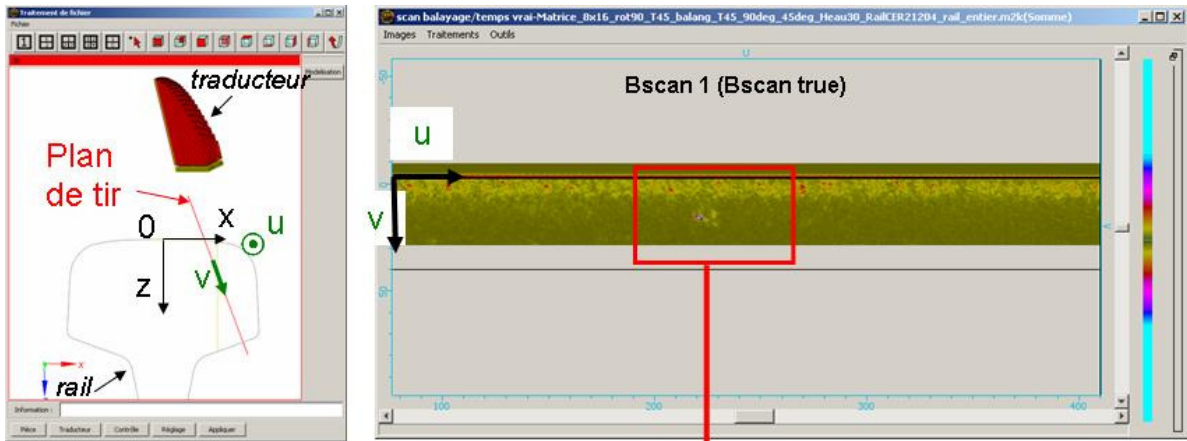


Figure 46 - Acquisition on sample CER212-04. Cscan and Bscan views for the 45°-shot/ rail axis

Figure 47 shows the results of acquisition obtained with the -10°-shot to the rail axis. The C-scan is time limited under the surface-breaking cracks echoes. We observe deeper echoes in the centre zone of the inspected area. These echoes are at least at 17.5 mm in depth with an extension of about 25 x 25 mm².





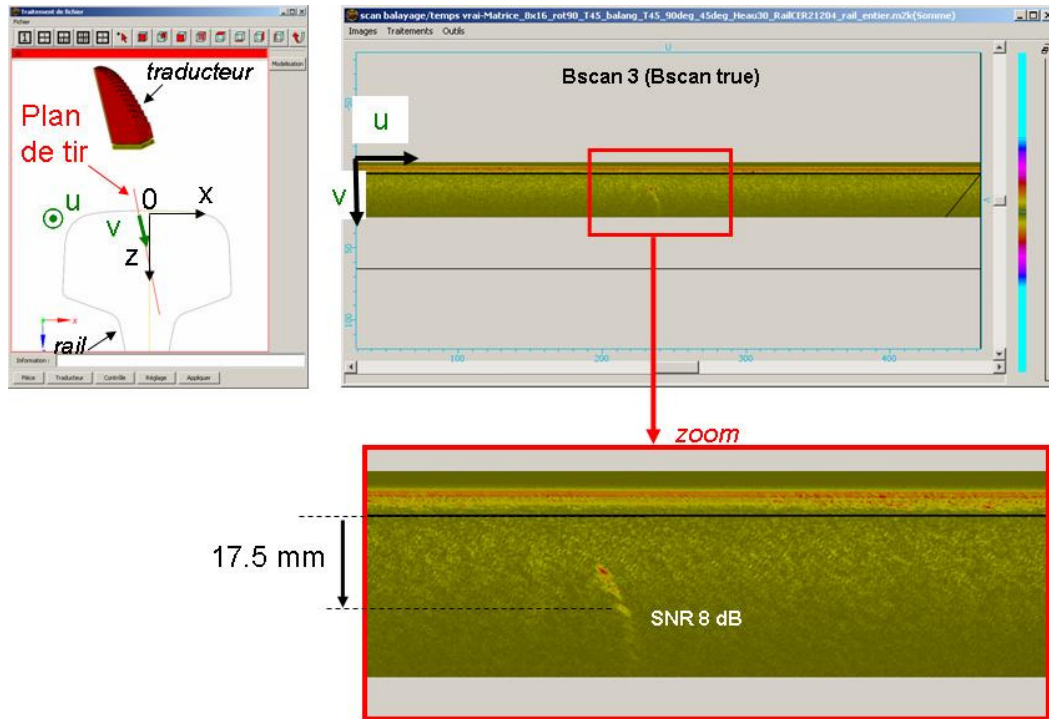


Figure 47 - Acquisition on sample CER212-04. C-scan (Time limited in depth) and B-scan views for the -10° -shot/ rail axis.

Sample 3506A

A visual observation shows that cracks are spaced from 15 to 30 mm. Acquisition was made above the damaged gauge corner on all the length of this sample i.e. 450 mm.

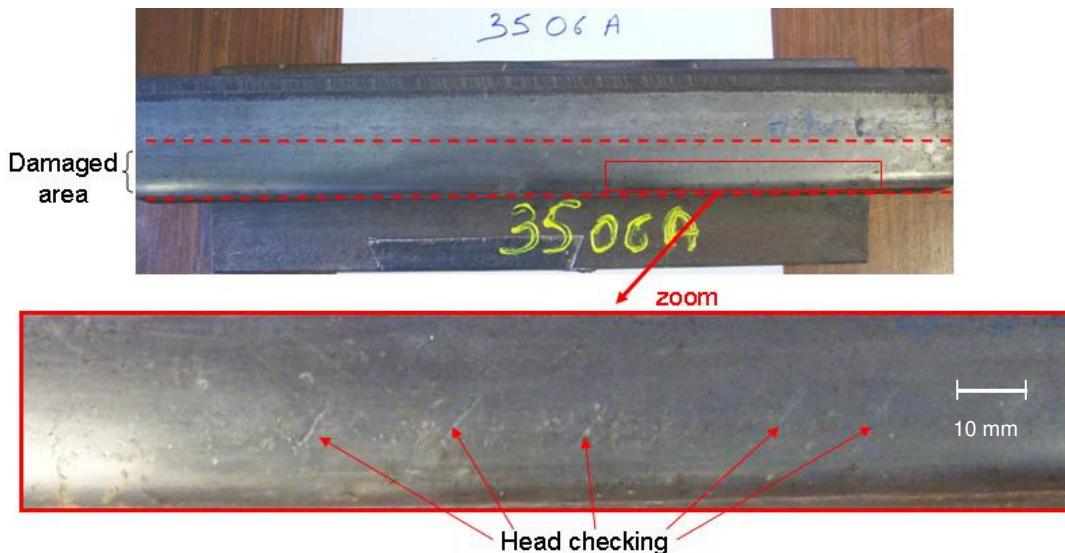


Figure 48 - Photo of the rail 3506A

The results of acquisition are shown in Figure 49. These images come from acquisition at 45° towards the longitudinal axis of the rail. The B-scan was extracted from the above C-scan at the dotted line. Surface-breaking cracks are detected with depths smaller or equal to 7.5 mm, except for a deeper one.

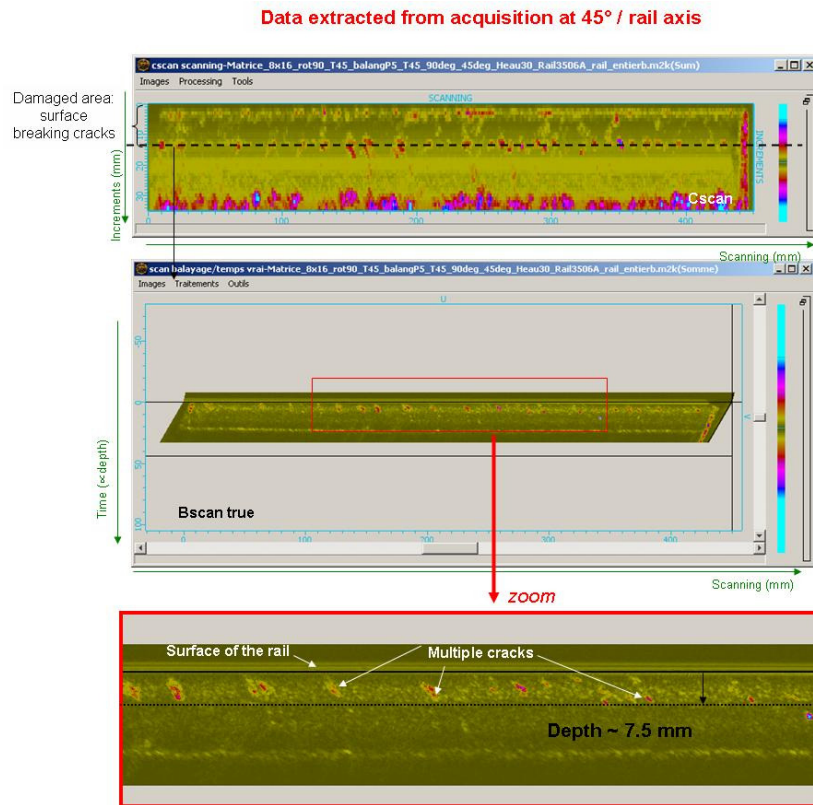


Figure 49 - Acquisition on sample 3506A. Cscan and Bscan views for the 45°-shot/ rail axis

Figure 50 shows results of acquisition obtained with the 25°-shot. The C-scan is time limited under surface-breaking cracks echoes. We observe then deeper echoes which are at least 10 mm in depth. Further reconstructions will be done to size more accurately these defects.

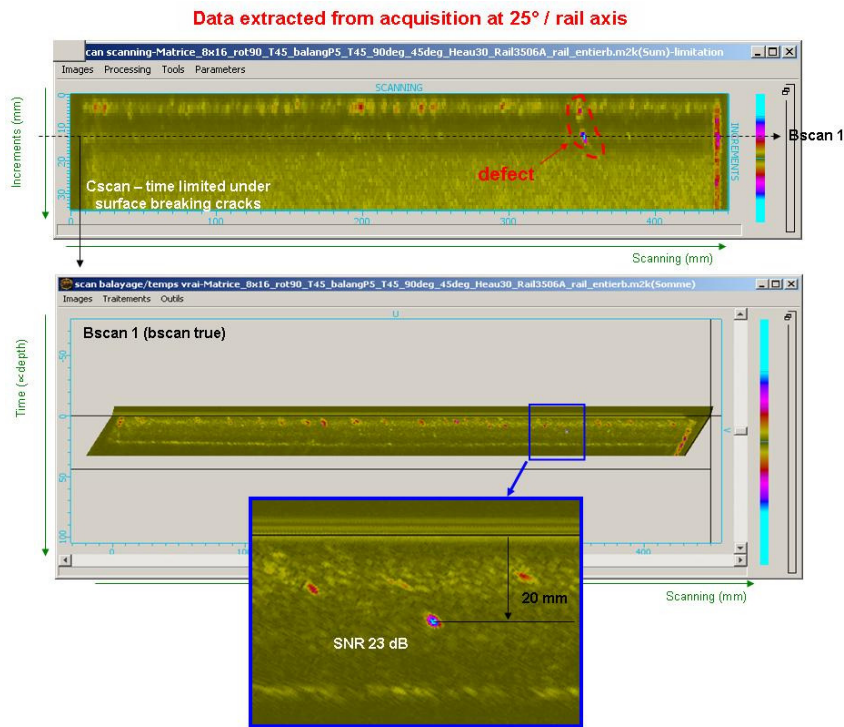


Figure 50. Acquisition on sample 3506A. C-scan (Time limited in depth) and B-scan views for the 25°-shot/ rail axis

Conclusion on innovative UT-method for head checking characterisation

3D-electronic scanning:

Inspections performed using this technique on real defects allow both surface breaking cracks and deeper cracks to be detected.

This first evaluation shows that the 3D-electronic scanning is a promising technique to characterise head checking in depth.

Head checking characterisation by Eddy current-inspection

The performance of different eddy current technologies has been evaluated in the framework of the project to inspect two kinds of mock-ups:

- Samples from the University of Birmingham.
- Rails from SNCF including Head checking

In the case of the Birmingham mock-ups, the given problem is to evaluate the ability of EC technologies to characterise flaws with different depths in the case of deep flaws and magnetic piece. Two technologies based on Transmit-Receive probes and magnetic flux leakage probes have been tested to tackle the problem.

In the case of SNCF mock-ups, the given problem is to evaluate the ability of EC technologies to detect thin flaws in a curved area. Technology based on flexible array probes has been tested to tackle the problem.

A description of these different probes is given below:

Description of the EC probes

Transmit-Receive probe

The probe is composed of two coils, an emitter coil and a receiver coil, with a diameter of a few mm.

A photograph and a picture of the probe are given in Figure 51. The operating frequencies are comprised between 100 Hz and 10 kHz. The distance between emitter and receiver is variable. The measurements were taken for different distances and frequencies to optimise the flaws detection and characterisation.

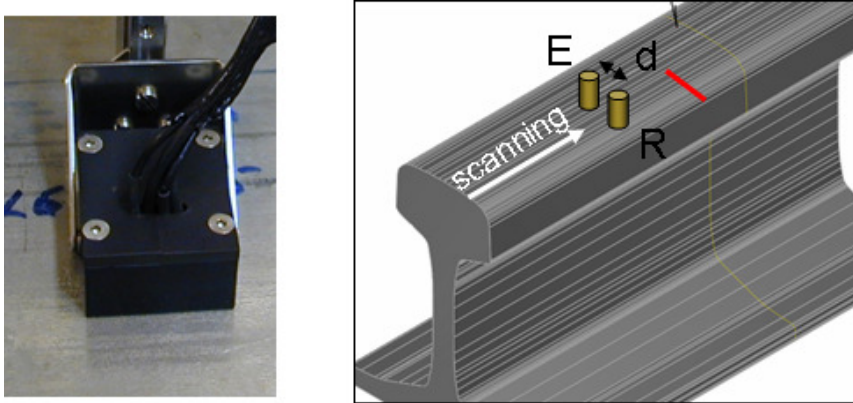


Figure 51 - Photograph and picture of the Transmit-Receive probe

The scanning is done with the emitter and receiver coils aligned with the flaw length: this configuration gives the best detection performances (right part of Figure 51).

Magnetic flux leakage probe

The probe is made of a U-shaped magnetic circuit with a bobbin coil emitter wound around, and a bobbin coil receiver placed between the poles of the magnet. A photograph of the probe is given in Figure 52.

In the operating mode, the U magnet imposes the course of the field lines created by the emitter. When a flaw is present, the current lines are disturbed (right part of Figure 52), and the corresponding signal is measured by the receiver. The design of the probe is well adapted to the inspection of deep flaws in magnetic pieces.

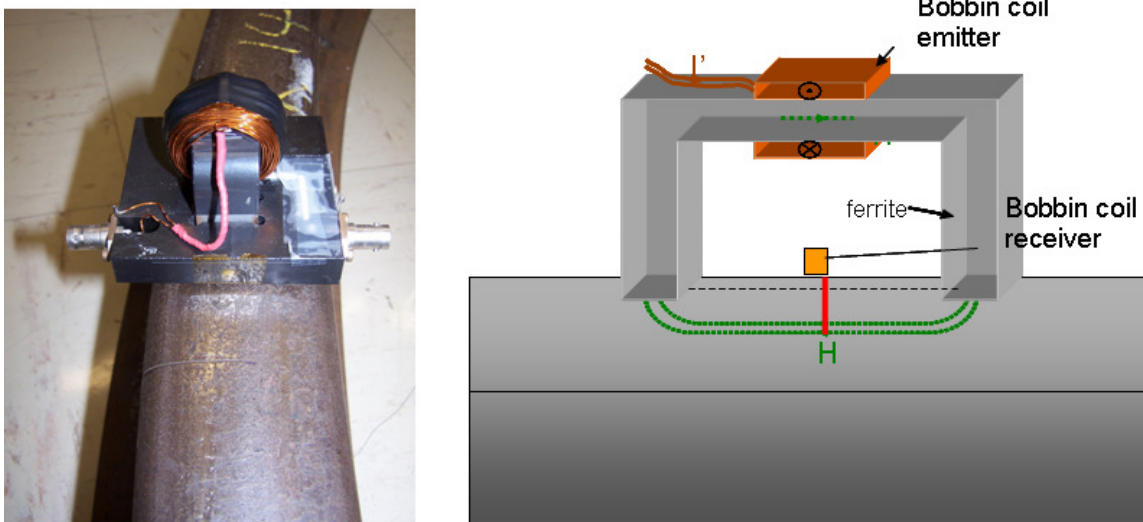


Figure 52 - Photograph and picture of the magnetic flux leakage probe

Flexible array probe

In the case of a curved surface, the use of flexible probe is motivated by the advantage that the probe can be kept in close contact with the surface of the piece during the inspection. Flexible technology ensures a good coupling between the probe and the piece, and a low sensitivity to the lift-off variation which could drastically

reduce the efficiency of the EC detection. This technology has been evaluated to determine its ability to detect thin surface cracks in the gauge corner of the SNCF samples (right part of Figure 53).

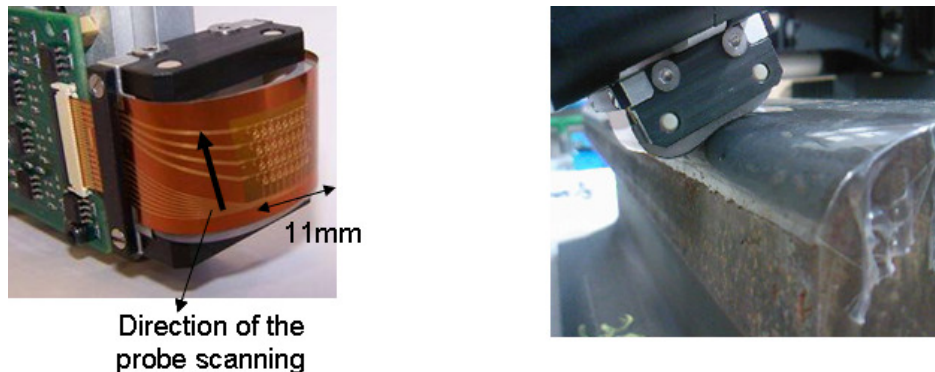


Figure 53 - Photograph of the flexible probe and evaluation in the case of the inspection of the gauge corner

The design of the flexible array probe is shown on Figure 53. Micro-coils are etched on a Kapton film which gives flexibility. This film is set on a silicon roll, with a size adapted to the inspected surface. Therefore, the sensor is always in close contact with the component. The lift-off variation problem is eliminated and complex shaped pieces can be inspected. Indeed, the minimal curve radius is less than 3 mm.

The design of the probe was optimised by simulation to detect small surface breaking flaws. Simulations, performed with CIVA software [36], drive to a pattern which contains two coils, an emitting one and a receiving one. Internal and external diameters, distance between coils as well as the frequency are the parameters which have been optimised to lead to an original pattern. The originality comes from the overlapping of the two coils. For this reason, coils are etched on both sides of the Kapton film.

This pattern is high sensitive and very efficient in the detection of few hundred of micrometers length defects [37].

The SNCF samples have been inspected by a 32 elements flexible probe. Each element is similar to the pattern described before and therefore the probe is composed with 64 coils (32 emitting and 32 receiving). The diameter of the coils is around 1mm. Every emitting coil is set on one side of the Kapton film and the receiving ones on the opposite side. The distance separating two patterns is 350µm that gives a high spatial resolution to the probe. Because of this density, patterns are set on 4 staggered lines. Figure 53 presents a photo of the probe. A 11 mm width strip can be inspected. Amplifiers have been put as close as possible to the coils so as to improve the signal to noise ratio.

Description of the experimental results

Transmit-receive probe and magnetic flux leakage probe

The performances of the probes have been evaluated for rails 1 and 3 of the University of Birmingham.

Figure 54 and Figure 55 illustrate the EC signal obtained respectively for a manual scanning of the transmit-receive and magnetic flux leakage probes above rail 1. The optimum frequency is 290Hz. These results show good detection of the flaws with an increase of magnitude according to the flaw height (Table 4). In the case of the magnetic flux leakage probe, large variations are obtained, which allows an in-depth flaw classification.

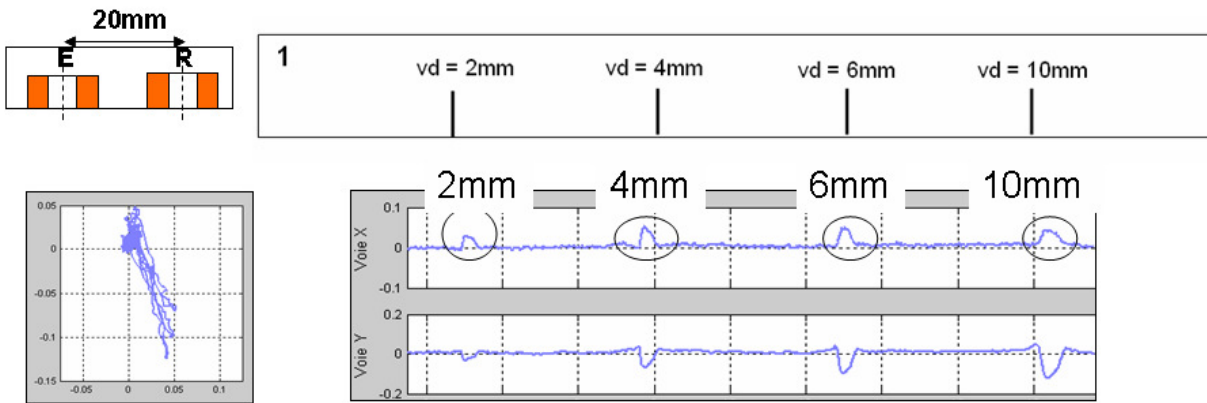


Figure 54 - Eddy current signal obtained at 290Hz with transmit-receive probe in the case of the detection of the flaws located in the rail 1

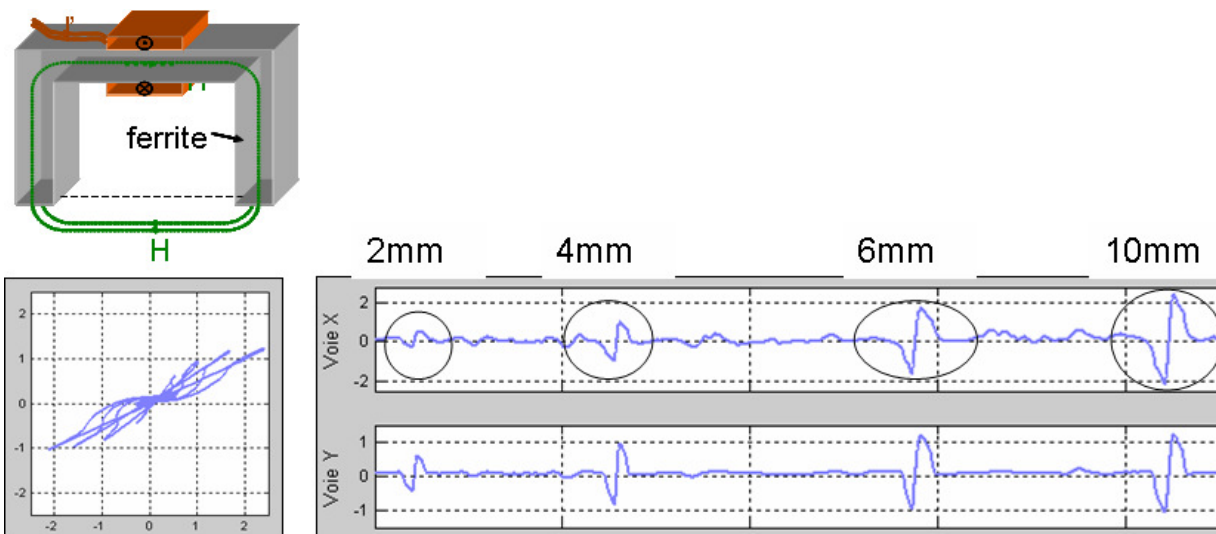


Figure 55 - Eddy current signal obtained at 290Hz with magnetic flux leakage probe in the case of the detection of the flaws located in the rail 1.

Flaw height (mm)	EC signal magnitude (V)	
	Transmit-receive probe	Magnetic flux leakage probe
2	0.04	1.3
4	0.09	2.7
6	0.12	3.4
10	0.14	5.1

Table 4 - EC signal magnitude values obtained for the detection of flaws in rail 1 in the case of transmit-receive and magnetic flux leakage probes

This illustrates the EC signal obtained for manual scanning of the magnetic flux leakage probes above rail 3. Good detection of the flaws, with an increase in magnitude according to the flaw height, is also observed in this case.

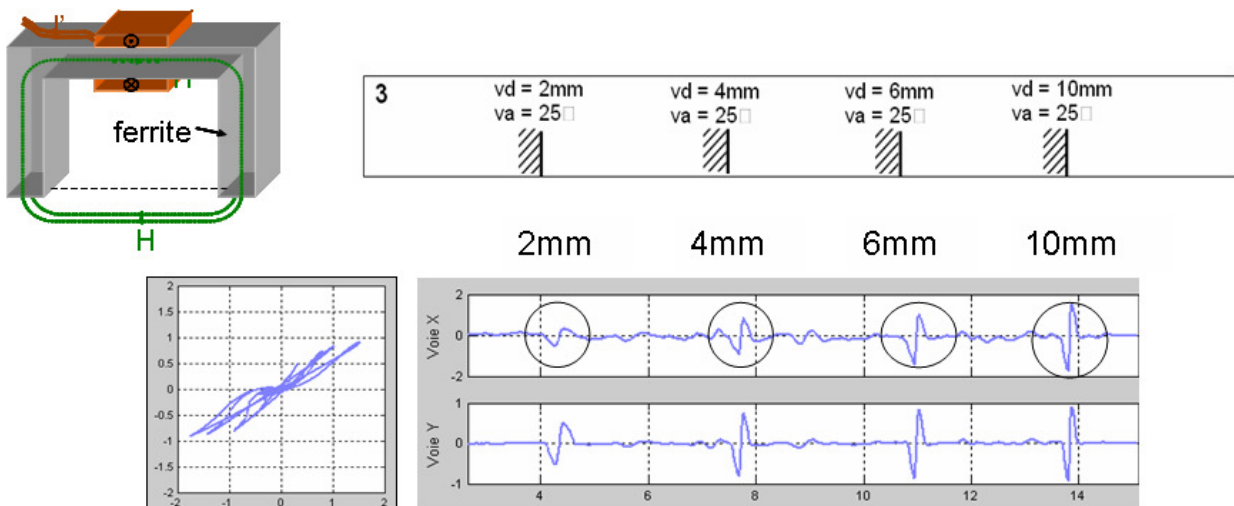


Figure 56 - Eddy current signal obtained at 290Hz with magnetic flux leakage probe in the case of the detection of the flaws located in rail 3.

Magnetic flux leakage probe	
Flaw Height (mm)	EC signal magnitude (V)
2	1.3
4	2.3
6	3
10	3.7

Table 5 EC signal magnitude values obtained for the detection of flaws in rail 3 in the case of magnetic flux leakage probe

Flexible array probe

The performance of the flexible array probe has been evaluated in two rail mock-ups from SNCF, whose references are 3506A and CER 212_04.

The CSCAN mapping obtained at 2 MHz and shown in Figure 57 corresponds to the EC examination of the cracked area during the inspection of the gauge corner of the 3506A rail mock-up. The small cracks show a very good signal to noise ratio.

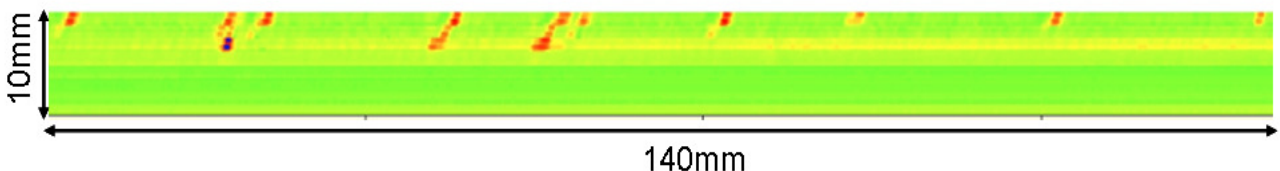


Figure 57 - CSCAN mapping obtained at 2MHz for eddy current examination of the cracked area of the 3506A rail mock-up

In the CER 212_04 mock-up, a network of many thin flaws is present and clearly visible on the top part of Figure 58. The CSCAN mapping obtained at 2 MHz and shown in the bottom part of Figure 58 corresponds to the EC examination of the cracked area during the inspection of the gauge corner. The network of small cracks is easily detected by the flexible probe.

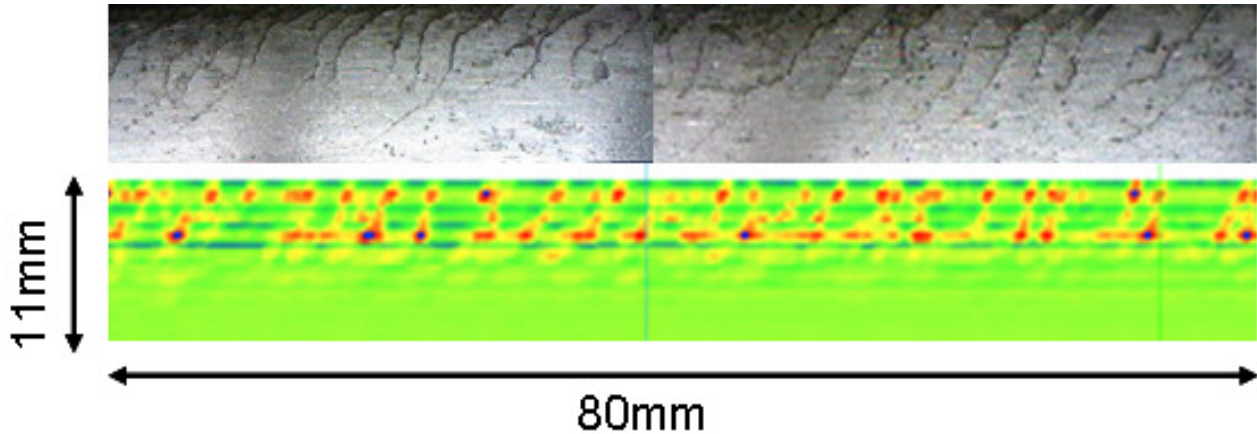


Figure 58 - CSCAN mapping obtained at 2MHz for eddy current examination of the cracked area of the CER 212_04 rail mock-up

The experimental data shows good results for detection obtained with the flexible sensor for small cracks. The flexible probe is particularly well adapted to the detection of thin flaws of a few hundred micrometers located in complex geometries (in particular a radius of variable curvature).

Detection of defects in rails of railroads by laser ultrasonic techniques

Laser Ultrasonic techniques are currently being evaluated by some railway companies throughout the world. This document includes a comprehensive state-of-the-art review of laser based methods which is included in Appendix 1. In addition, as part of the work of WP4.4 the laser techniques have been tested by LMP using real rail defects in line with the other methods considered.

Experimental set-up and sample

A laser ultrasonic system has been developed on an optical table at LMP to demonstrate the abilities of the laser ultrasonic technique for the nondestructive testing of a rail (Figure 59). The radiation of a Q-switched Nd:YAG laser at a wavelength of $1.06 \mu\text{m}$ is used for the excitation of surface acoustic waves on the surface of the rail. The energy of laser pulses with duration of 10ns and a repetition rate at 50 Hz is adjusted to provide the thermoelastic regime of acoustic wave excitation. To control the wavelength of the generated surface wave the size of the excitation source is varied by means of a slit variable width 0.5-10 mm. Then the surface wave propagates a distance of about 4 cm along the surface of the rail to be probed by a laser interferometer (TEMPO, Bossa Nova Technologies, 0.2-120 Mhz). This interferometer is quite sensitive to changes of the speckle picture in time. For this reason, it is acoustically isolated from the optical table to avoid mechanical vibrations. The radiation of the interferometer is focused on the surface of the rail by a 20 cm lens. Then the same lens is used to collect the radiation of the scattered light. To improve the sensitivity of photodetection, the surface of the rail was polished.

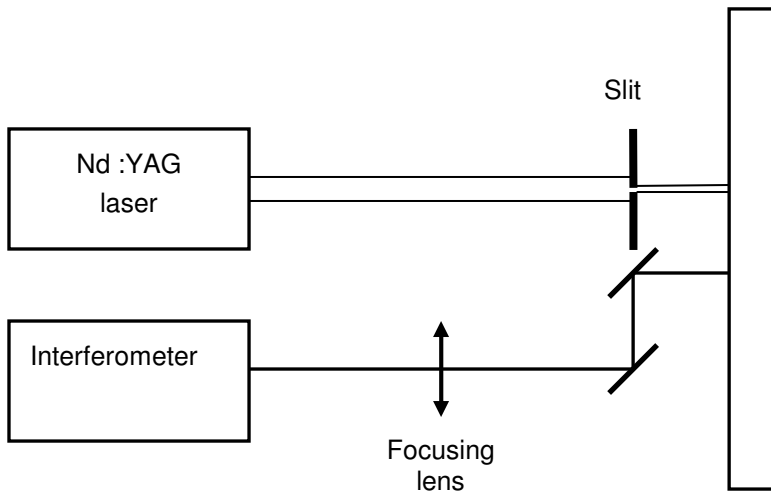


Figure 59 - Experimental set-up for the study of defects in rail

The output high-frequency signal of the interferometer is detected by the oscilloscope. The 1 m rail was studied with a marked unknown defect approximately in the centre. To test the laser ultrasonic technique several artificial defects (~ 1mm thick gaps) have been made on the surface of the rail with a saw. The configuration of the defects is shown in Figure 60.

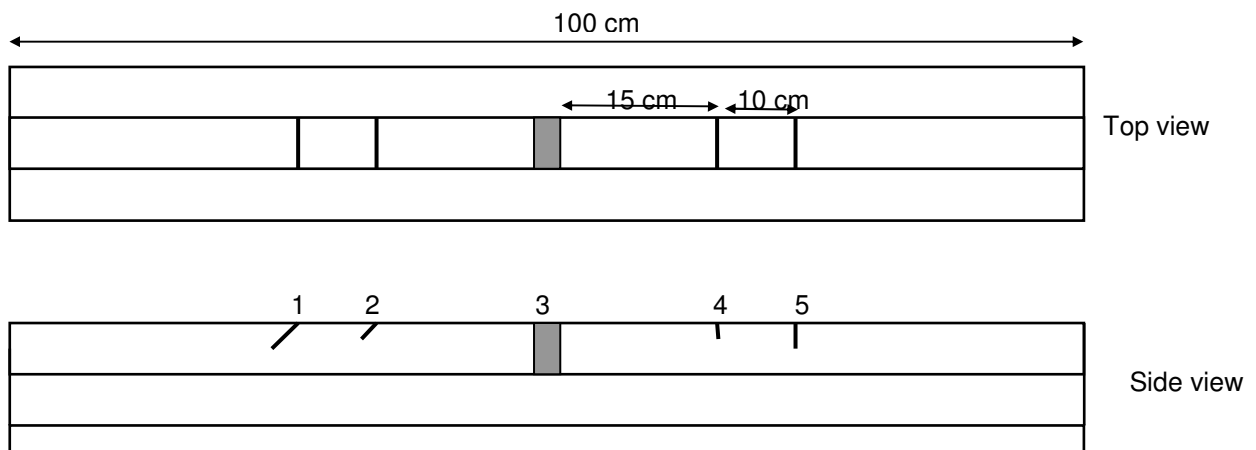


Figure 60 - Configuration of defects on the rail (Table 61)

Number of defect	Depth, mm	Angle to the surface, deg
1	6	45
2	3	45
3	unknown	unknown
4	3	90
5	6	90

Table 6 - Parameters of the defects

Experimental result on an artificial defect

First, the surface wave was observed in the part of the rail free from the defects (Figure 61A).

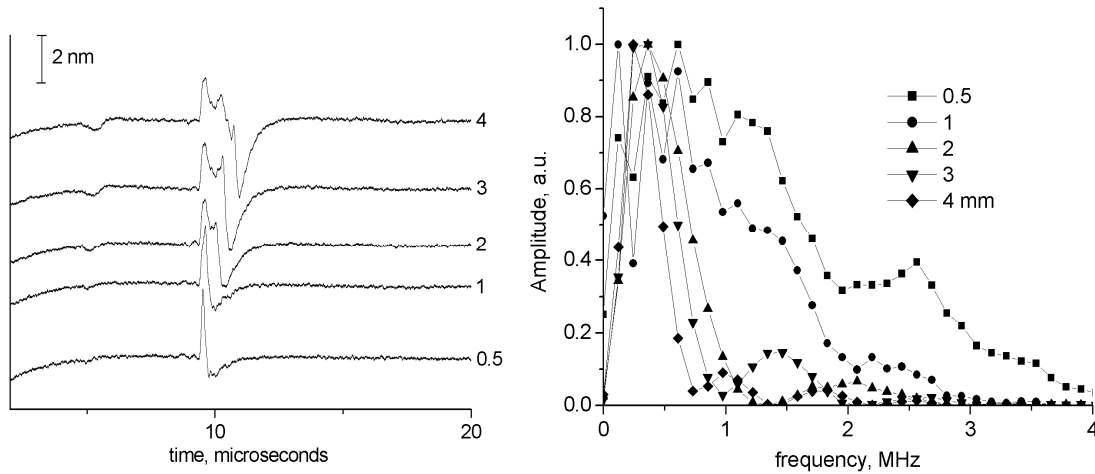


Figure 61 – A. Surface wave. The width of line source (mm) is on the right part of each curve / B. Corresponding spectra normalized on their maximum.

The width of the line-source was varied within the range 0.5-4 mm. It is clear from this picture that the duration of the photoexcited surface wave increases with the rise of line-width. Corresponding spectra provide a good confirmation of it (Figure 61 B). It is clear that the amplitude of high frequency components decreases as the line-width is made broader.

Using the described technique the surface wave propagation through vertical defects of 3 and 6 mm depth has been studied (defects 4 and 5 in Figure 60, correspondingly). The defects were located approximately at mid distance between pump and probe beam.

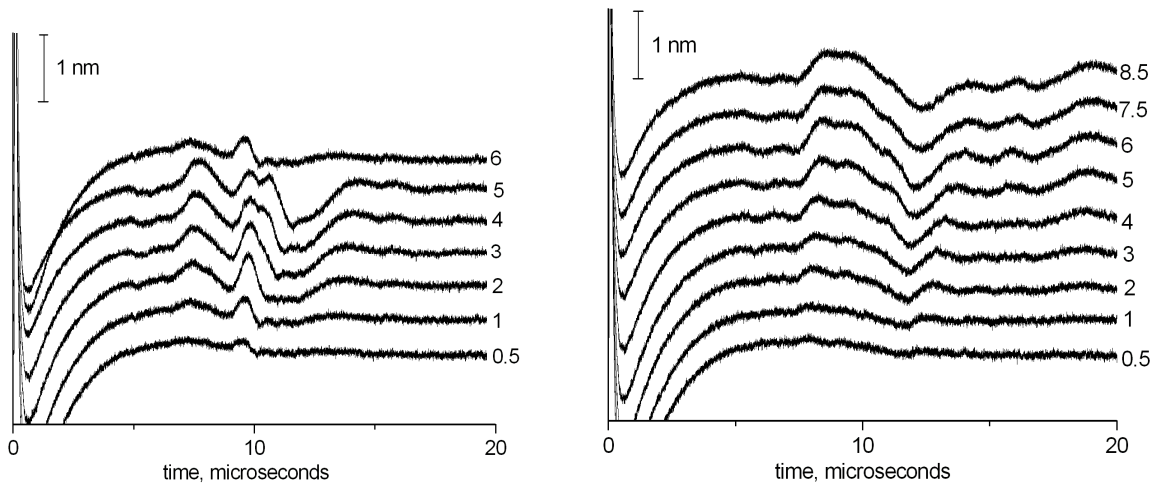


Figure 62 - Surface wave on the rail with 3 (A) and 6 mm (B) deep vertical defect. The width of the line-source in mm is marked on the right side of each curve

It is clear from the comparison of waves in Figure 61 (without defect) and Figure 62 (with defect) that the amplitude of the detected surface wave is ~10 higher in case of absence of defect. The transmitted surface wave amplitude increases with the wavelength increase. A maximum amplitude is achieved when the wavelength approximately equals the defect depth. It is about 3 and 6 mm, correspondingly, in Figure 62 A and B a good match with the size of the defect.

Defects with depth 3 (defect 2) and 6 mm (defect 1) at 45 deg to the surface were studied for two configurations. The only difference between these two configurations was the direction of propagation of the surface wave according to the angle of the defect. They were achieved by the adjustment of the position of the probe on one or another side of the defect (Figure 63).

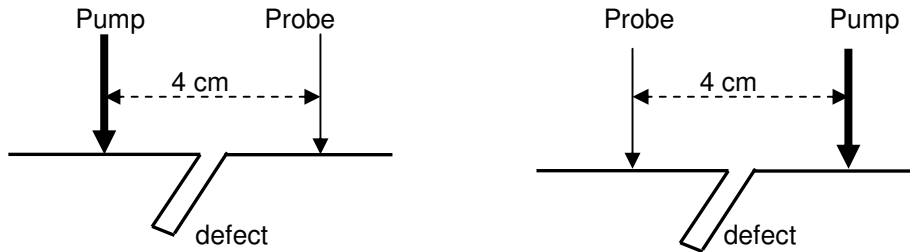


Figure 63 - First (A) and second (B) configuration of the defect probing by the surface wave

The surface waves detected in the first and second experimental configuration are shown in Figure 64 and Figure 65, respectively. There is no evidence of clear dependence of surface wave pulse shape on the experimental configuration.

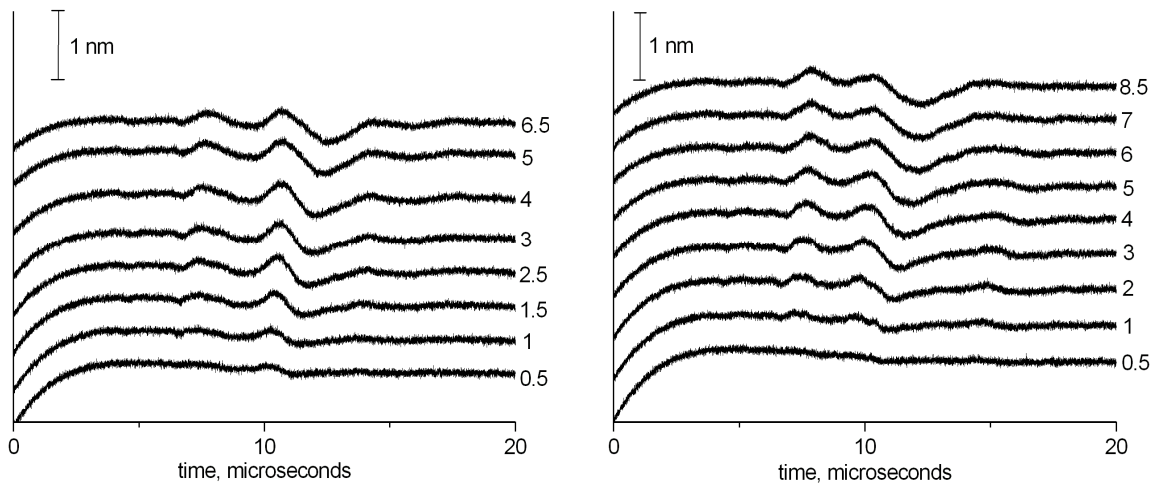


Figure 64 - Surface wave on the rail with 3 (A) and 6 mm (B) deep defect (45 deg., first configuration). The width of the line-source in mm is marked on the right side of each curve

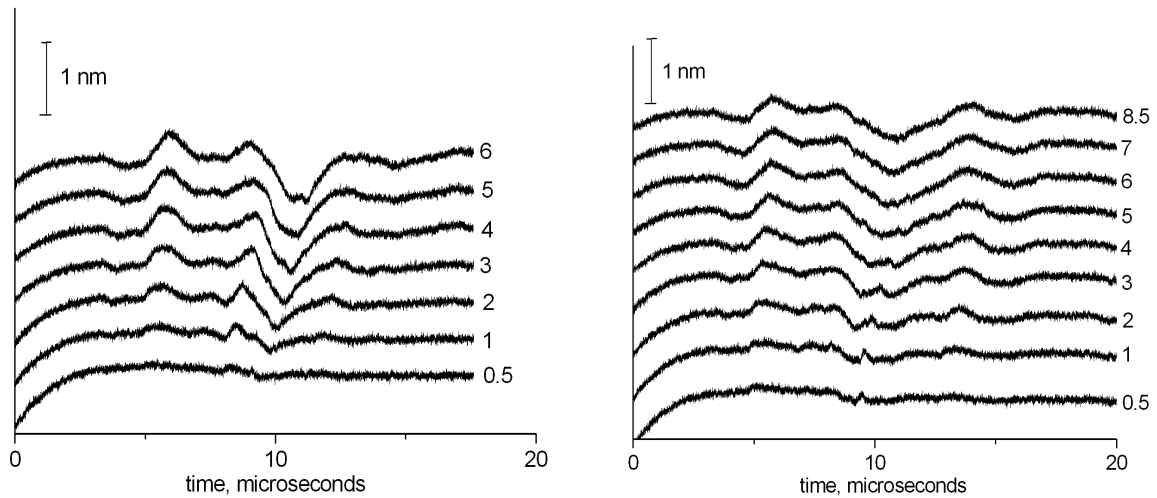


Figure 65 - Surface wave on the rail with 3 (A) and 6 mm (B) deep defect (45 deg, second configuration). The width of the line-source in mm is marked on the right side of each curve

Experimental result on an unknown defect

Then, experiments aimed at detection of the unknown defect were performed. This defect was not visible visually. Therefore, the exact location of this defect was unknown. The approximate position is marked on the rail with a yellow line. A clear echo of the reflection from the defect was obtained by probing nearby this line (Figure 66). This echo is located before the surface wave. Therefore it could be associated with the reflection of a longitudinal wave from the crack in the volume of the rail. To determine the exact position and size of this crack it is necessary to perform an accurate scan of the rail nearby the area of the crack.

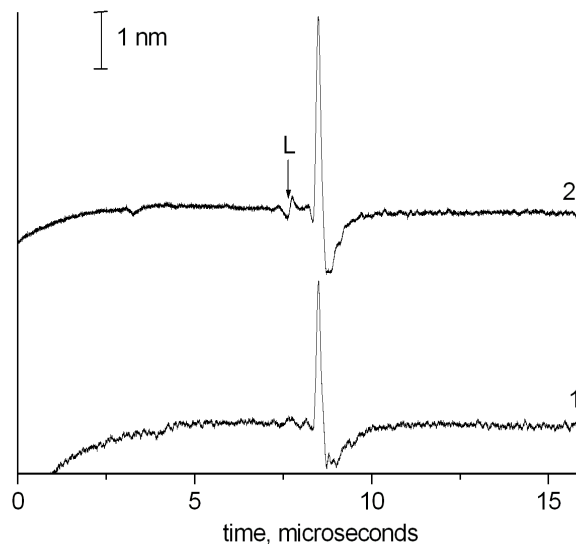


Figure 66 -Acoustic pulses in rail without (1) and with defect (2). The echo from the defect is marked as L

Conclusion on laser ultrasonic techniques

In conclusion, the following significant results have been obtained during test experiments with the rail:

1. Nanosecond ultrasonic laser set-up was prepared for non-destructive testing of rail parts on the optical table.
2. Several artificial defects made on the rail surface were successfully detected.

3. The influence of defect length and angle on surface acoustic wave has been qualitatively studied.
4. It has been shown that the depth of a defect could be derived from the experiment performed with variable wavelength of the surface wave.
5. A promising ability for the nanosecond ultrasonic technique to be used for the testing of defects in rails has been demonstrated.

Head checking characterisation by ACFM inspection

Alternating Current Field Measurement (ACFM) is an electromagnetic inspection method which is now widely accepted as an alternative to magnetic particle inspection in the Oil and Gas Industry, both above and below water. Although developed and patented by TSC Inspection Systems Ltd. initially for routine inspection of structural welds, the technology has been improved further to cover broader applications across a range of industries. Figure 67 shows the theory behind the operation of the ACFM sensor. Increases in inspection speeds (from around one metre to a few metres per minute), application to non-planar crack morphologies and extension of sizing models to accommodate different crack types have all been achieved¹⁻³.

The ACFM technique is capable of both detecting and sizing (length and depth) surface breaking cracks in metals based on the thin-skin theory developed by Lewis, Michael, Lugg, and Collins (LMLC theory)¹. Under certain conditions ACFM can be applied for the detection of near-surface defects, however, this strongly depends on the electromagnetic properties of the metal under inspection. Typically, the maximum skin depth achieved with ACFM systems varies from 0.1mm for carbon steels to 6mm for stainless steel.

Fundamentals of the ACFM technique

The technique is based on the principle that an alternating current (AC) can be induced to flow in a thin skin near the surface of any conductor. By introducing a remote uniform current into an area of the component under test, when there are no defects present the electrical current will be undisturbed. If a crack is present the uniform current is disturbed and the current flows around the ends and down the faces of the crack. Because the current is an alternating current it flows in a thin skin close to the surface and is unaffected by the overall geometry of the component.

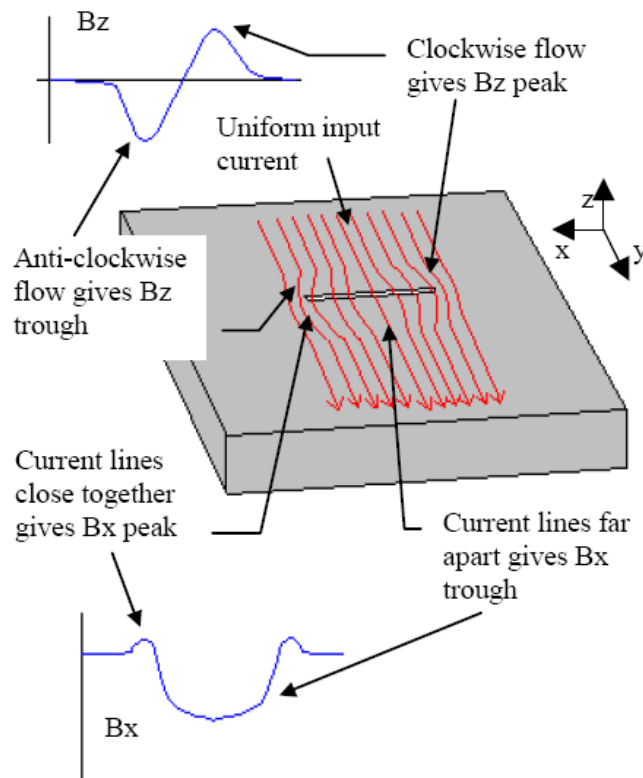


Figure 67 - Definition of field directions and co-ordinate system used in ACFM

Associated with the current flowing in the surface is a magnetic field above the surface which, like the current in the surface, will be disturbed in the presence of a defect. An important factor of the ACFM technique is its capability to relate measurements of the magnetic field disturbance to the size of defect that caused that disturbance. The breakthrough came from a combination of research studies, which provided mathematical modelling of the magnetic field rather than electrical fields, and advances in electronics and sensing technology^{1,3}. Despite the fact that the magnetic field above the surface is a complex 3D field, it is possible, by choosing suitable orthogonal axes, to measure components of the field that are indicative of the nature of the disturbance and which can be related to the physical properties of any cracks present⁴. Figure 67 presents a plan view of a surface breaking crack where a uniform AC current is flowing. The field component denoted B_z responds to the poles generated as the current flows around the ends of the crack introducing current rotations in the plane of the component. These responses are principally at the crack ends and are indicative of a crack length. The field component denoted B_x responds to the reduction in current surface density as the current flows down the crack and is indicative of the depth of the defects. Generally, the current is introduced perpendicular to the expected direction of cracking. In practice, special probes have been developed which contain a remote field induction system, for introducing the field into the component, together with special combined magnetic field sensors that allow accurate measurement of the components of the magnetic field at the same point in space. The probe requires no electrical contact with the component and can therefore be applied without the removal of surface coatings or grime.

In contrast to eddy current sensors that require to be placed at a close (<2mm) and constant distance from the inspected surface, a maximum operating lift-off of 5mm is possible without significant loss of signal when using ACFM probes. This is due to the fact that at small lift-off the signal strength diminishes with the square of lift-off, not with its cube which is the case for eddy current sensors. This enables the ACFM technique to cope with much greater lift-off and thicker non-conductive coatings. For larger threshold defects a higher operational lift-off (>5mm) is possible⁵.

ACFM probes are available as standard pencil probes and multi-element array probes. These probes can be customised to optimise inspection of particular structural components and maximise the Probability of Detection (PoD) of critical-sized defects. ACFM pencil probes can detect surface-breaking defects in any orientation. Nonetheless, in order to size defects, they need to lie between 0° - 30° to the direction of travel of the probe. This drawback is overcome in ACFM arrays by incorporating various field inducers in order to allow a field to be introduced within the inspected surface in other orientations. This is particularly useful in situations where the crack orientation is unknown or variable. In this case, additional sensors, denoted B_y , are also incorporated in order to take full advantage of the additional input field directions².

To make best use of an array probe, it is necessary to switch through the sensors as quickly as possible in order to allow rapid inspection. However, there are inherent limitations to this including switching settling times, data transfer rates and limitations in the sampling of a 5kHz signal. With conventional analogue electronics these factors limit the speed of scan for array probes to around 0.15m/s for a single field 16-channel array. In order to improve the applicability of the ACFM array probes a high-speed instrument has been developed which allows scanning speeds 4-5 times faster than with conventional ACFM instrument. This has been achieved by increasing the energising frequency from 5kHz to 50kHz together with modifications to the signal processing electronics².

ACFM walking stick array

Following the experimental work on the train axles, it became evident that an ACFM system could be deployed to both detect and size RCF cracking on rails. This led to the development of a pedestrian-operated ACFM walking stick as shown in Figure 68. The incorporated ACFM array has been shaped to conform to the shape of the head of the rail. This allows the application of the ACFM system in both new and worn rails. The inspection across the rail head is carried out by sequentially scanning across the group of sensors enabling the uninterrupted inspection of the rail.

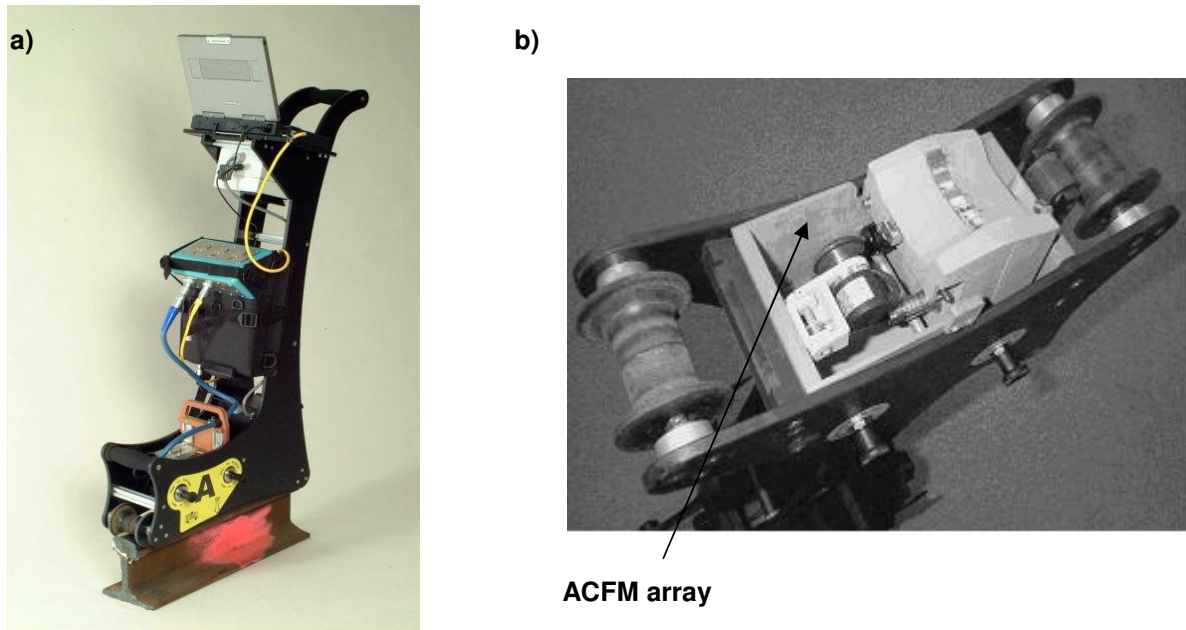


Figure 68 - a) The ACFM walking stick, b) the under-side of the walking stick.

RCF head checks are often inclined to the surface, penetrating initially at a shallow angle of approximately 15° - 30° until they reach a characteristic depth and turn down into the railhead at an angle of approximately 60° . Figure 69 shows an optical micrograph taken from a cross section through the railhead of a typical RCF crack¹⁰. Based on the data acquired through extensive metallographic work on rails with RCF cracking, a customised software package incorporating the appropriate defect sizing algorithms was developed in order to enable the automated sizing of the RCF cracks that were detected with the walking stick².

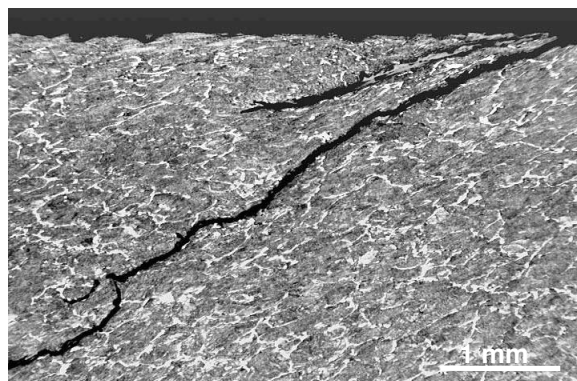


Figure 69 - Optical micrograph of a typical RCF crack¹⁰

By increasing sampling rates to 50kHz the walking stick system achieved scanning speeds of 0.75m/s. It should be stressed here that sufficient data must be collected to not only detect a defect but also to determine its severity. Further experiments are currently under way in an effort to develop a high-speed ACFM sensing system for the detection and quantification of RCF in rails. The initial results of this work are presented next.

ACFM tests on rails containing artificially induced surface defects

A 3.6m diameter spinning rail rig capable of rotating at speeds between 1-80 km/h has been purchased by the University of Birmingham as part of an Advantage West Midlands (AWM) equipment grant. The rig has been previously used to investigate the use of lasers to remove the build up of leaf mould on the surface of

rails and to help in the development of equipment to measure the temperature of rails from in-service trains. The spinning rail rig, shown in figure 50, is unique in the world and provides a means of evaluating various NDT technologies in a laboratory environment with 'close to real world' conditions.



Figure 70 - The spinning rail rig at Birmingham University

A special set of eight 1.41m long rails containing artificially induced defects have been produced, including half-face slots machined normal to the railhead surface, clusters of angled slots, and pocket defects more typical of real defects. The defects have been induced using spark erosion. The shapes and sizes of the induced defects were chosen in such a way as to enable their use as calibration samples for various NDT technologies.

Figure 71 shows a plan view schematic of sample rails and induced defects. The induced artificial 'pocket slot' defects contained in rail samples designated #7 and #8 are the ones that closely resemble actual RCF cracks.

Initial ACFM tests were carried out at slow speeds (0.1m/s) with the walking stick ACFM array in order to evaluate its detection performance. The ACFM system successfully detected all artificially induced defects. Figure 52 shows the C-scan image obtained for rail 8. The upper part of the C-Scan in figure 52 shows in blue colour the intensity of the recorded signal for the pocket-shaped defects with regards to their depths, while the lower part of the C-scan shows in blue and red the intensity of the recorded signal with regards to the surface lengths of the slots.

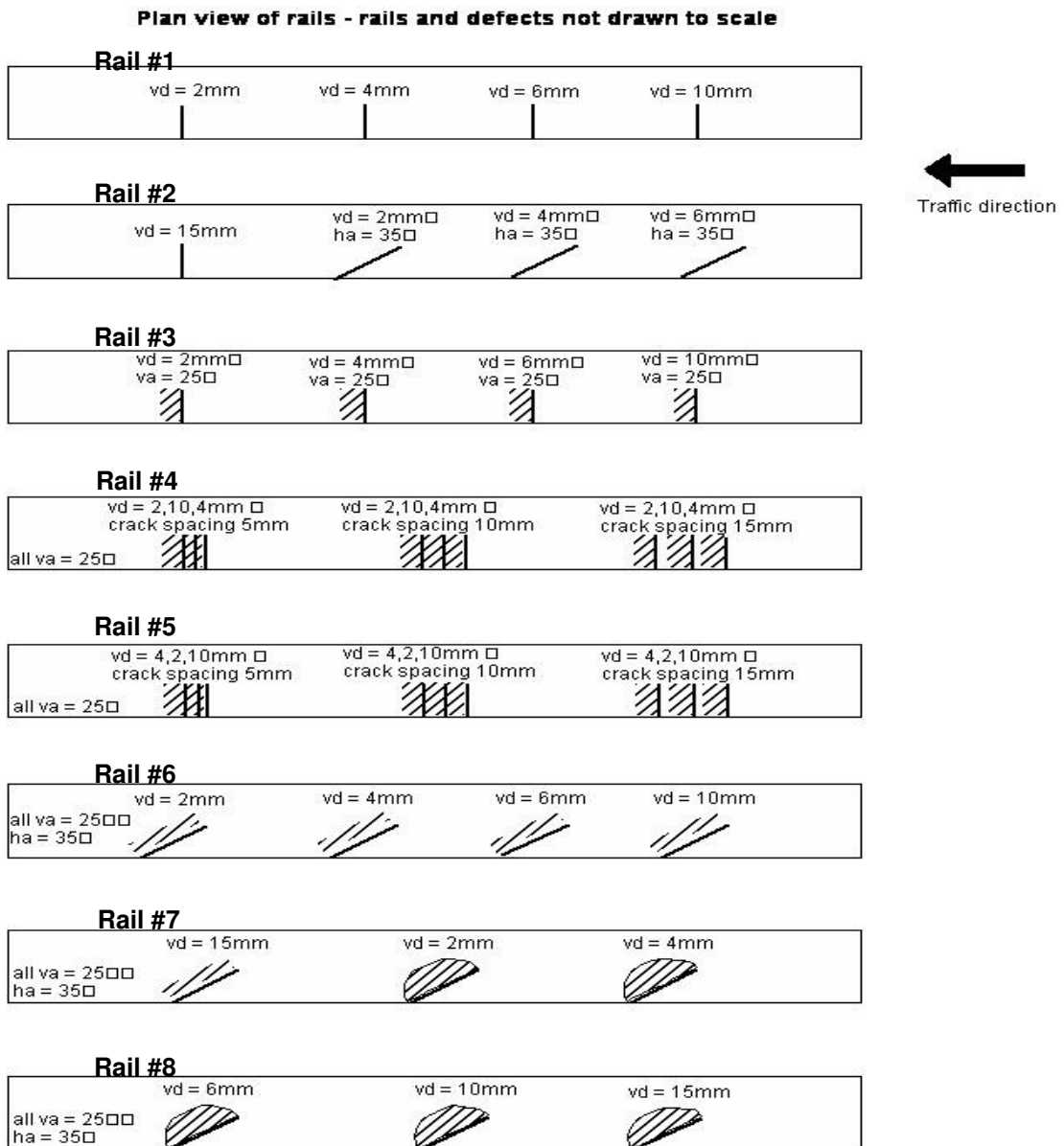


Figure 71 - Plan view schematic of sample rails and induced defects (vd = vertical depth, va = vertical angle, ha = horizontal angle)

The system automatically quantifies and displays the largest defect for every 0.98m (1 yard) of inspected rail. The calculated depths obtained through the automated quantification for the artificially induced pocket-shaped defects in rails #7 and #8 are shown in Table 7.

Rail sample #	Actual defect depth	ACFM depth	calculated
7	2.0	5.5	
7	4.0	8.8	
8	6.0	9.4	
8	10.0	9.6	
8	15.0	9.9	

Table 7 - Actual and ACFM calculated depths for the pocket-shaped artificial defects

It should be noted that the software has been optimised to calculate the length and depth of actual RCF defects and therefore the accuracy for the artificially induced pocket-shaped defects has not been as good as that achieved for actual defects.

It seems that although the correct rankings are obtained for the defects with respect to their depth, the system tends to oversize the shallow ones. It is very likely that this discrepancy could be related to the slot opening (>0.7mm) at the surface of the pocket-shaped defects, which is quite large for the size of the ACFM probe employed in these tests.

It is unlikely that the discrepancy is related to the shape of the defects since they resemble actual RCF cracks. It is intended that new samples containing pocket-shaped artificial defects with smaller slot openings are produced in order to confirm the reason for the discrepancies seen in the quantification of the artificially induced defects.

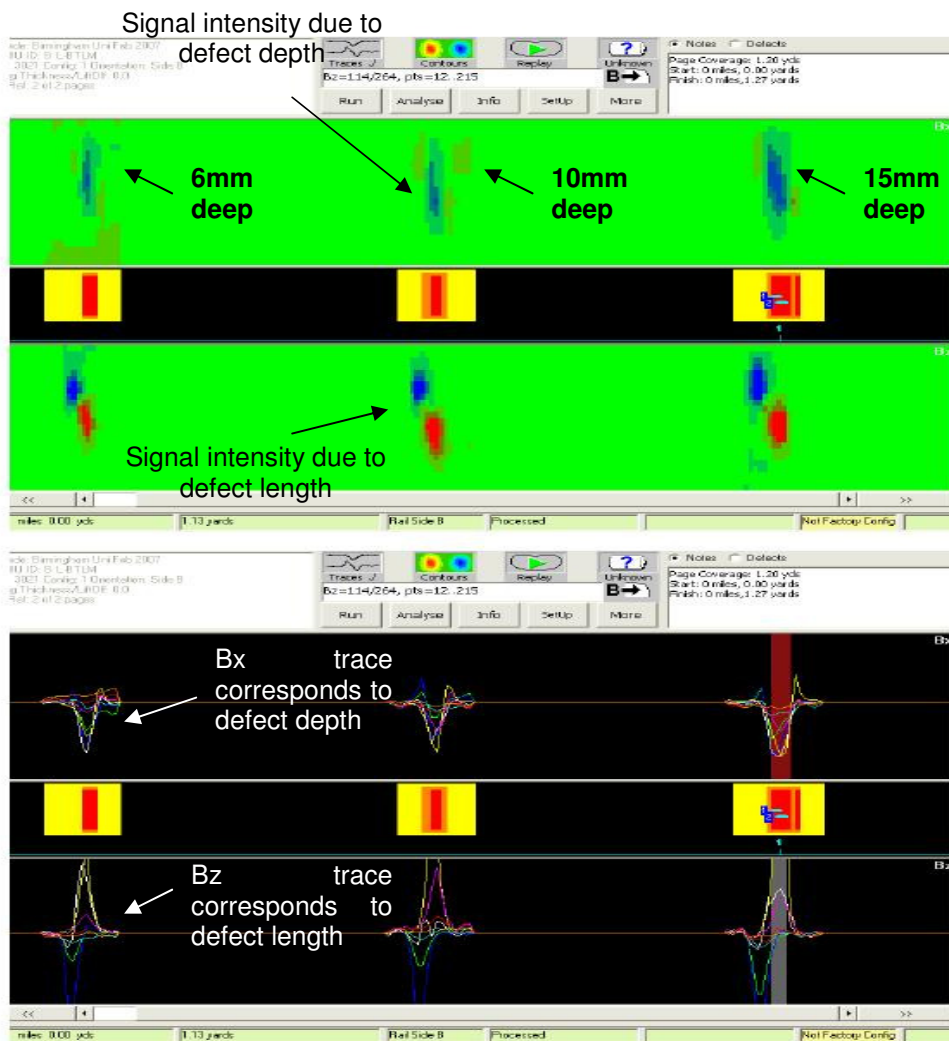


Figure 72 - ACFM C-scan obtained for rail 8.

ACFM C-scans for the rest of the test rails are shown next:

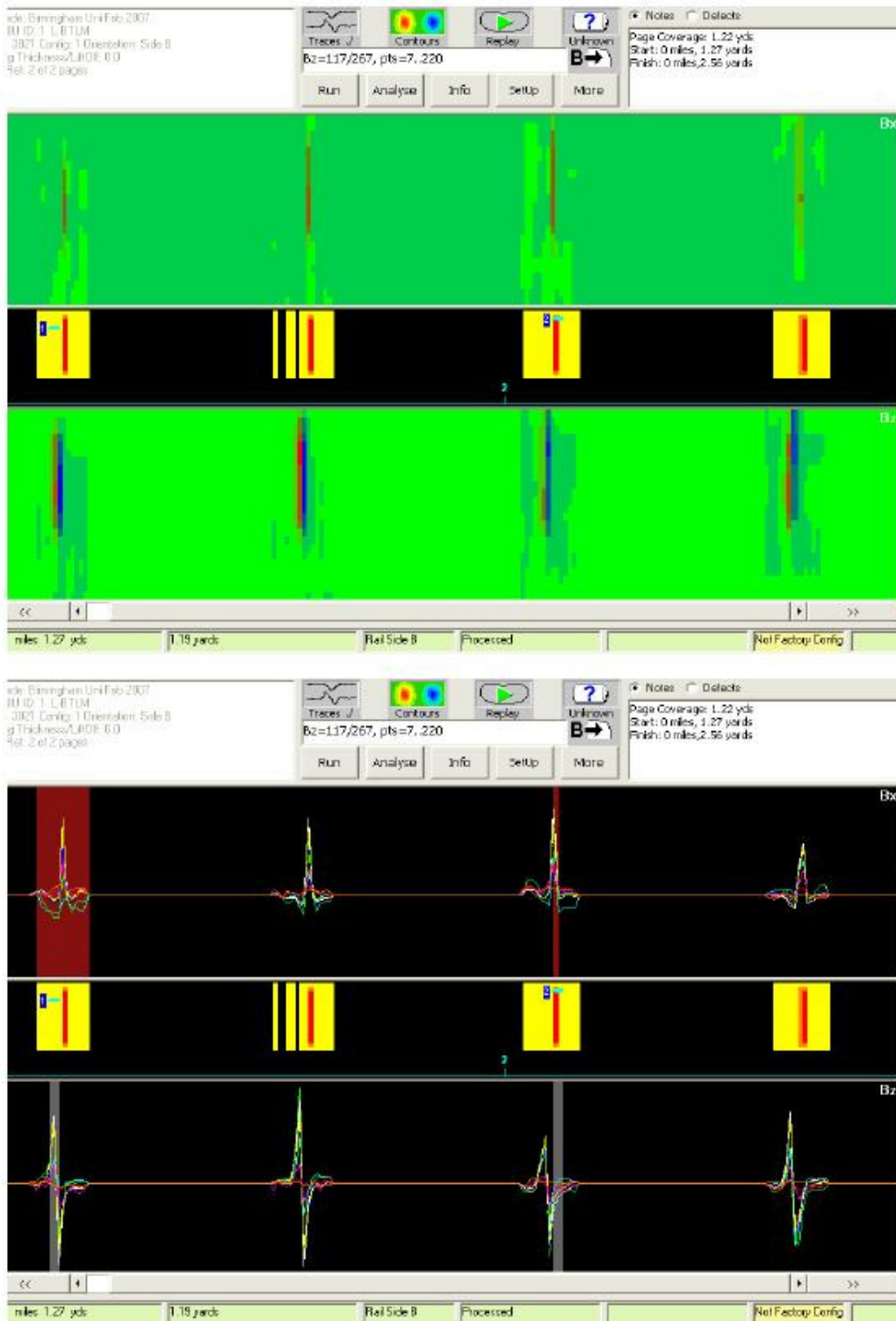


Figure 73 - ACFM C-scan for test rail 1

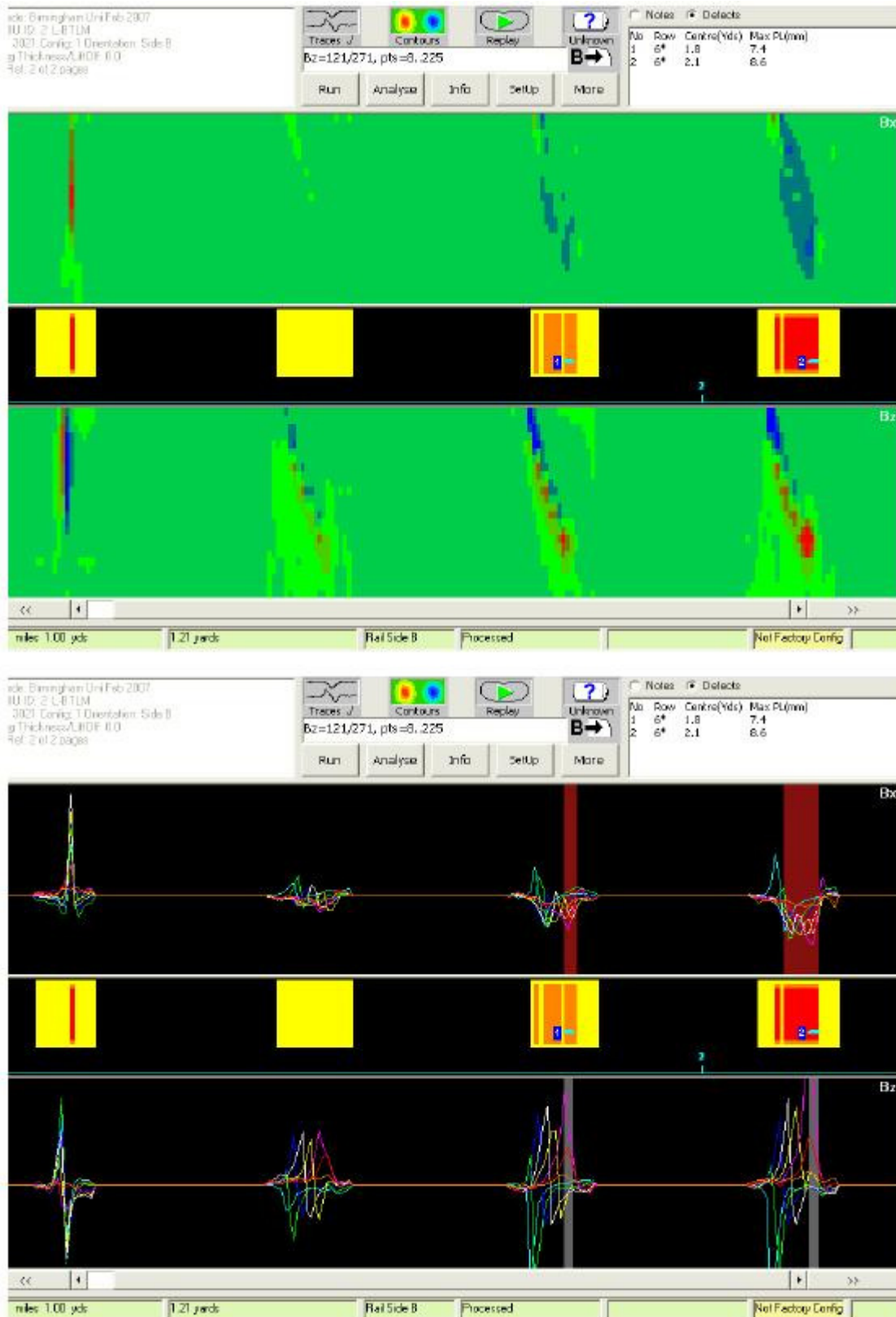


Figure 74 - ACFM C-scan for test rail 2

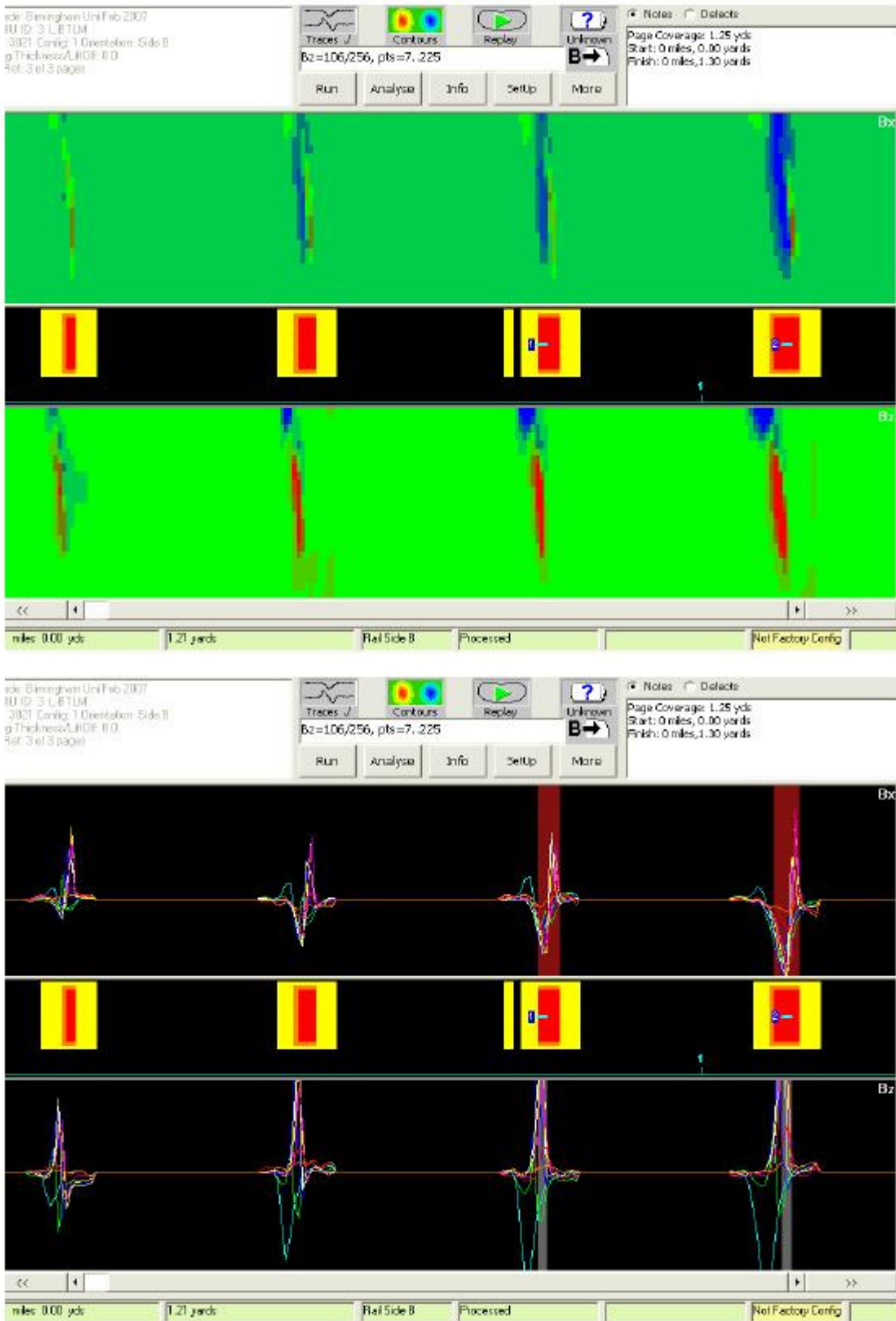


Figure 75 - ACFM C-scan for test rail 3

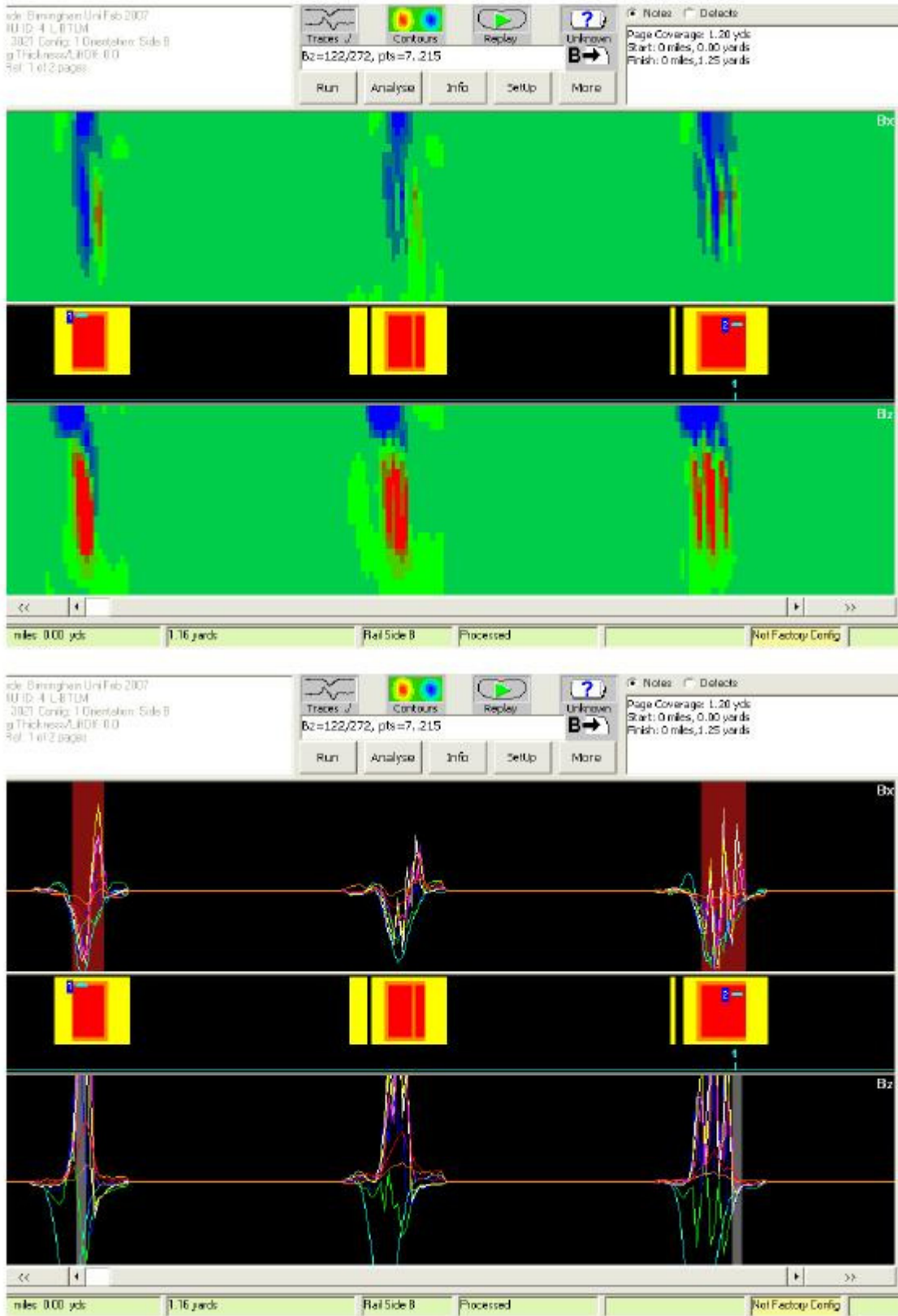


Figure 76 - ACFM C-scan for test rail 4

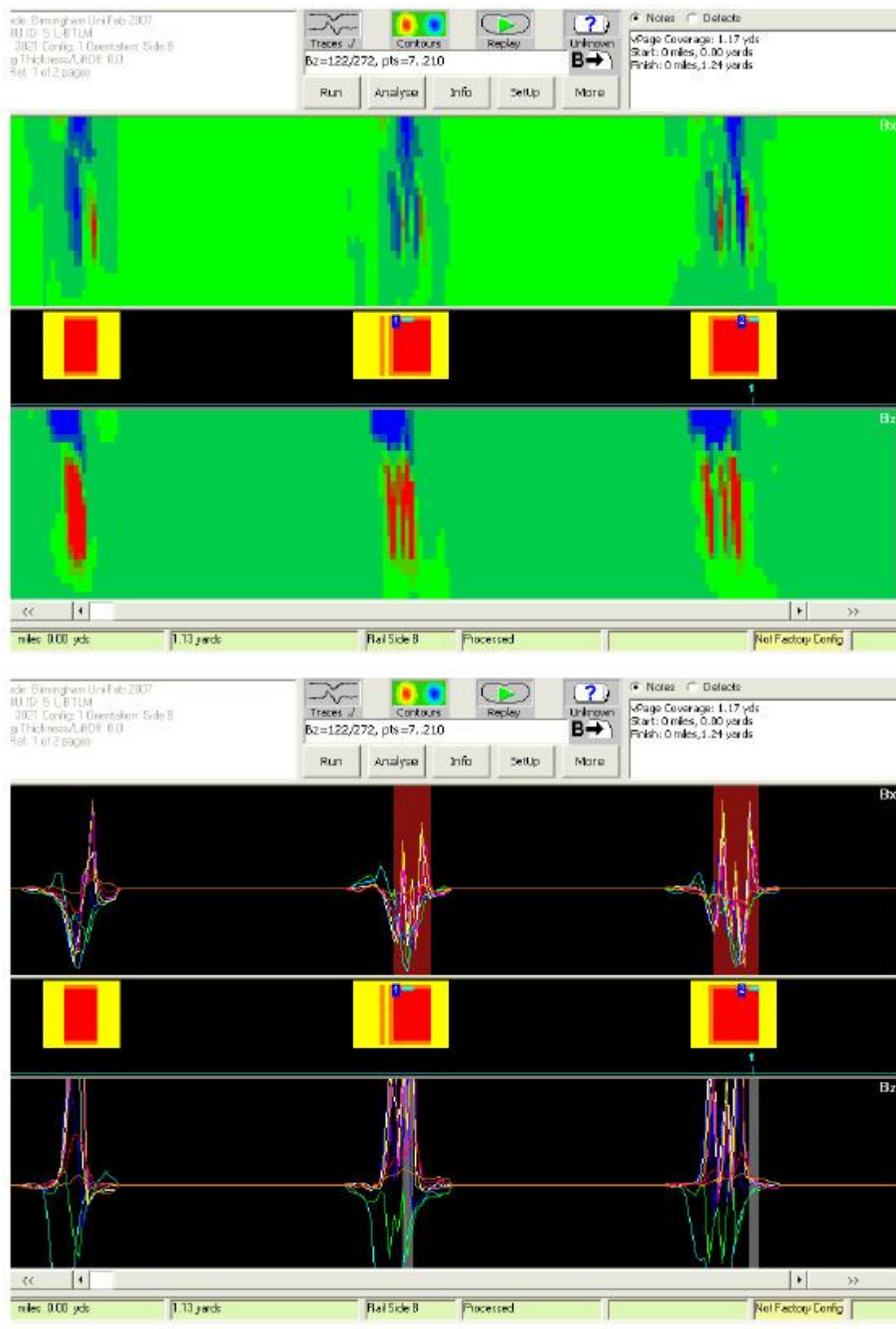


Figure 77 - ACFM C-scan for test rail 5

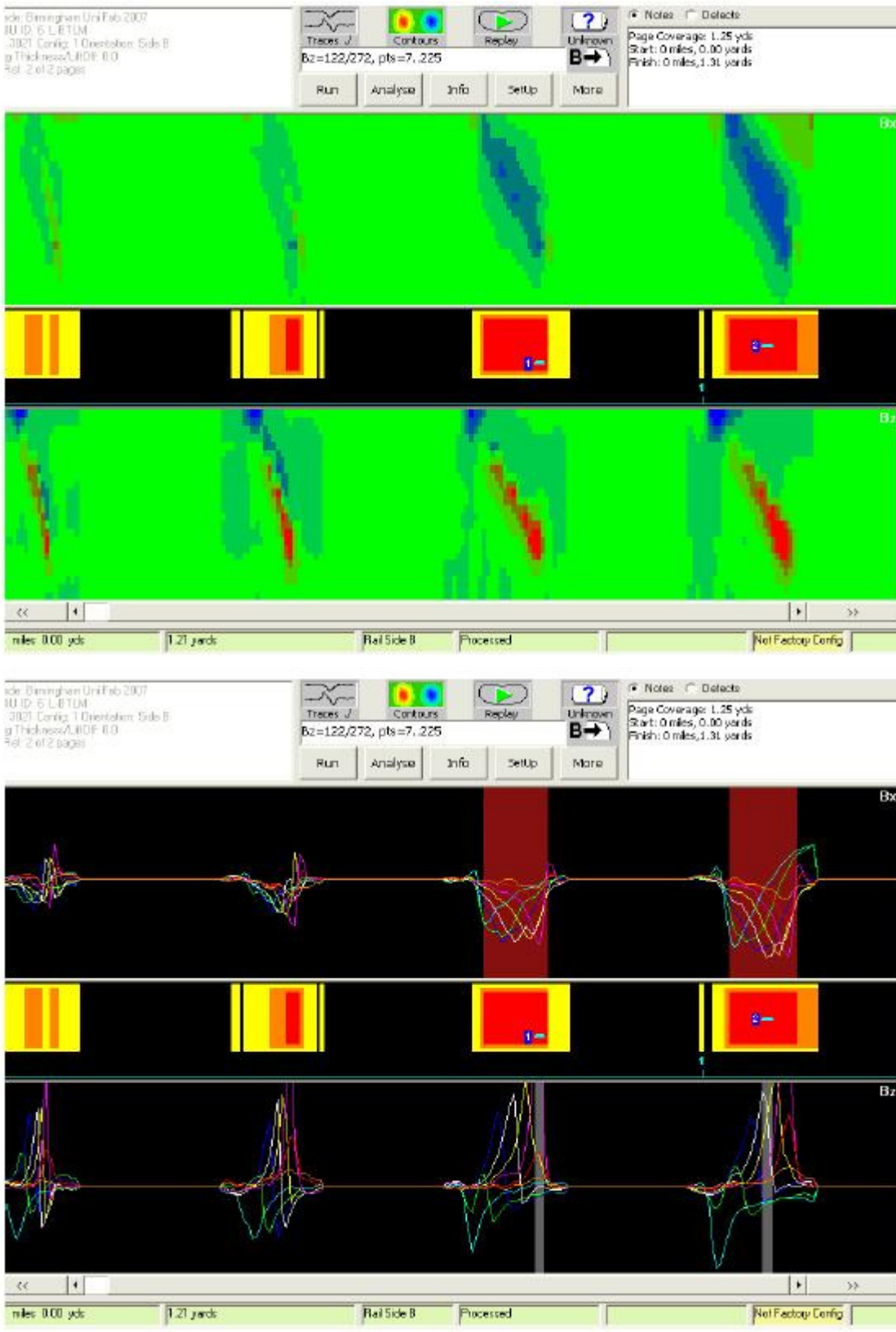


Figure 78 - ACFM C-scan for test rail 6

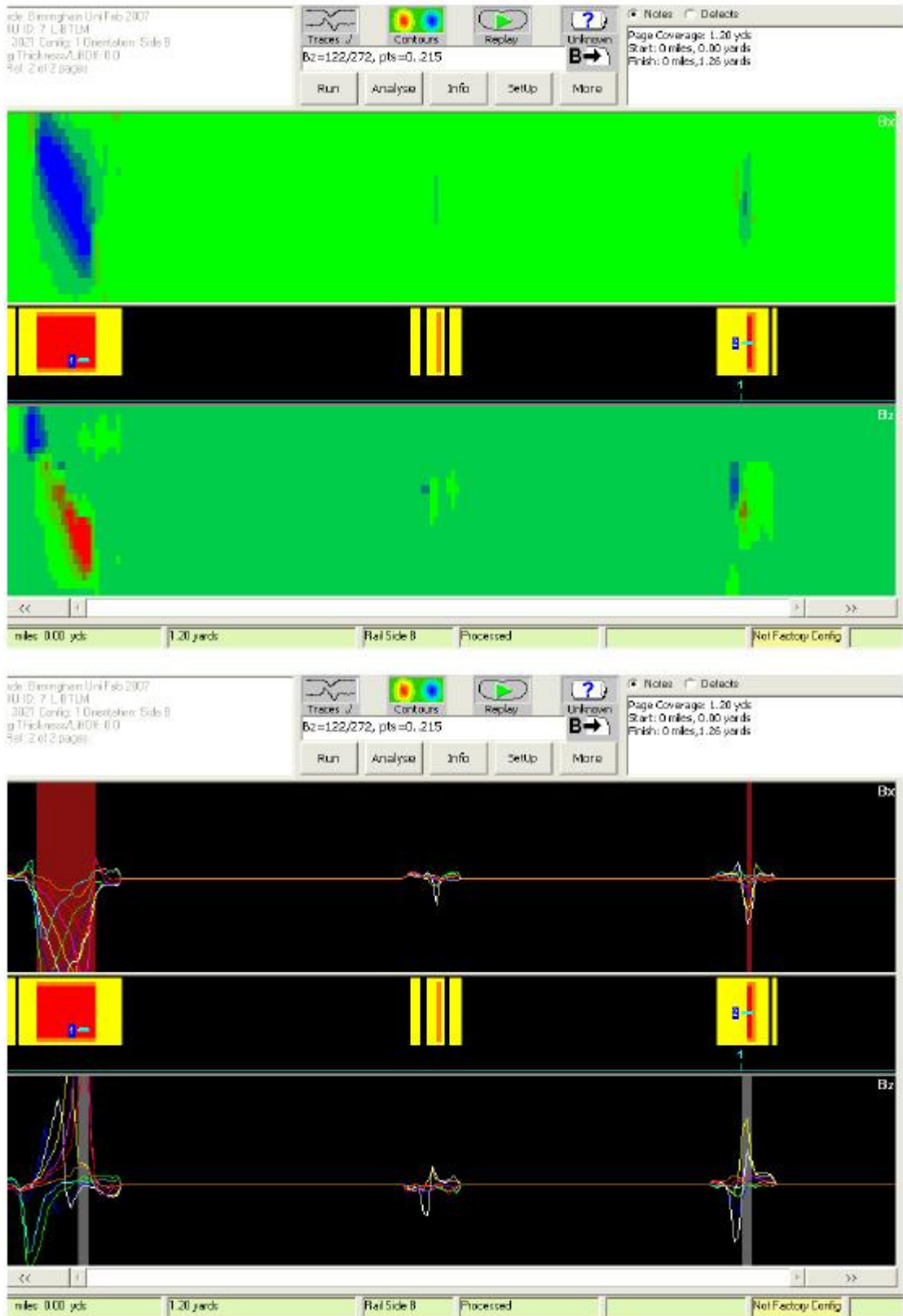


Figure 79 - ACFM C-scan for test rail 7

Figure 80 and Figure 81 shows the C-scan for 3 rail head pieces containing actual RCF cracking.

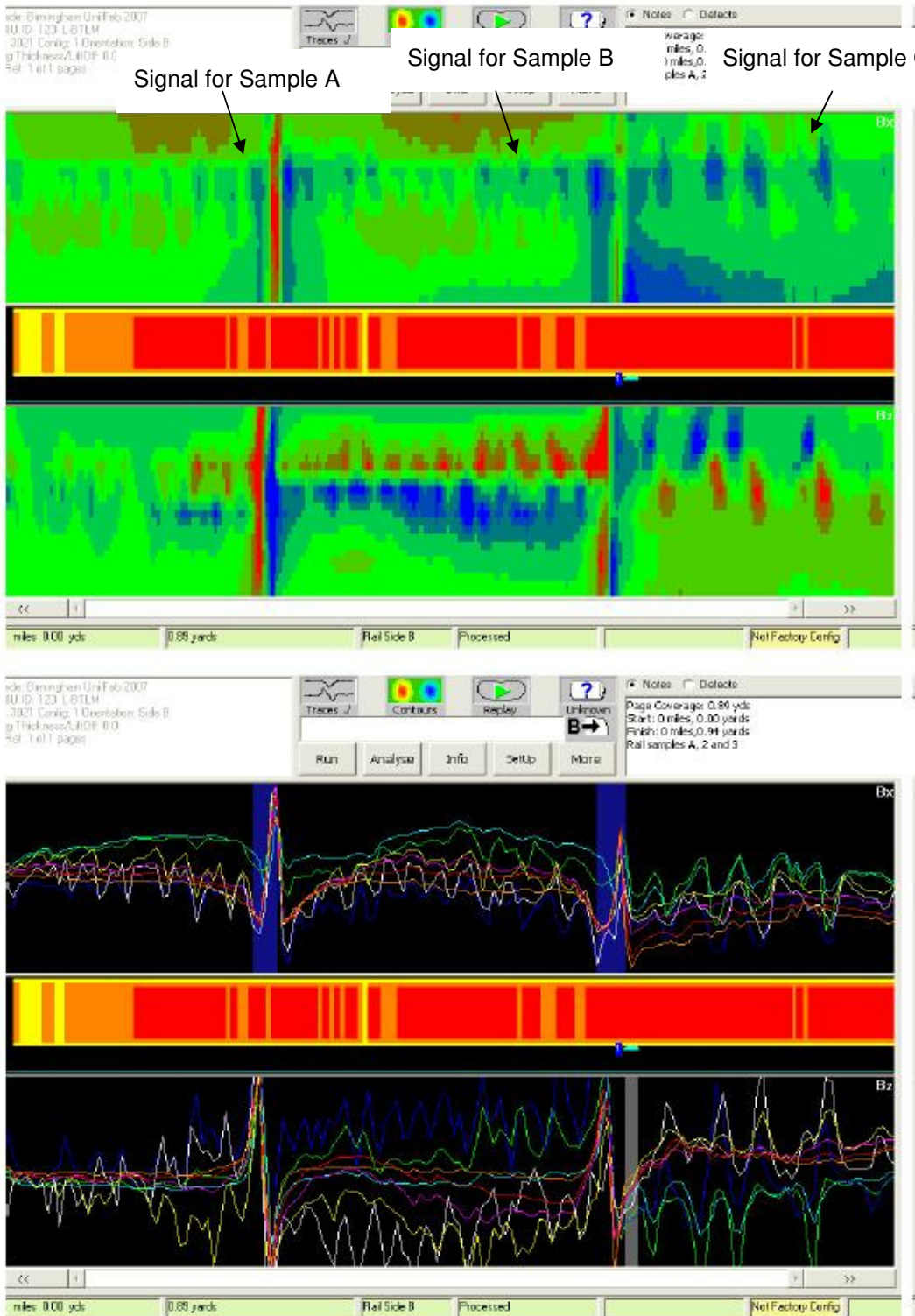


Figure 80 - C-scan for three railhead pieces containing actual RCF cracking

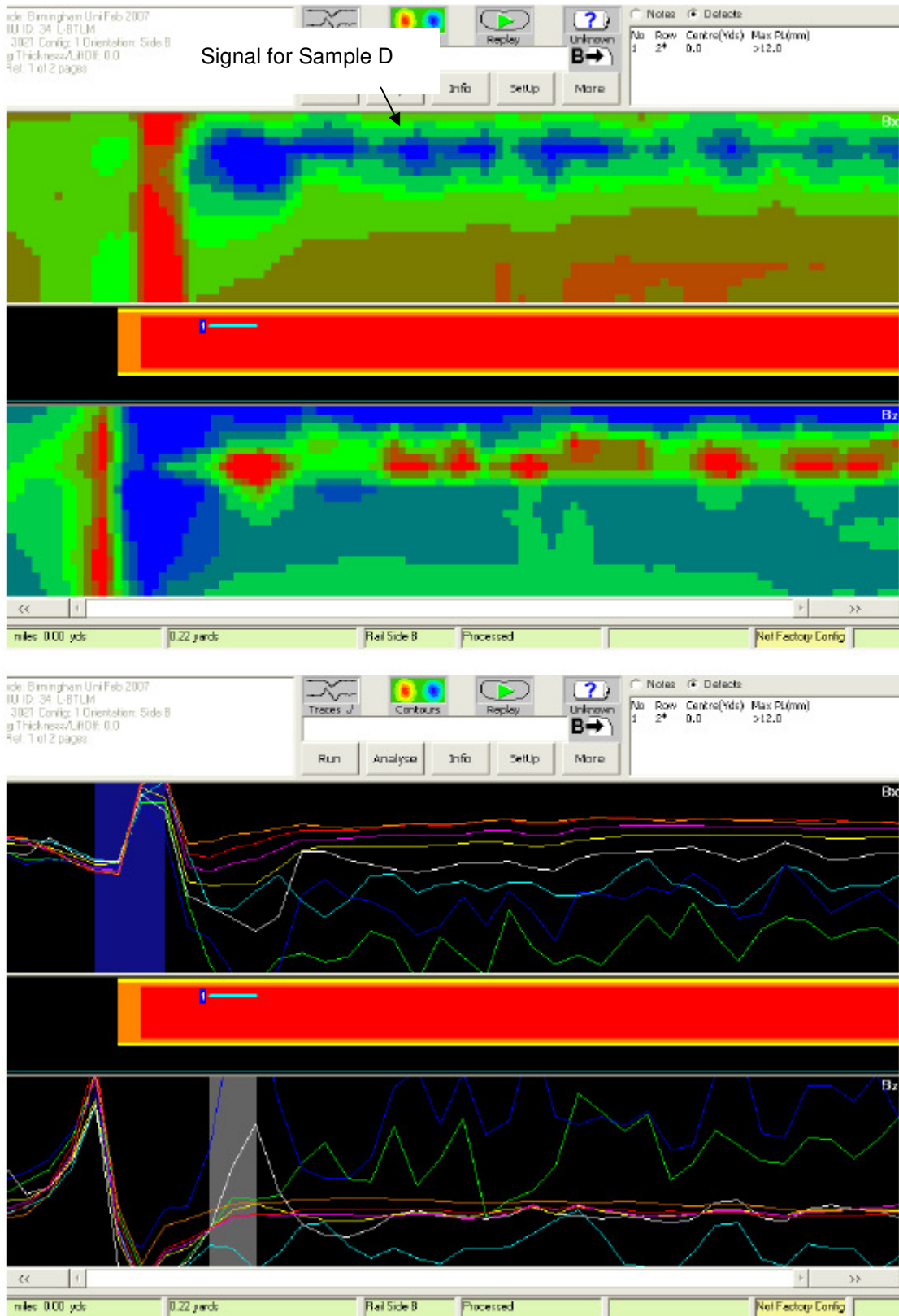


Figure 81 - C-scan for railhead piece containing actual RCF damage

The photographs in Figure 82 show the railhead samples that were inspected with the ACFM array.

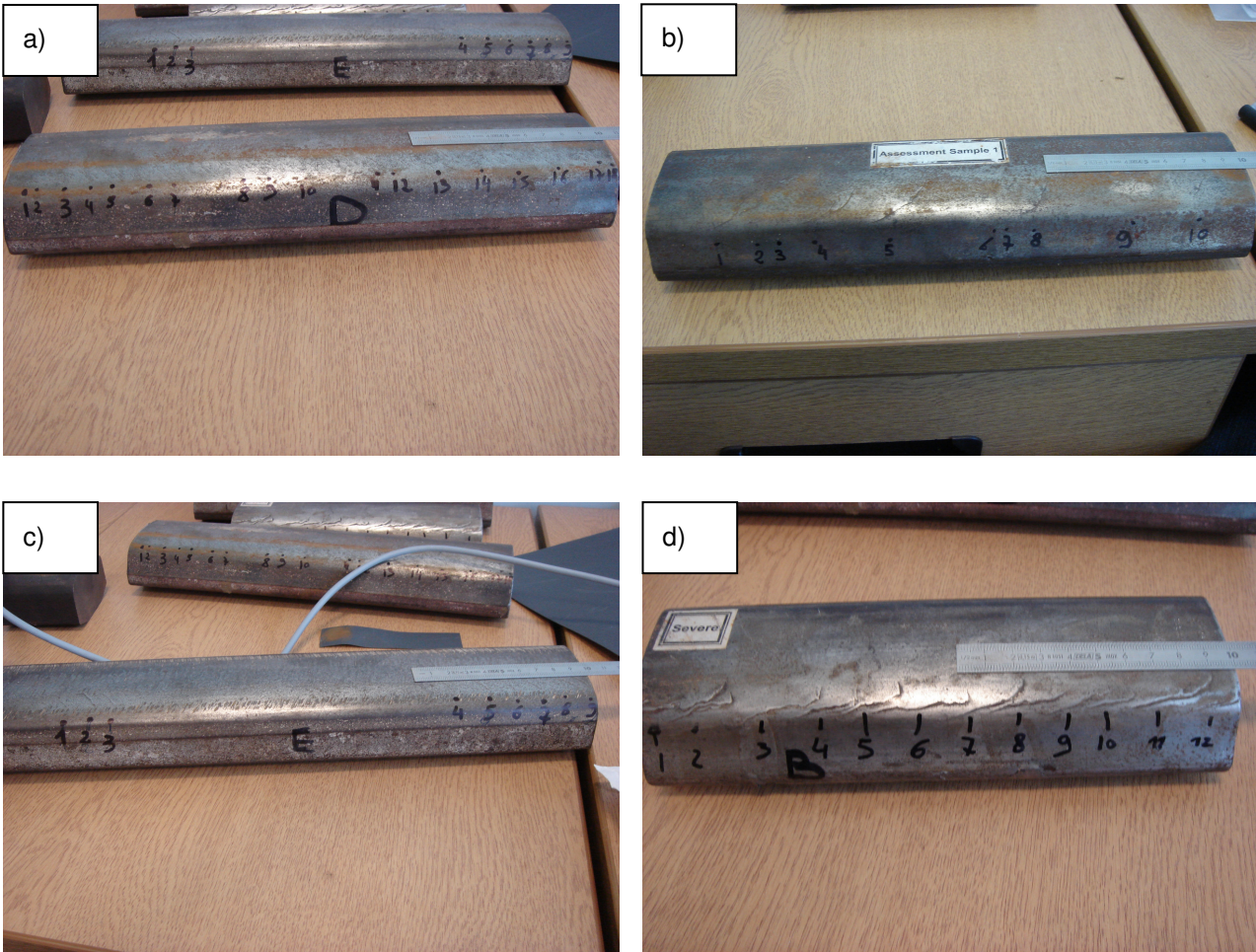


Figure 82 - Photographs of samples containing actual RCF cracking tested with the ACFM walking stick array

High-speed ACFM tests

High-speed tests were carried out using a single-channel ACFM pencil probe that was driven by a TSC AMIGO system. Initial tests were carried out on a rotary test piece made of a similar steel grade with the 260 rail steel grade. The rotary test piece contained four spark eroded notches in the middle of the rim as shown in Figure 83.

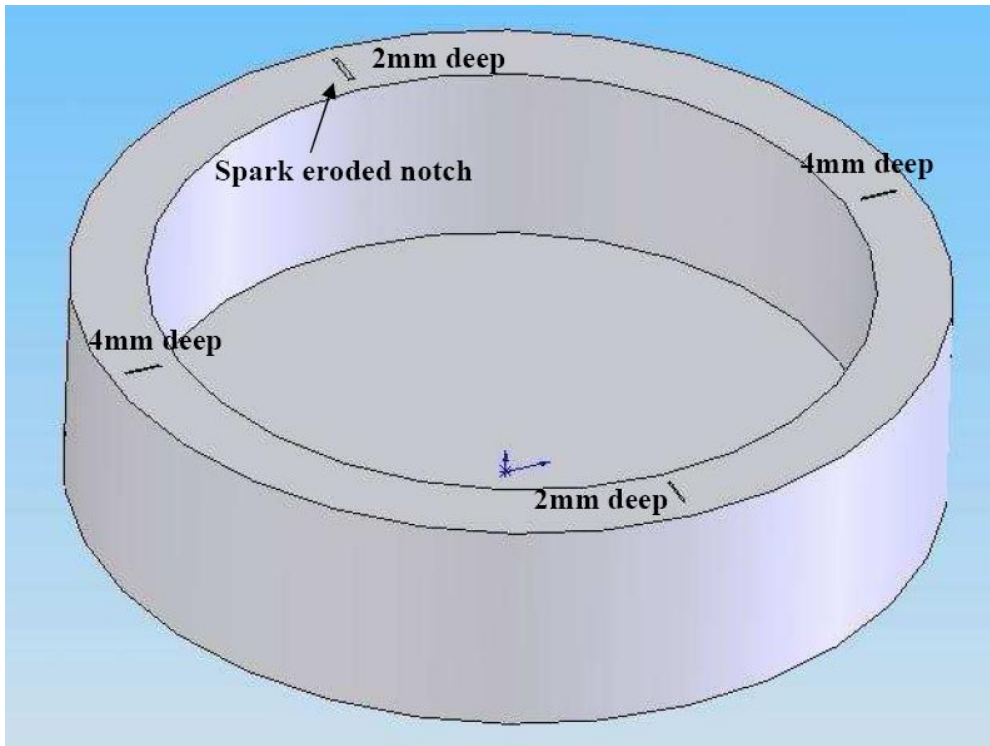


Figure 83 - Rotary test piece with spark eroded notches

The notches were 10mm long and 0.5mm wide. Their depth was 2mm and 4mm with a flat profile. The test piece was loaded on a turning lathe capable of rotating the rotary test piece up to 3000 rpm (121.5km/h surface speed at the centre of the notches) as shown in the photographs in Figure 84. The ACFM probe was placed at a distance of 0.8mm from the surface of the rim and tests were carried out for a range of speeds from 0.1km/h up to 121.5km/h.

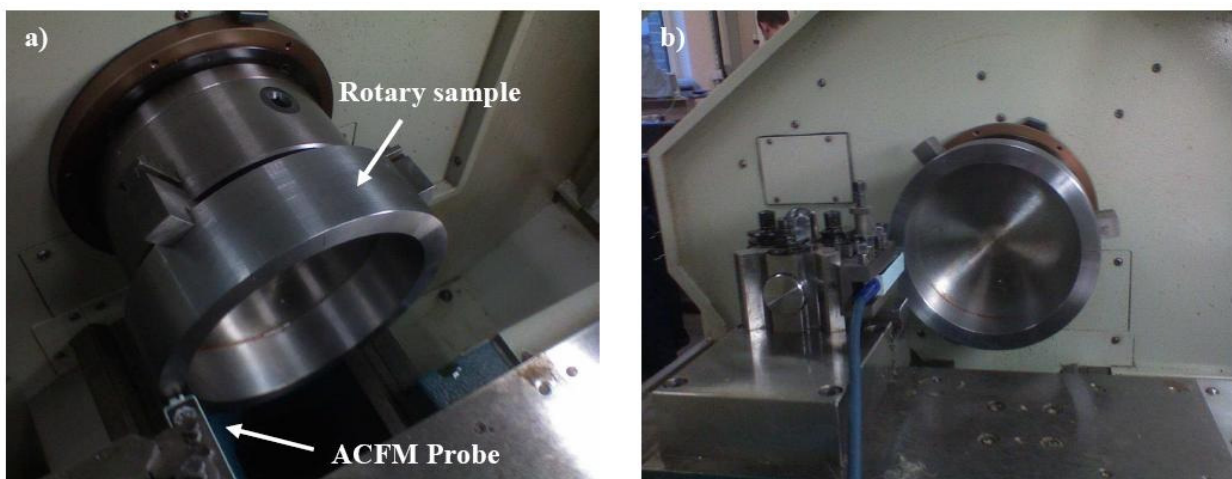


Figure 84 - Experimental configuration for the turning lathe tests

Figure 85 shows the data obtained at 20.25km/h and 121.5km/h for a probe lift-off of 0.8mm. The intensity of the signal is virtually identical as is the noise level of the measurements.

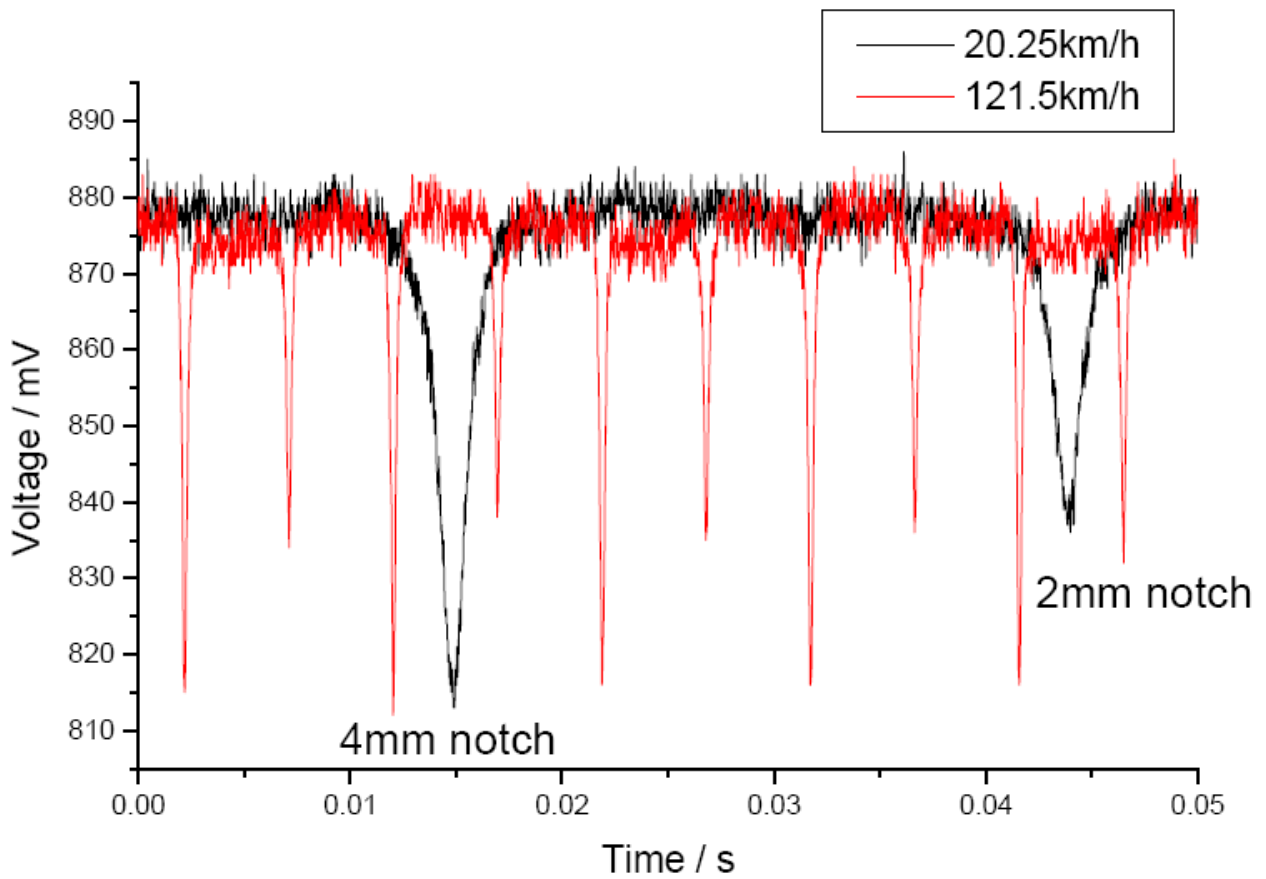


Figure 85 - ACFM data at 20.25km/h and 121.5km/h at a lift-off of 0.8mm

Figure 86 shows the lift-off effect in the ACFM signal as measurements were taken with progressively larger lift-offs. The data shown is at 81km/h. The signal decreases by the square of distance in comparison to eddy currents where the signal diminishes by the cube of the distance.

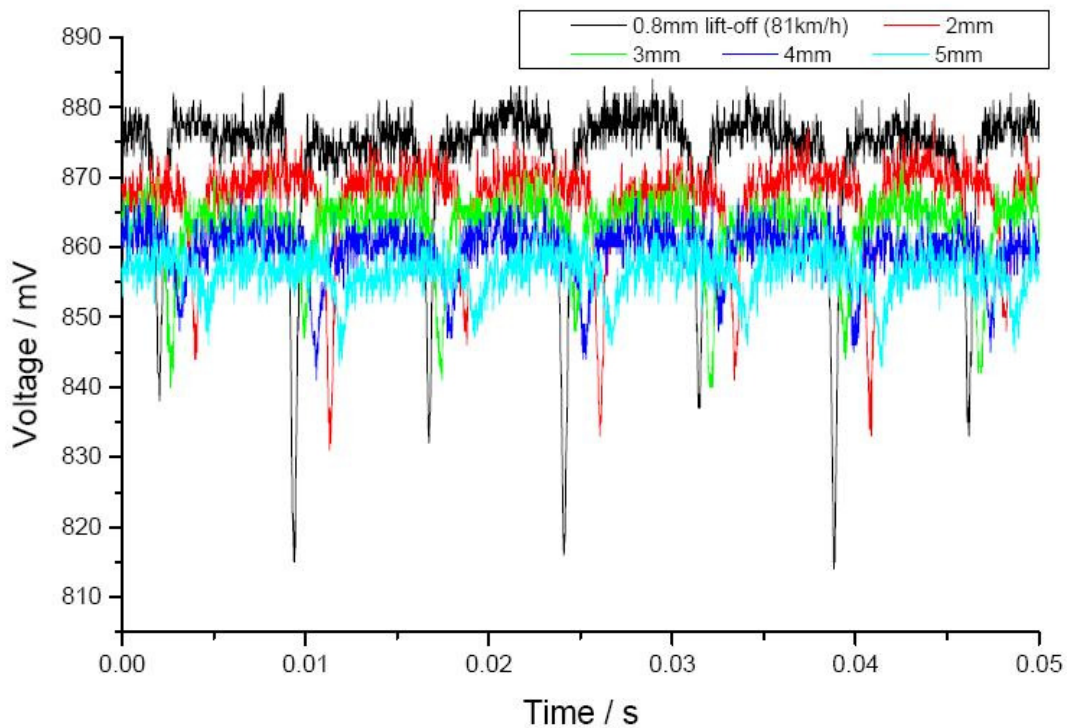


Figure 86 - ACFM signal with increasing lift-off at 81km/h

Figure 87 shows the normalised plots of the ACFM signals for varying lift-off.

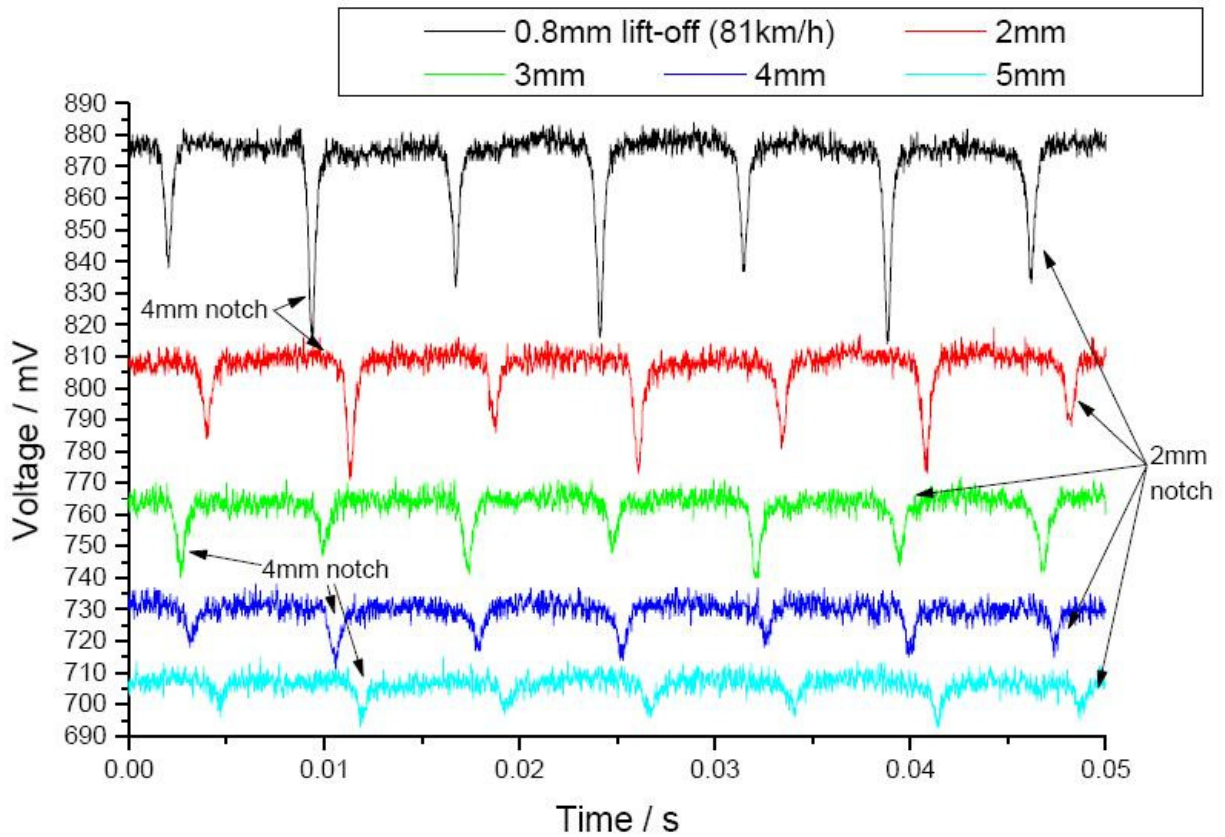


Figure 87 - Normalised ACFM plots showing the effect of increasing lift-off

Following the turning lathe experiments, tests were carried out on the spinning rail rig using the test rails containing spark eroded notches. The same micro pencil ACFM probe was used during the experiments. The photograph in Figure 88 and Figure 89 shows the experimental setup.

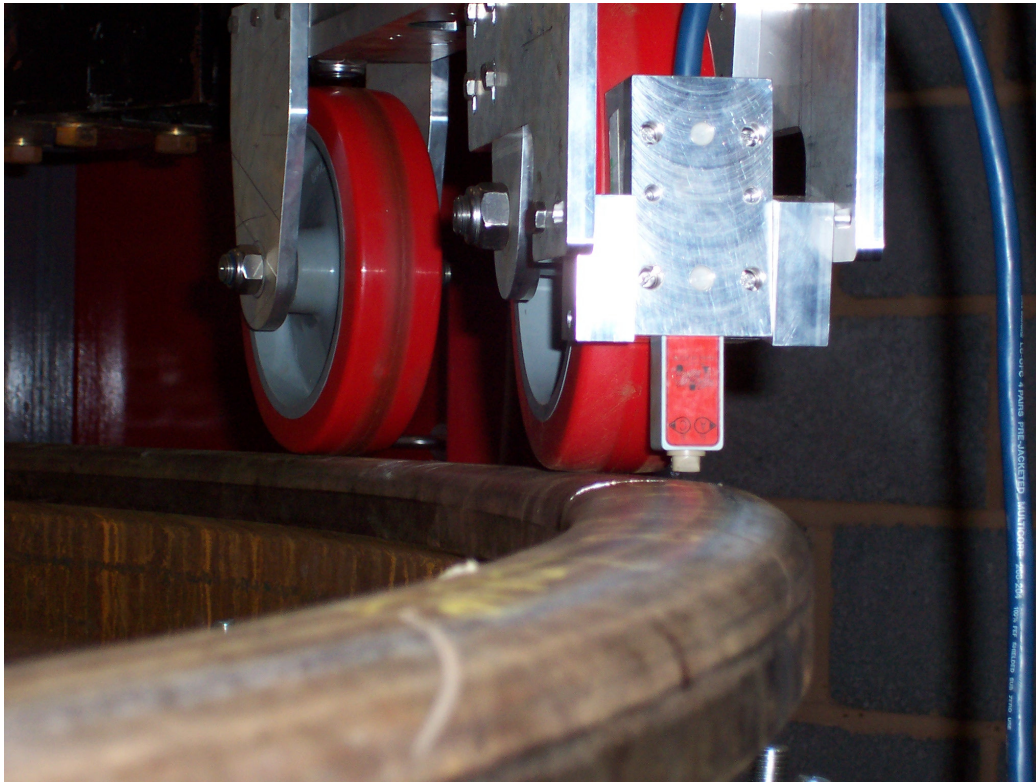


Figure 88 - Experimental setup for the spinning rail rig tests. The ACFM probe can be seen in the foreground

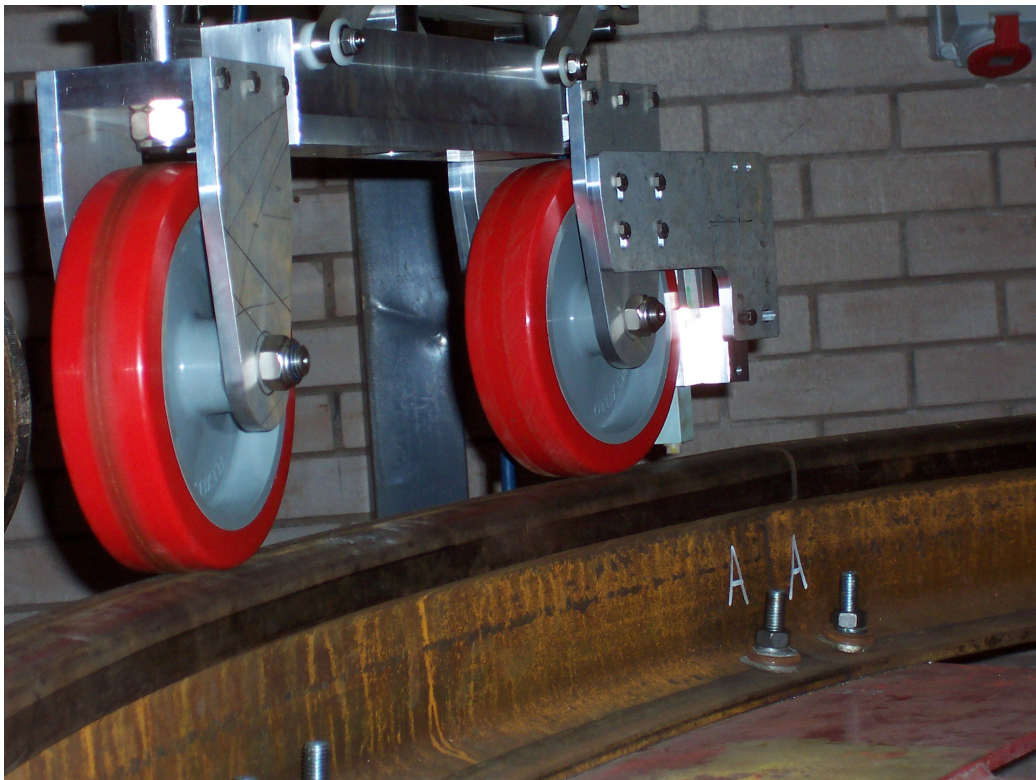


Figure 89 - An alternative view of the experimental setup for the spinning rail rig tests

Tests were carried out between speeds of 1km/h-32km/h. Although the tests revealed virtually no difference in the ACFM signal at different inspection speeds the lift-off variation exhibited during the tests affected the results. The lift-off variation for a full rotation of the rig is given in Figure 90.

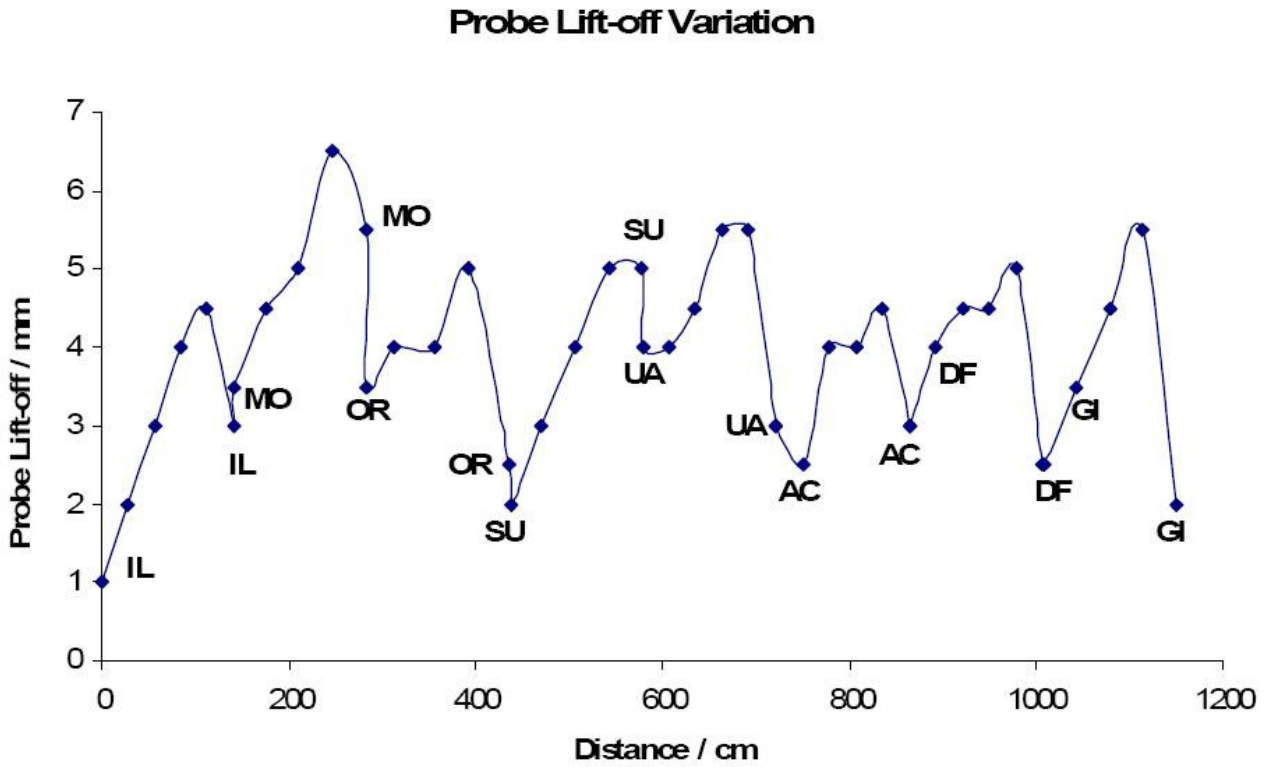


Figure 90 - Probe lift-off variation for the spinning rail rig tests

The plots in Figure 91 and Figure 92 show the similarity of the ACFM signal obtained at 2.3km/h and 32km/h. The effect of the lift-off variation in the measurement is also evident.

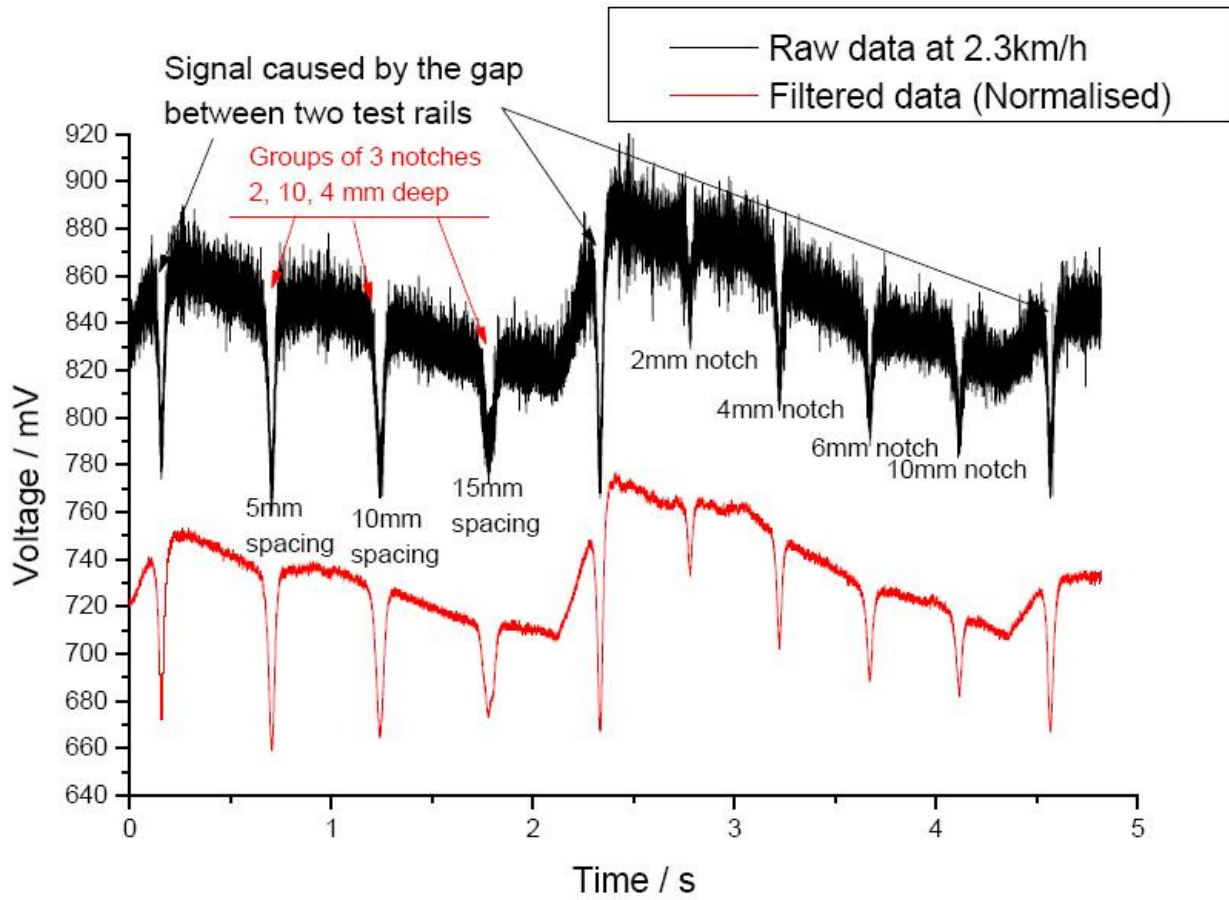


Figure 91 - Plot showing the ACFM signal for test rails #3 and #5

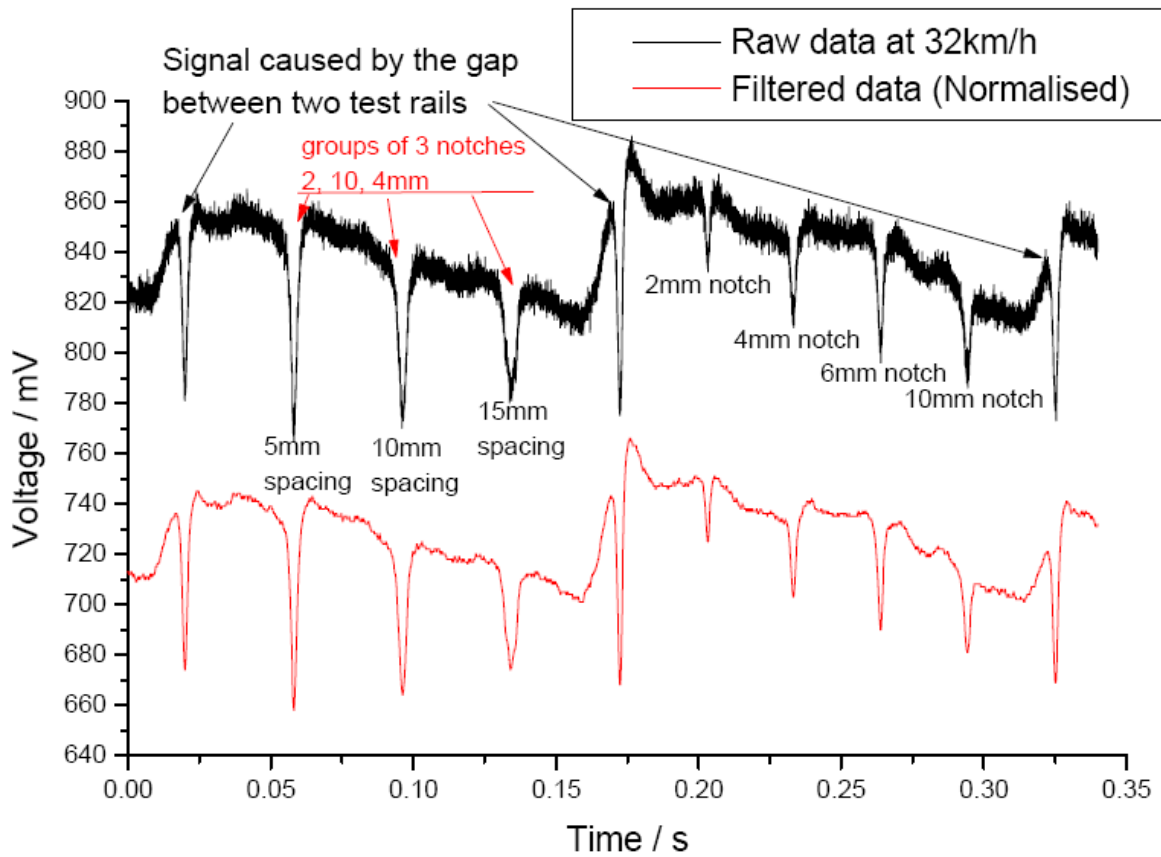


Figure 92 - Plot showing the ACFM signal for test rails #3 and #5

Figure 93 shows the ACFM data plot for rail #8.

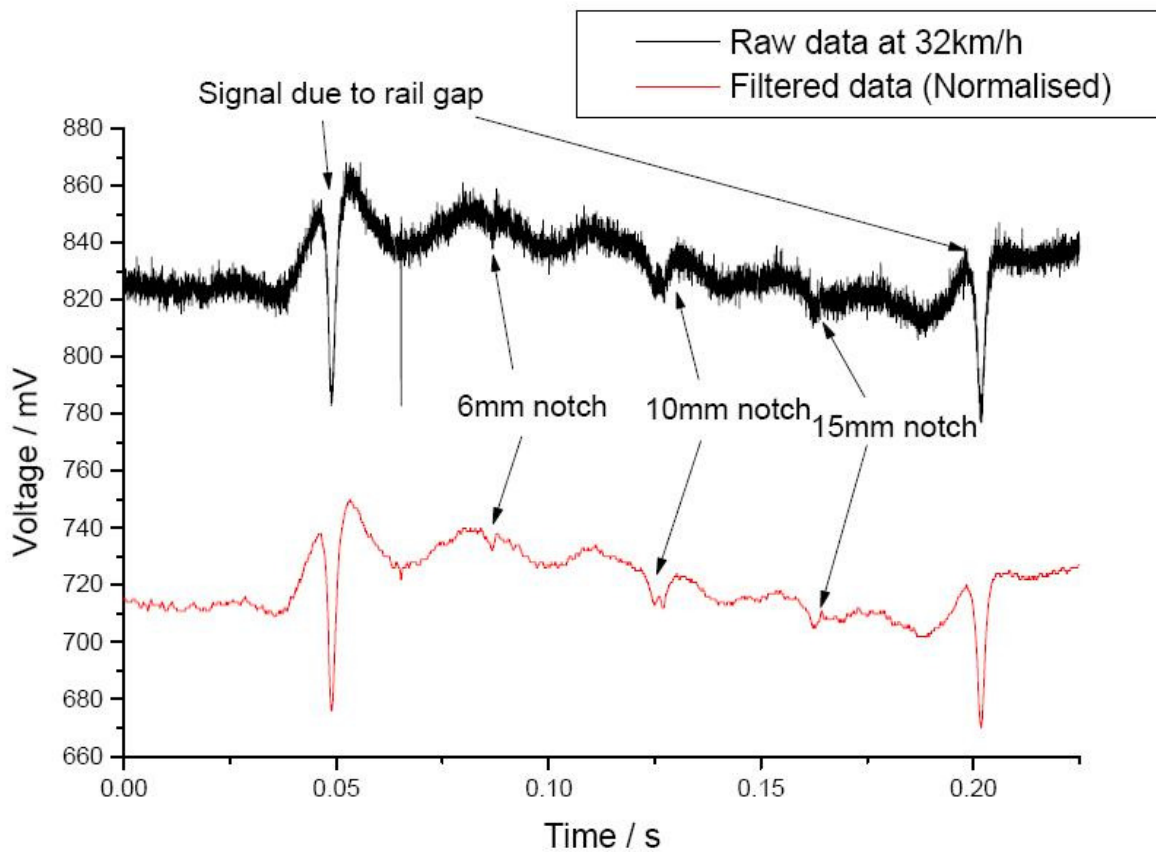


Figure 93 - Plot showing the ACFM signal for test rail #8

Summary for ACFM tests (UNIBHAM)

High-speed ACFM tests were carried out using a micro pencil ACFM probe that was driven by a TSC Amigo crack microgauge system. Tests were carried out initially using a rotary test piece containing spark eroded notches 2mm and 4mm deep. A turning lathe was used to rotate the rotary test piece at speeds up to 121.5km/h (at 3000rpm). This experimental configuration provided controlled inspection conditions as well as easy repeatability of the tests. It was found that the probe could successfully detect the induced notches at 121.5km/h and that the ACFM signal remained largely unaffected by the increases in the speed under constant lift-off. Tests using different lift-offs revealed that the intensity of the signal obtained for a given notch was reduced by the square as the lift-off increased as predicted by the theory.

In order to simulate actual rail inspection conditions at high speed, further tests were carried out using the spinning rail rig at the University of Birmingham. The ACFM micro pencil probe was installed on a special trolley, however under this experimental configuration it was impossible to compensate for lift-off variations that occurred during the spinning rail rig tests due to limitations in the design of the trolley used. Data analysis of the results obtained showed that the ACFM sensor detected the vast majority of the induced notches, missing only the smaller pocket-shaped defects in rail #7. It was also found that the variations in the lift-off made it impossible to obtain the correct rankings for all detected defects. Comparison of the ACFM data at various inspection speeds showed that the signal remained largely unaffected with increasing velocity up to 32km/h. Unfortunately, lift-off variations during the experiments did not permit a more accurate evaluation of the capability of the ACFM micro pencil probe. However the implication that arise from the fact that there is virtually no loss of signal with increasing speed is extremely important for the application of ACFM technology as an alternative means of high-speed inspection of rails. The performance of the ACFM technique at inspection speeds up to 80km/h and constant lift-off is currently under investigation using a new trolley design.

Head checking characterisation by EMAT inspection (Warwick and UNIBHAM)

Electromagnetic acoustic transducers (EMATs) are increasing in usage as the technology improves [8-14]. An EMAT is a non-contact ultrasonic transducer which couples electromagnetically with an electrically conducting and/or magnetic sample, allowing stand-offs of up to several millimetres above the sample surface; more details of their operation are available in references [9-11]. Their efficiency is significantly less than standard ultrasonic techniques; however the benefits of being non-contact and generating a broadband pulse can sometimes outweigh the lower efficiency [10,11]. The lack of need for couplant and contact with the railhead lifts some of the speed constraints, and a different measurement configuration can remove the need to wait for a reflected wave. The schematic in Figure 94 shows the experimental setup for the EMAT tests.

Surface ultrasonic waves with properties very close to those of Rayleigh waves are used to characterise surface defects [12,13]. Waves are generated at one point on the rail using an EMAT and then the transducer is free to move. The waves travel along the railhead and are detected by a second EMAT a fixed short distance later (currently 150 mm). The waves travel much faster than current train speeds and arrive at the detection EMAT even if the train is moving. With a fixed separation and known train speed the arrival time is known and the transmitted Rayleigh-like wave can be windowed and analysed to gain information about the cracking [13,16,17]. The coil design can be optimised for application; in these measurements we mainly use a meander-coil design of generator, specifically used to generate a large signal amplitude Rayleigh wave, and detect using a linear receive coil [9,13].

The energy of a Rayleigh wave lies predominantly within one wavelength below the surface, and a surface-breaking defect will act like a filter to such a wave; those waves with a longer wavelength than the crack depth will be able to partially pass underneath the crack, whilst those with a shorter wavelength will be mainly blocked [16,17]. The EMATs used here generate a broadband signal; by looking at changes in both the amplitude of the signal and its frequency content after it has been transmitted through a cracked region the depth of the crack can be measured, and this is presented in references [13,17]. Due to the filtering action, over a region of clustered cracking the deepest crack will have the dominant effect and hence the depth of the most serious defect will be recorded [13]. The system can size cracks from a vertical depth of approximately 1.5 mm to 20 mm, with deeper cracks indicated by a complete blocking of the signal [17]. For a real rail measurement system the lift-off will not remain constant, and variations in lift-off lead to changes in the signal amplitude unrelated to the presence of defects [14]. However, the overall frequency content of the generated pulse remains almost constant, and with normalisation a measurement of transmitted frequency content will give a reliable depth measurement even with variations in lift-off [14,17].

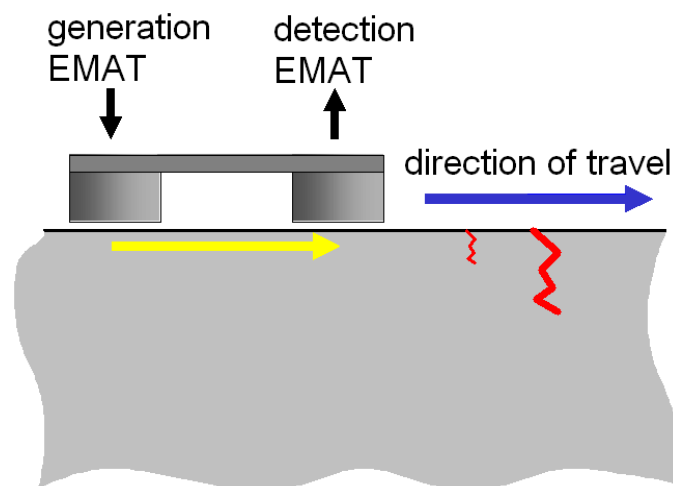


Figure 94 - Schematic showing the EMAT experimental setup

Crack characterisation at speeds of around 100 mph and higher should be possible using this technique with some improvements to the EMATs and pulse generator. A significant restriction on speed of testing is the

speed of data acquisition and analysis, and a system has been developed using a hardware rather than software approach to analysis, based on Field Programmable gate Arrays (FPGAs) [18]. This system allows the data to be taken, processed, and a fast Fourier transform (FFT) applied to measure the frequency content, all in about 400 μ s, with post processing to detect a faulty rail taking a further 600 μ s.

The EMAT probe was used to test the eight curved rail sections with simulated defects. The probe was placed in a trolley to allow the lift-off to remain close to 1.5 mm and to ease the scanning. Measurements were at an average speed of around 0.2 m/s with some variation during the scan. A slow pulse generator and software-based data acquisition system were used to record the data, with an approximate repetition rate for data acquisition and analysis of around 5 Hz. Signals were recorded as single shot with no data averaging, with filtering to reduce the noise level [13].

Figure 95 shows results recorded on Rail 1, which contains four defects normal to the rail edge and top surface machined part way across the rail. This is not realistic compared to actual rail defects; however, it is the simplest simulated defect and is included to improve understanding of the transmitted ultrasonic signals. The defects range in depth from 2 to 10 mm. Figure 95b shows the reduction in signal amplitude when a crack is present (grey line) compared to when the surface is defect free (black line). A fairly low signal-to-noise ratio due to the lack of averaging is observed, but improved filtering will improve signal quality; the drop in signal due to the presence of a defect remains obvious.

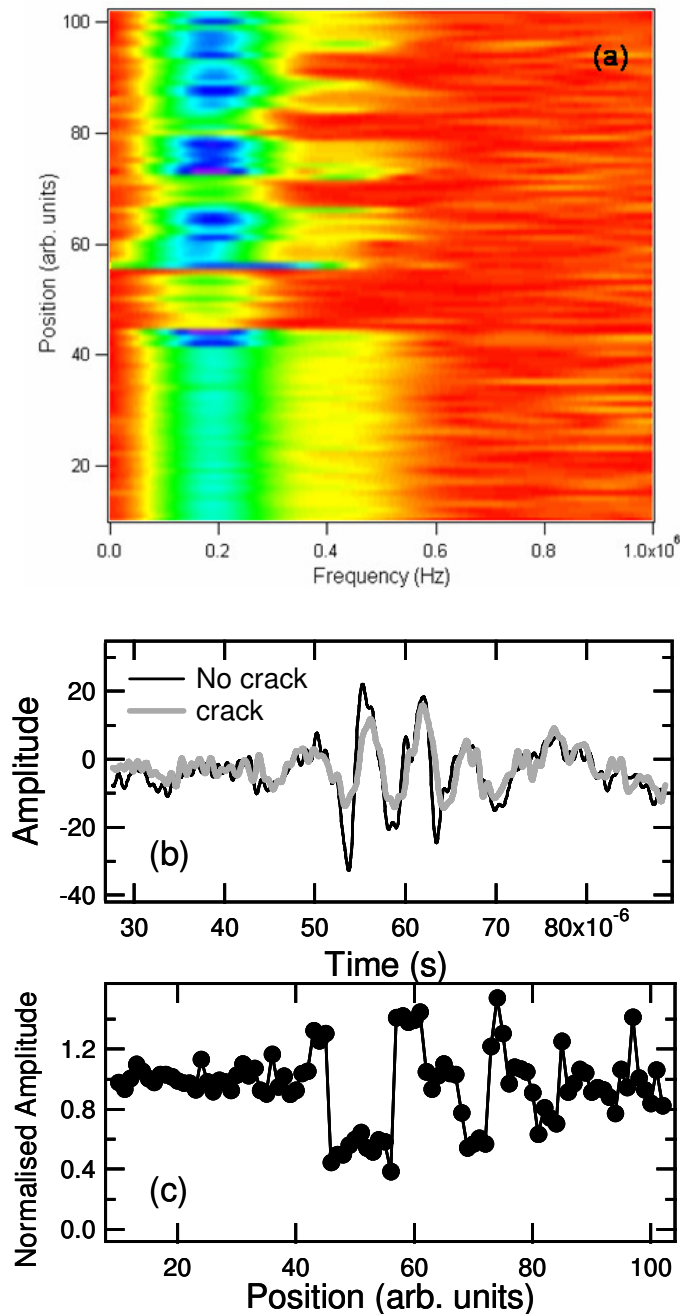


Figure 95 - EMATs: transmitted ultrasound on Rail 1. (a) Frequency B-scan, (b) two A-scans, (c) the change in normalised Rayleigh-wave amplitude during the scan

The peak to peak amplitude of the Rayleigh-like wave is recorded, and after normalisation by the defect-free measurement Figure 96c is obtained showing normalised amplitude against data-point-number (the trolley is above each crack for a different number of data acquisitions). Three of the cracks are obvious (10, 6 and 4 mm deep, with the 10 mm slot measured around position 45) with identification of the signal reduction due to the 2 mm deep slot difficult due to the noise level. Work is ongoing into the possibility of logically combining the measurement with a drop in the FFT magnitude at 400 kHz for almost all cracks measured to give weight to a measurement close to the noise level. Initial results using this method allow us to detect approximately 38 of the 40 machined defects with a high certainty [18]. Figure 96a shows a type of B-scan generated using the FFTs of the Rayleigh-like wave at each acquisition, with frequency on the x-axis, position on the y-axis,

and the magnitude shown by the brightness, varying from red (zero magnitude) to blue (maximum). Four regions where higher frequencies are blocked are obvious, indicating four defects.

Figure 96 shows similar results on Rail 4, which contains clusters of defects. These simulate regions of clustering where standard ultrasonic techniques may underestimate the depth of the deepest defect due to the shadowing effect of nearby shallow defects. The normalised amplitude (Figure 96b) shows three regions where the signal is partially blocked, indicating three regions of cracking; these all have a very similar drop in amplitude, as in each region the deepest defect dominates. Sharp increases in amplitude are seen when the detection EMAT is very close to a crack and the direct and reflected Rayleigh waves and mode converted waves interfere [15]. Whilst highly indicative of a crack, this measurement is dependent on a slow-scan and cannot be relied upon. The B-Scan produced by the frequency content is shown in (a), and again, three very similar regions are identified.

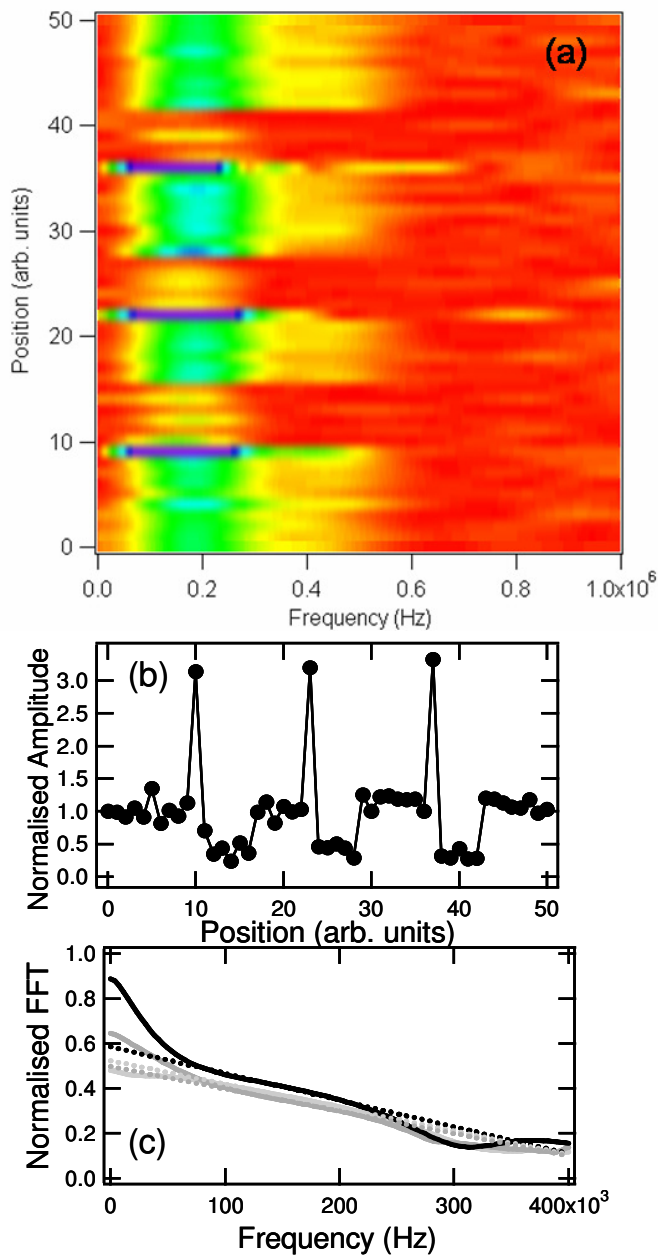


Figure 96 - Rail 4 (clustered defects). (a) Shows a frequency B-Scan, (b) shows the normalised signal amplitude, and (c) shows normalised FFTs in the cracked regions

In order to quantitatively analyse the frequency content the method described in reference [13] is used. As in the amplitude normalisation, an FFT from a region of clear rail is used as a reference and all later signals are divided by this reference. In the region of significant frequency content (approximately 50 to 350 kHz for these EMATs) a non-defect region will show as a straight line with magnitude 1. A normalised FFT over a defect will show as an approximately straight line in this region with a slope towards the frequency axis, indicating the increasing blocking of the signal with increasing frequency [17]. Figure 77c shows normalised FFTs taken from signals transmitted underneath each of the three clusters. A cut-off frequency is defined as the frequency at which a straight line fit crosses the frequency axis [17]; as can be seen, the cut-offs are all very similar, indicating again that the deepest defect dominates.

Similar analysis has been done on rail 6, containing cracks at an angle to the rail edge and surface, with results shown in Figure 97. Again, Figure 97b indicates three definite cracks, with a fourth possible around a position of 18 and confirmed using frequency analysis. Figure 97a shows a B-scan made up of normalised FFTs, with black showing zero magnitude and white maximum, clearly indicating the presence of four cracks. Cut-off frequencies scale as approximately 1.26 MHz, 670 kHz, 480 kHz, and 300 kHz for the 2, 4, 6 and 10 mm vertical depth cracks respectively, as expected (cut-offs higher than the content of the generated pulse are possible due to the data analysis technique, which extrapolates the results in the region of frequency content to higher frequencies [17]).

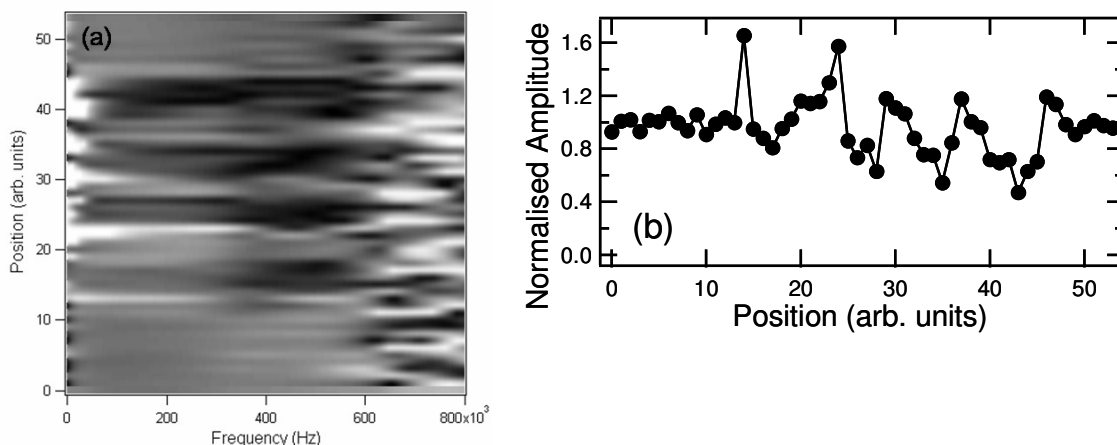


Figure 97 - Rail 6 (two angles). (a) Frequency B-Scan made up of normalised FFTs; (b) normalised signal amplitude

A new trolley has been developed to hold the EMATs above the rotating rail rig for higher speed measurements, and the fast data acquisition system and a 100 Hz repetition rate pulse generator will be used. Due to the increased generation rate and the use of the fast data acquisition system, a similar level of detail to the above measurements will be possible at a speed of around 3.9 m/s. With an improved pulse generator and EMATs so that working at the highest possible rate of data acquisition is possible we will be able to gain this level of information at a speed of 39 m/s (87 mph). Further increases in speed are possible; the level of detail recorded in these measurements is excessive for high speed measurements, as the depth of each crack is measured around six times, and increasing the separation between the EMATs will reduce spatial resolution but allow higher speeds of testing.

Summary for EMAT tests (Warwick and Bham)

The EMAT non-contact technique will work at high speeds and give the depth of the deepest defect between the two transducers at any point, but lacks spatial resolution for identifying the exact position and number present between the transducers. A high-speed EMAT could identify areas which require further investigation, with a combined EMAT-phased array probe employed for slow testing to give extremely good imaging whilst ensuring that the deepest crack is detected.

The results presented here show the applicability of the EMAT sensors for rail testing. At hand-scanning speeds with a slow pulse generator and data analysis system, the EMAT measurements are able to detect

most of the simulated defects. Using higher frequencies would allow shallower defects to be detected, but would also detect small pitting. The phased array technique has shown promise for visualisation of cracks in the D-scan view. Improvements to EMAT techniques, including substitution of some of the magnets for reduced magnetic drag, are ongoing [14] with online analysis of the results being improved. A trolley has been produced for use with the rotating rail rig at Birmingham and experiments will be conducted shortly.

3.1.4 Comparison of results for common test rails

The tables below summarise the results obtained during experiments using the innovative techniques on the manufactured defects where comparison to absolute dimensions can be made.

Sample Number	Phased Array	Eddy Current	ACFM	EMATs
Rail 1 2, 4, 6, 10 mm defects	N/A	Correctly ranked by size, algorithms required to accurately size	Correctly ranked by size (also tested at speed)	Correctly ranked by size, algorithms required to accurately size
Rail 3 2, 4, 6, 10 mm inclined at 25 degrees	10 mm defect sized as 7-11 mm 6 mm defect sized as 5-7 mm 4 mm defect sized as 4-5 mm 2 mm defect sized as 2-3 mm	Correctly ranked by size, algorithms required to accurately size	Correctly ranked by size (also tested at speed)	Correctly ranked by size, algorithms required to accurately size
Rail 6 2, 4, 6, 10 mm defects inclined at 25 degrees and skewed at 35 degrees	10 mm defect sized as 7-9 mm 6 mm defect sized as 5.5-7 mm 4 mm defect sized as 4-5.5 mm 2 mm defect sized as 2-3.5 mm	N/A	Correctly ranked by size (also tested at speed)	Correctly ranked by size, algorithms required to accurately size

Table 8 – Normalised results of innovative techniques

Feature	Phased Array	Eddy Current	ACFM	EMATs
Can overcome crack shadowing	Characterisation in depth of Squat: No Characterisation in depth of Head checking: Yes	Yes	Yes	Yes
Can assess skewed cracks	Yes	Yes	Yes	Yes
Can operate at high speed	?	Yes	Yes	Potentially
Potential stand-off from rail			4-5 mm	1-2 mm

Minimum crack size detection (based on current laboratory tests)	2 mm (Detected and characterised in depth)	2 mm	2 mm	2 mm
--	---	------	------	------

Table 9 –Capability table

3.1.5 Applicability of methods for industrial exploitation

In addition to focussing experimental tests, WP4.4 has also considered the relevance of the novel techniques to industrial requirements. The industrial requirements elicited from ProRail are shown in Appendix 3.

The table below shows the evaluation of the novel methods against the industrial requirements, as well as providing information regarding cost and the current state of development.

Fill in the cells for each method using the colors in the heading lines (except for cost)

All CEA methods have been evaluated in laboratory with existing (i.e. not totally dedicated) probes. Further work needs to be done to evaluate these methods on field.

Method	Operational requirements (Velderman's ProRail document)											Industrial stage	Cost (order of magnitude in €)	Remark								
	2.1	2.2	2.3	2.4	2.5	2.6	2.7	3.1	3.2	3.3	3.4				3.5	3.6	3.7	3.8	3.9	3.10	4.1	4.2
	C	I	NC	F	NA	C	I	NC	F	NA	C				I	NC	F	NA	C	I	NC	F
Squat characterization																						
UT - 3D-electronic scanning (CEA)																						
UT - Through transmission (CEA)																						
UT - Laser (CEA)																						
Head Cheacking																						
UT - 3D-electronic scanning (CEA)																						
EC - Transmit-receive probe (CEA)																						
EC - Magnetic flux leakage probe (CEA)																						
EC - Flexible array probe (CEA)																						
UT - Laser (CEA)																						
ACFM (BHAM)																						
EMAT (BHAM)																						

* Accuracy of +/- 1mm for walking stick, under evaluation for high speed

3.2 Mapping to infrastructure assets

As this SP 4.4 task is designed to create real operational advances, it is necessary to encompass all aspects of in operational situations. Among these issues are human factors issues, more precisely the need of real-time positioning for site operators in connection with infrastructure asset and previous inspection runs. This applies equally to manual and train-borne inspections.

Modern information and communication techniques offer a wide range of solutions from cutting edge information and communication technology (GPS, mobile phones, PDA, Internet). In the course of SP 4.4, a software prototype called NAVIRE (NAVigate across the Infrastructure by Real Events) has been created.

NAVIRE establishes full compatibility between GPS positioning or geographical coordinates and practical "railgraphic" coordinates (Line index or name, track name, milepost).

This compatibility makes it possible to very easily refer infrastructure data (generally linked to "railgraphic" coordinates) to geographic coordinates. The same is true for inspection results.

Provision has been made to integrate NAVIRE to future PDA (Personal Data Assistant) available for manual or train operators with new software standards.

Some examples of the software capabilities are given on the following images.

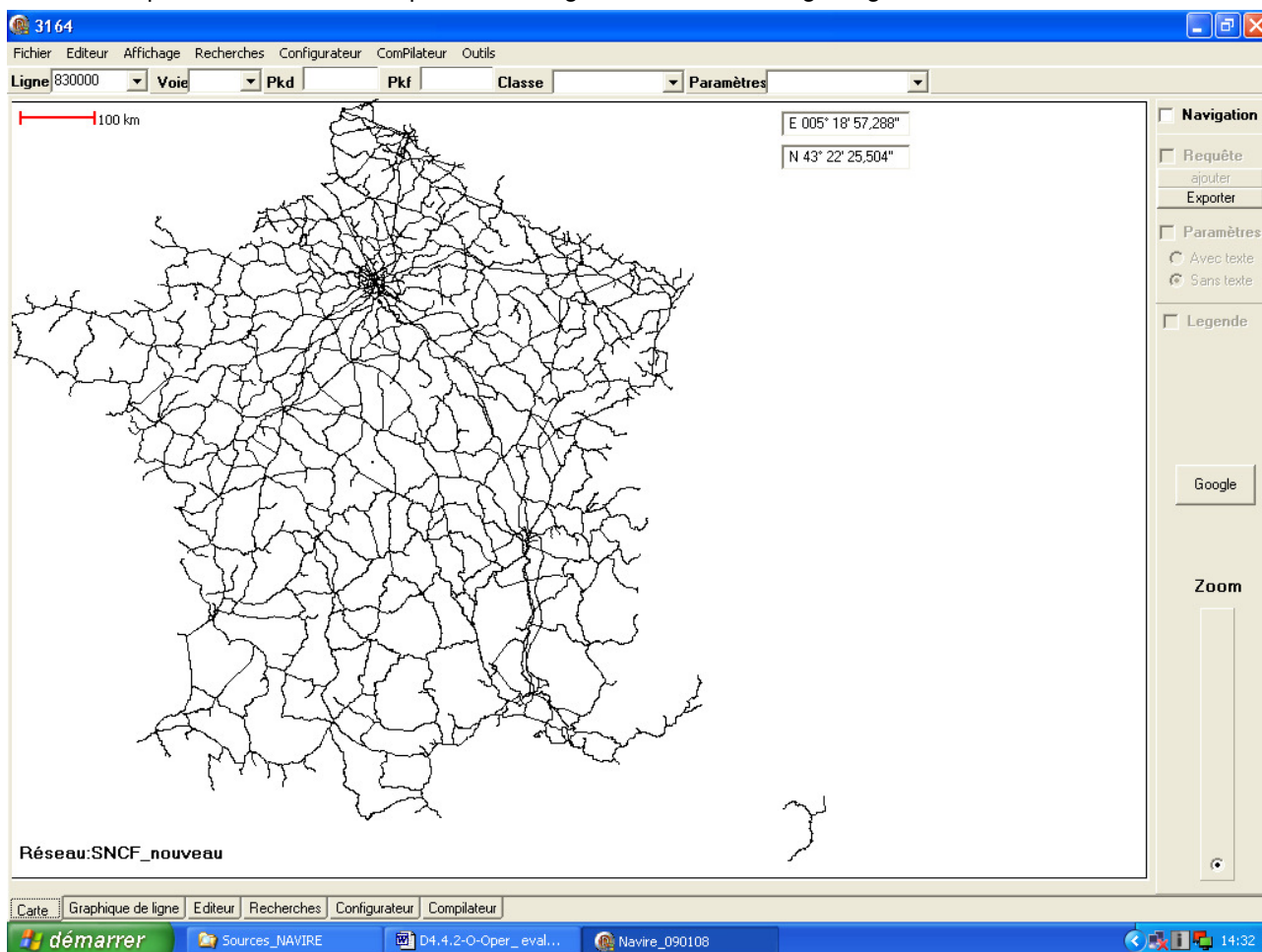


Figure 98 - Layout of the current software NAVIRE platform

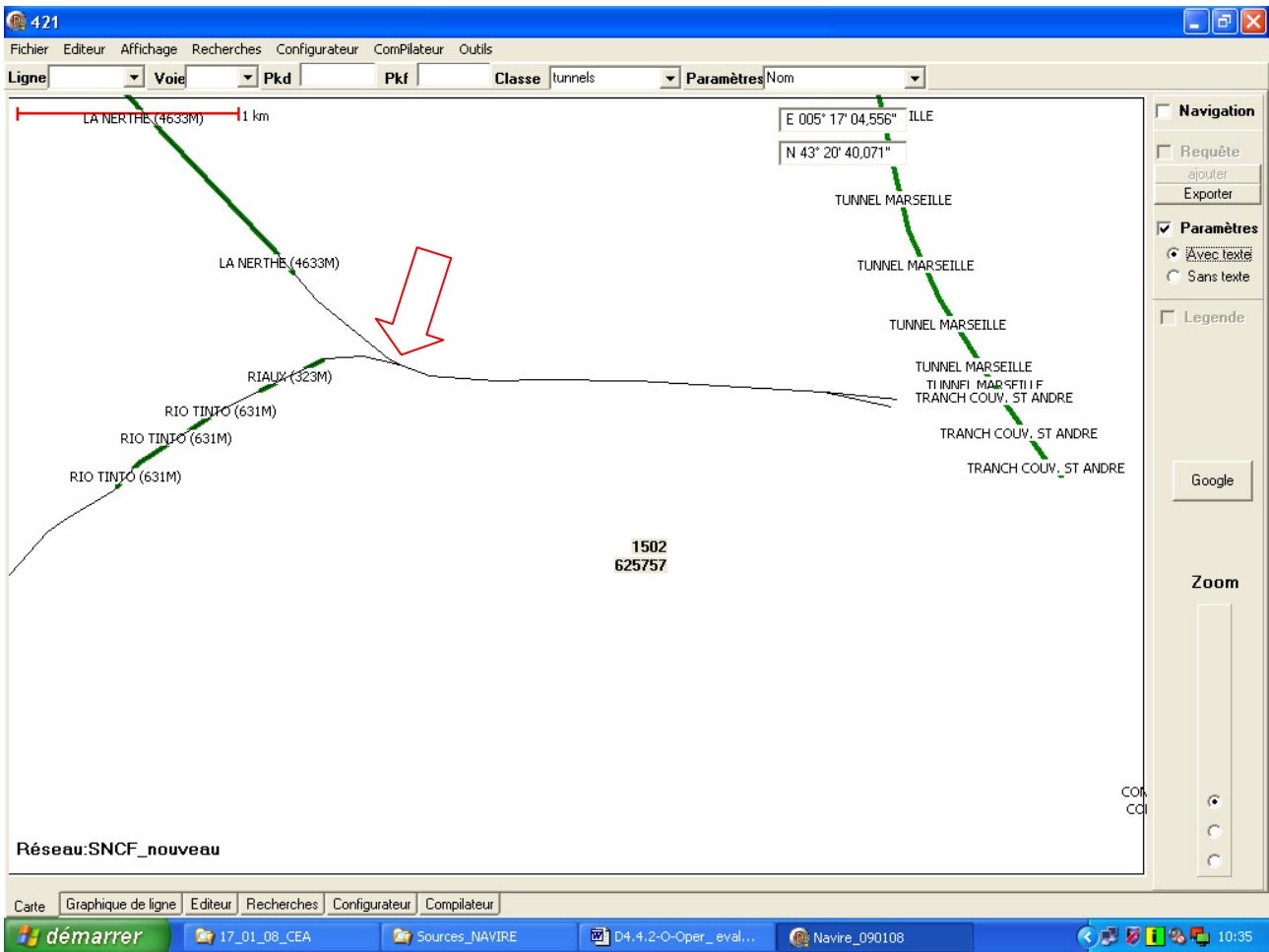


Figure 99 - Display of infrastructure features (tunnels in a selected area near Marseille)

Once a specific location has been selected on the NAVIRE railway map (at the arrow end), an immediate match with a satellite Google photo may be obtained by clicking on the appropriate button.

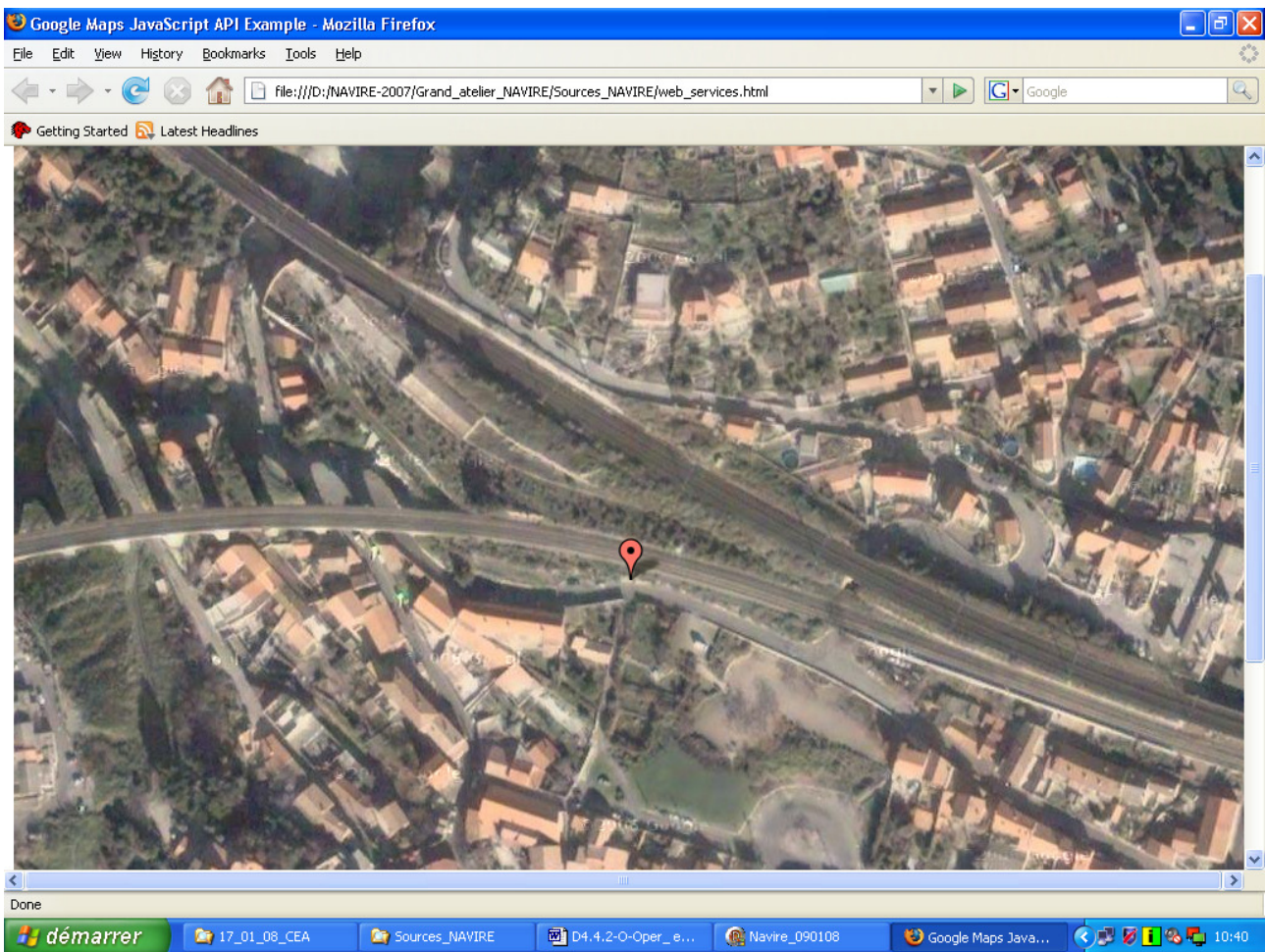


Figure 100 - Satellite view of selected infrastructure features (Figure 99)

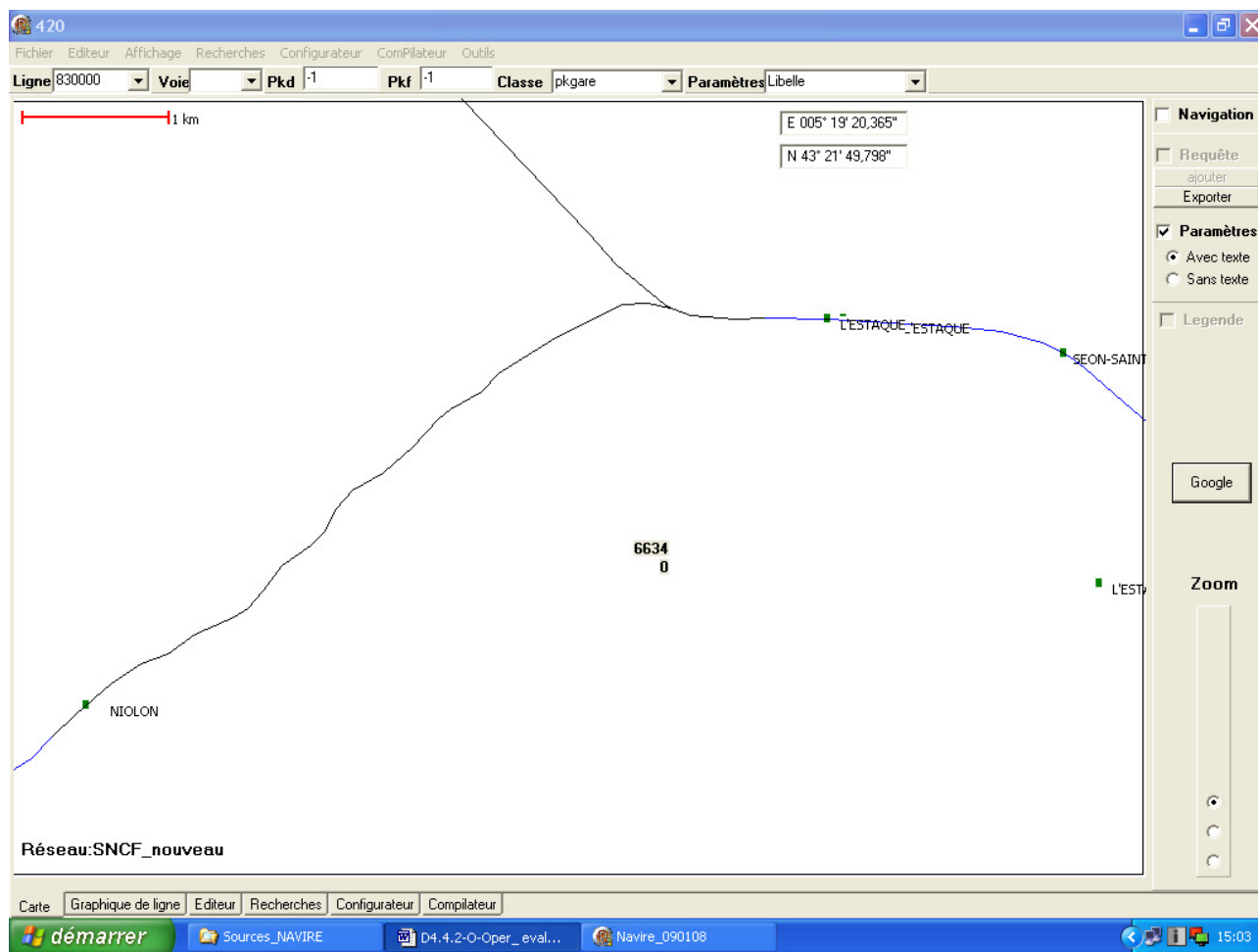


Figure 101 - Display of railway infrastructure features (stations)

A similar example is shown for a different infrastructure asset (a station in the same area).

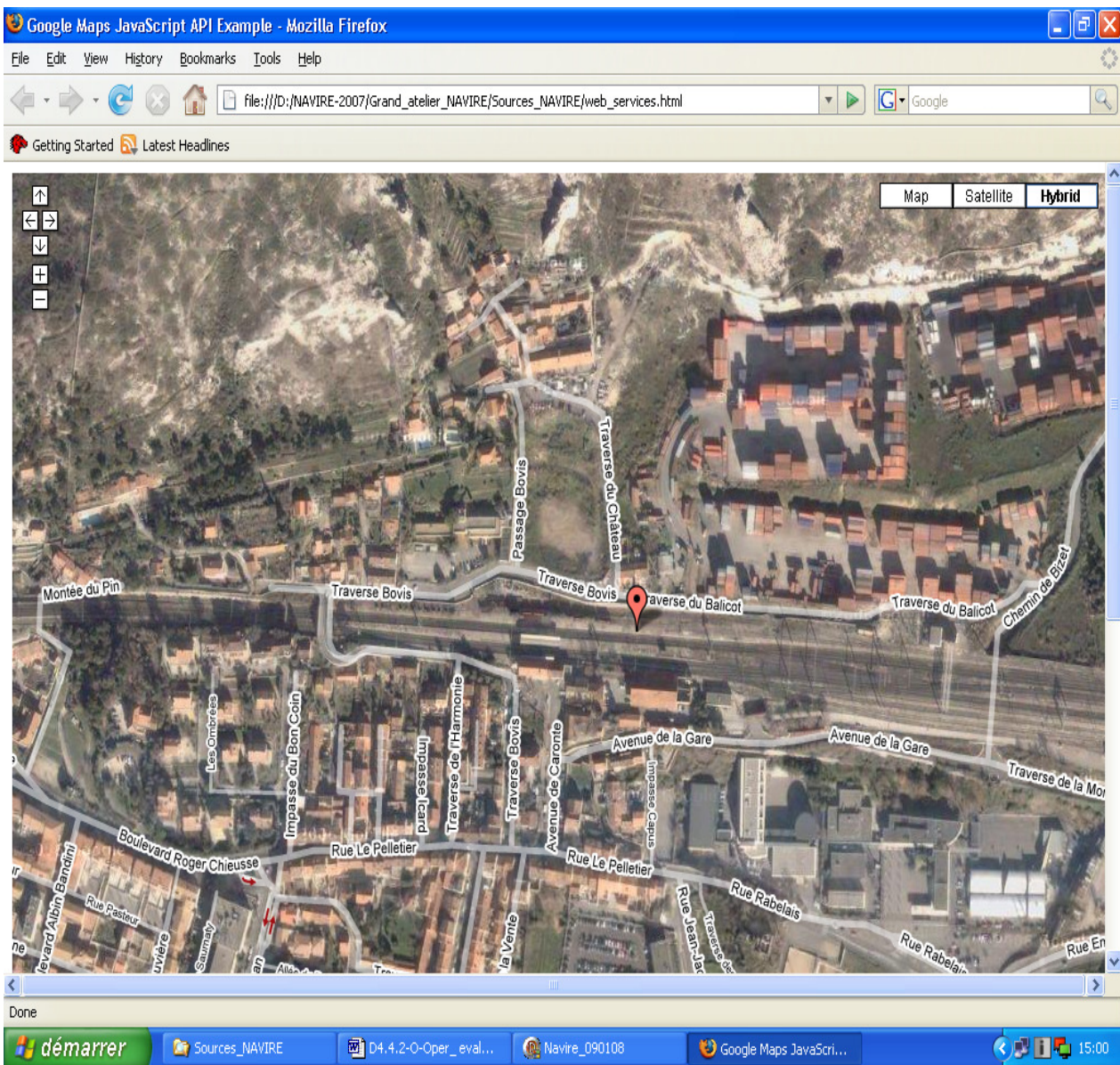


Figure 102 - Hybrid satellite image of the same area (L'Estaque station near Marseille)

Other Internet resources are shown on the following railway maps, which have been downloaded. NAVIRE is equipped with software which transforms track images into geographical coordinates. This is for demonstration purposes only, as the results are not very accurate and must in any case be matched to "railgraphic" coordinates.



Figure 104 - Examples of other railway cases (2/2)

A prototype of NAVIRE software has been built in the first stage T 4.4.2 of the task “Operational evaluation of an inspection demonstrator”. It has been tested successfully in respect of the railway network of SNCF.

The intention is now to extend its use to another railway, possibly the test track which will be chosen for the demonstration stage of T 4.4.3. This will require the input of railway lines and their specific naming conventions (lines and tracks), reference mileposts and the associated geographic coordinates, or whichever system is currently used by the railway authority.

Significant data relating to infrastructure description (previous inspections, various rail types or rail age, curves, etc.) will also be provided for the sake of software evaluation.

4. Conclusions

This report forms the second deliverable within WP4.4 of the INNOTRACK project. The first deliverable, D4.4.1 provided a complete survey of industrial achievement globally in the field of rail non destructive testing. From this initial work, the WP4.4 undertook a detailed technical evaluation of selected techniques in order to addresses some of the fundamental drawbacks and inadequacies of existing methods, as detailed in the introductory sections of this report.

This report provides details of a series of experiments that were undertaken by the University of Birmingham and CEA. The primary purpose of the experiments were to:

- evaluate the ability of novel non destructive testing methods to accurately characterise both manufactured and real defects. There is a need to be able to accurately characterise individual defects in order to make better decisions regarding rail replacement or remedial maintenance;
- test the performance of the methods at speed, which is increasingly important in high capacity railways;

Five different techniques have been evaluated, namely: Phased Array, Eddy Current, Laser, ACFM and EMATs. The process of evaluating the techniques is believed to be original, as most previous studies which have compared techniques have been undertaken by system suppliers who can be biased in the presentation of the results.

In addition, the study focuses on the industrial applicability of the methods. The applicability has been evaluated against a set of industrial requirements developed by ProRail, based on an industrial tender document.

The next phase of the project will further develop the techniques believed to be closest to exploitation for in-service rail inspection. This work will culminate in a track trolley test to be undertaken in conjunction with Network Rail. This assessment is based on the ability of the techniques to provide greatest benefit to infrastructure companies through the use of higher speed defect detection. These experiments will test the real world capabilities of the ACFM, EMATs and Visual Inspection methods, as well as demonstrating the usefulness of new information technology tools for defect mapping and decision support.

5. Bibliography

- [1] **"An international cross reference of rail defects"**, A report commissioned by the Steering Group of UIC/WEC. Joint Research Project 1 – Rail Defect Management, D.F. Cannon, June 2003.
- [2] UIC leaflets R712 "Rail defect catalog" & R725 "Rail defect maintenance"
- [3] " Rail inspection technologies " deliverable issued of INNOTRACK D4.4.1, November 2007.

6. Annexes

6.1 APPENDIX 1- Laser acoustics

The failure of rails is one of most significant causes of the accidents on railroads. Statistics show that 2700 derailments happened on the railroads in the US between 1992 and 2002 [1]. The corresponding cost of the losses was about \$441 millions. For this reason, the development of systems for fast and efficient testing of the rails is an important task for the science dealing with non-destructive testing (NDT). The first cause is a crack in the transversal direction. The usual techniques for the detection of transversal defects in rails are magnetic methods and ultrasonic inspection. The first method may be affected by environmental magnetic noise. It also demands very small working distances for sensor elements. Ultrasonics is a traditional technique of rail inspection. It works on the top of the rail in the regime of excitation, propagation and detection of ultrasonic pulses by Piezo-transducers. They are introduced inside a water-filled wheel. The drawbacks of this ultrasonic technique are the slow velocity of the control and the demand of contact to the rail. Moreover, the problem of the surface shelling exists with this ultrasonic technique. The shelling could prevent the detection of the transversal crack.

An improvement to the ultrasonic technique has been made by the application of powerful pulsed lasers for the excitation of sound pulses [A2]. The prototype of a laser-based ultrasonic inspection system so-called U-Rail is described in [3]. This system uses high-energy lasers to generate ultrasonic echoes in the rail. Air-coupled transducers are then used to control the waves propagating through the rail. A laser pulse of high energy was directed on the rail surface to produce a normal stress in the ablation regime. This ablation on the surface works as an ultrasonic pulse that propagates in the rail. A commercial 50 W Nd:YAG laser has been used for this goal. The laser system was developed on a rail-vehicle. A four-laser system allows the inspection of a rail in one pass at 20 miles per hour. The ultrasonic detection sensor was located at 2.5 inches above the top of the rail. A laser optic triangulation unit allows the position of the rail to be determined. There is also a global positioning system (GPS) for control. The U-rail system includes necessary software for real-time processing of the data.

To avoid the problem of surface shelling and to increase the speed of rail control, the application of guided acoustic waves has been proposed [4]. Guided waves propagate along the rail with a velocity of several kilometres per second. They should not be sensitive to the shelling. All this makes guided acoustic waves very attractive in rail control. To make use of their advantages it is also necessary to develop an efficient contactless method of guided waves excitation. The application of pulsed laser looks very promising for this goal. These lasers are now readily commercially available. The pulse duration of such lasers is typically ~10 ns. Therefore, they allow an acoustic wave to be excited in very large spectrum domain. The efficiency of light to sound conversion could be very high when the regime of ablation is obtained. This regime is accessible for steel if the radiation of a laser is focused on the surface by a short focusing lens. Using spherical or cylindrical lenses it is possible to provide a point- or line-like source on the surface of the material. Then, after propagation in the controlled part of the rail, a guided wave could be detected by air-coupled [5] or electro-mechanical transducers [6].

6.1.1 Principle of sound excitation

Hot photoexcited electrons provide their energy to the lattice during the process of their thermalisation (about 1 ps). Typically, the energy range of commercially available powerful solid-state lasers is in range 0.1-10 J. The threshold of metallic surface ablation is determined by the temperature of solid-liquid transition (500-1000 C). It is easy to see, that the threshold required to liquidise the metallic surface could be achieved by focusing in spots of ~0.1mm in diameter. The ablation regime could therefore be easily achieved with powerful pulsed lasers (with density of energy above 107 W/cm²). In the regime of ablation, the sound pulse is generated by the pressure provided by the portion of material vaporised from the surface of the metallic plate (Figure 105B).

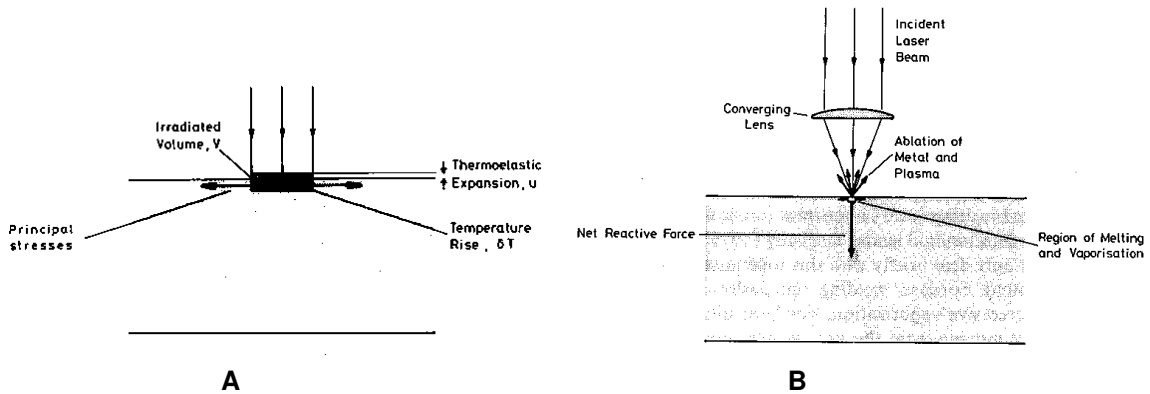


Figure 105 - Sound pulse excitation by thermoelastic (A) and ablation (B) mechanisms [8]

If the density of the laser pulse energy is less than the damage threshold, the excitation of a sound pulse on the surface of the metallic plate is governed by the thermoelastic mechanism [7]. The local temperature rise δT induces corresponding thermoelastic expansion u and stress on the surface of the sample (A). This stress acts like a source for the the ultrasound pulse. The diagrams of sound field have been calculated and measured in [8] for both thermoelastic and ablation regimes (A, B). It is clear from the last picture that the maximum longitudinal wave is normal to the surface in ablation. It is about 60 deg for the thermoelastic regime. In an isotropic medium, the shear wave is generated on the surface due to the coupling between longitudinal and shear-modes. However, there is still a maximum angle (~ 30 deg) for the shear wave diagram. It should be pointed out that the diagram starts to be more directive with the increase in size of the source.

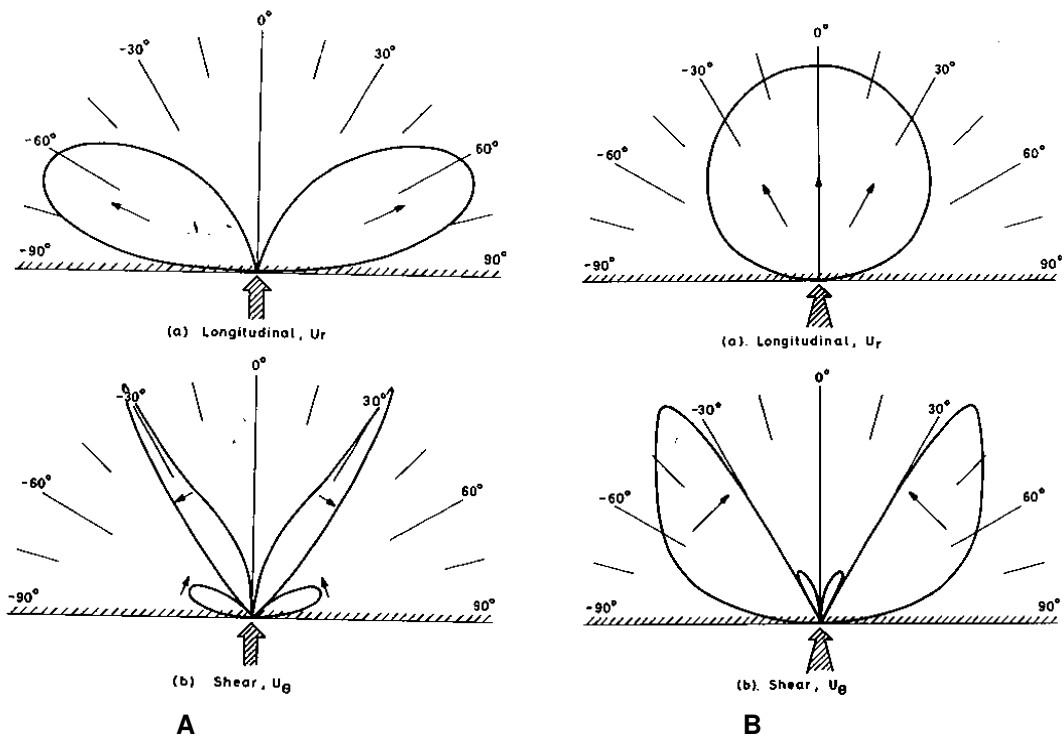


Figure 106 - The diagram of sound excitation by a laser line source. A – thermoelastic; B – ablation regimes [8]

6.1.2 Methods of defects detection

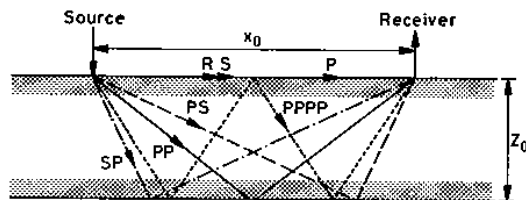
The detection of defects from the echoes

The principle of defect detection in rails is based on the so called time-of-flight technique developed in [9]. It is related to the fact that the tips of defects provide diffraction sources for ultrasound. Then, it is followed by the measurement of the arrival times of the diffracted pulses relative to known arrivals such as echoes from the bounds. The conventional time-of-flight technique normally uses two transducers (a). The first is for the generation of ultrasound (source) and the second is for its detection (receiver).

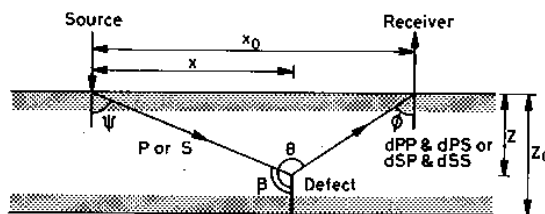
The arrival of different waves in the absence of defect is shown in (a). When the defect is introduced in the sample, the diffracted compression wave (dPP) arrives after the direct wave (P) and before that reflected from the bound compression echo (PP). The direct wave (P) could be completely absent if the defect is located near the surface of detection. Corresponding P, PP and dPP-waves arrival times are described by the relationships:

$$\left\{ \begin{array}{l} T_P = x_0 / c_P, \\ T_P = \sqrt{x_0^2 + 4z_0^2} / c_P, \\ T_{dPP} = \left(\sqrt{x^2 + z^2} + \sqrt{(x_0 - x)^2 + z^2} \right) / c_P, \end{array} \right. \quad (1)$$

where x_0 is the distance between source and receiver, z_0 is the thickness of the sample, (x, z) are coordinates of the defect, c_P is the compression wave velocity.



(a) Wave arrivals in parallel plate



(b) Wave arrivals diffracted by tip of defect

Figure 107 - Time-of-flight technique for defects detection. P, S, R are direct compression, shear and Rayleigh waves; PP is P wave reflected as compression wave, dPP is P wave diffracted as compression wave (other details are in the text of the review) [8]

Laser beams (pulsed laser for pumping and interferometer for probing) could be used as a source and a receiver instead of piezoelectric transducers. It has been shown that the maximum of dPP waves in the geometry (b) appears at the angle ~ 60 deg to the surface normal [10]. This angular condition is important for the optimisation of the set-up for nondestructive testing. Indeed, the interferometer detects only the component of the displacement normal to the surface. It is not therefore maximised for 60 deg geometry. In the regime of ablation the diagram of sound excitation for the compression wave is quite broadband. However, it is at the maximum at 0 deg. The diagram for the thermoelastic regime fits better for the condition 60 deg geometry. All these factors should be taken into account in the development of an efficient schematic for the laser ultrasonic inspection of rails.

The detection of defects from the shadow patterns

The schematic shown in Figure 108 has been proposed for the detection of defects in rails [11]. It is based on a pump-probe laser technique. The beam of a pump laser is directed towards point A on the surface of the sample. The beam of a laser interferometer is focused in point A' located at distance l_0 from point A. If the path of ultrasonic beams is free from discontinuities the interferometer will detect corresponding peaks. If discontinuity appears it will block the sound propagation to create the shadow zone (Figure 108).

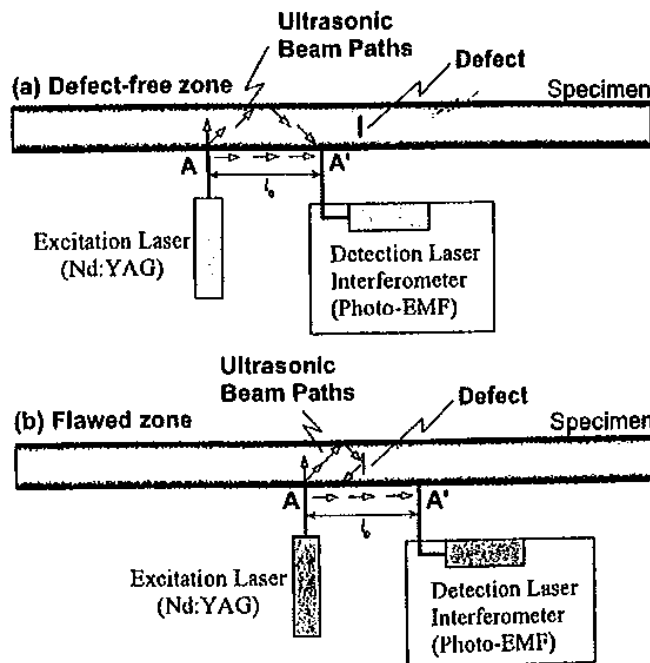


Figure 108 - The experimental set-up for the detection of defects based on the shadowing of ultrasound beam [11]

As already mentioned, the diagram of ultrasound source generation is important for the optimisation of this technique. It provides the estimation of optimal distance $l_0 = 2h/\tan\theta \approx 1.7h$ for the maximising of shear wave peaks while suppressing P waves using the regime of ablation in steel. This distance is constant when the system moves along the studied sample (from point A to D, Figure 109). Shear wave amplitude vs. the scanning distance x provides a picture with two zones of shadow (far and near).

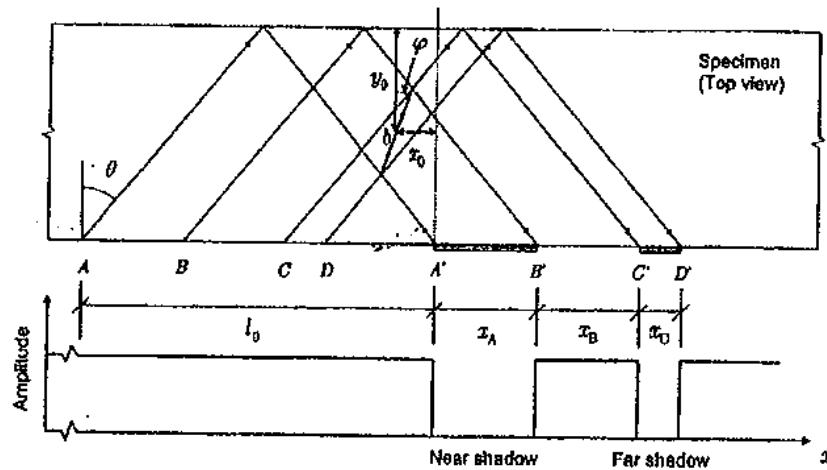


Figure 109 - Near and far shadow zones on the surface due to the blocking of ultrasonic rays (x_0, y_0) – coordinates of the defect; b – size; φ - orientation [11]

Then, the size b and orientation of a defect could be obtained from the following equations [11]:

$$b = \begin{cases} \frac{1}{2} \sqrt{\left(\frac{x_A + x_C}{\tan \theta}\right)^2 + (x_A - x_C)^2} & \text{if } \theta > |\varphi| \\ \frac{1}{2} \sqrt{\left(\frac{x_A - x_C}{\tan \theta}\right)^2 + (x_A + x_C)^2} & \text{if } \theta \leq |\varphi| \end{cases} \quad (2)$$

$$\varphi = \begin{cases} \tan^{-1}\left(\frac{x_A - x_C \tan \theta}{x_A + x_C}\right) & \text{if } \theta > |\varphi| \\ \tan^{-1}\left(\frac{x_A + x_C \tan \theta}{x_A - x_C}\right) & \text{if } \theta \leq |\varphi| \end{cases}$$

The method of shadowing was validated in [11] for a real rail specimen with a transverse internal defect. The calibration was performed with a transducer array to ascertain the parameters of the defect. Despite the rusted and worn rail surface, the measured parameters agree closely with the prediction. It demonstrates a promising ability of the method for the nondestructive noncontact rail testing.

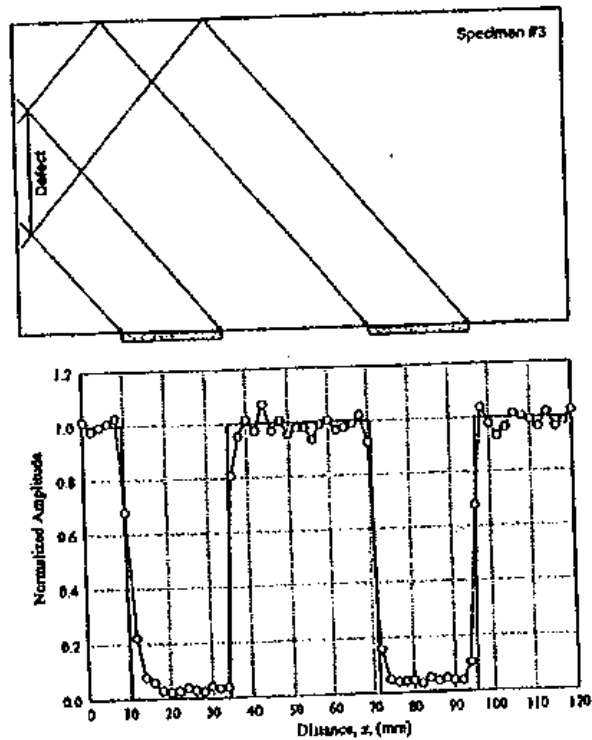


Figure 110 - Shadow pattern provided by a transverse defect in rail [11]

Summary of methods for nondestructive rail testing

Modern methods of defect detection in rails could be divided into categories:

1. Contact excitation and detection of ultrasound. This method is now commonly used now on railroads everywhere in the world.
2. Laser noncontact excitation and transducer for contact or noncontact detection. A prototype [3] and studies [4] of this method have been developed. Air-coupled [5] or electromagnetic [6] transducers are commonly used for this purpose.
3. Laser noncontact excitation and detection of ultrasound. This method is still in the process of development [11]. It looks very promising because of absence of contact with the rail.
4. Contact transducer excitation and laser noncontact interferometer detection. In principle, the schematic of so called 'scanning laser acoustic microscope' (SLAM) could be used for defect detection [12].

6.1.3 Optical methods for ultrasound detection

The surface of the rail does not reflect perfectly. For this reason, one of the goals of this study is to describe an efficient optical method of ultrasound detection on a non-polished surface with diffusive reflection. Numerous methods of optical ultrasound detection are known in literature. The most commonly used methods are [13]:

1. Interferometry.
2. Doppler spectroscopy.
3. Diffraction of laser beam by the grating induced by surface wave.
4. Beam deflection technique.

Interferometric techniques

Laser interferometry fits very well to the condition of nondestructive testing because of the availability of reliable commercial interferometers. The principle of the interferometric technique is shown in Figure 111 [14]. It uses optical heterodyning. A Michelson interferometer in which the probed surface is one of the mirrors is generally used for this goal.

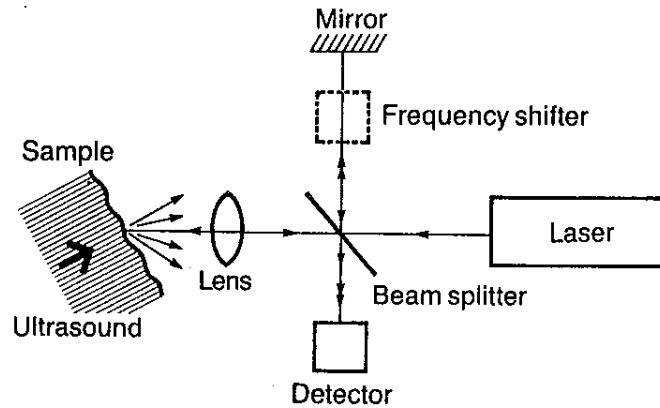


Figure 111 - Optical heterodyne interferometer [14]

The frequency response of the interferometer is limited by the cut-off frequency of the detector. To stabilise the interferometric set-up it is necessary to compensate with low-frequency vibration of large amplitude. The compensation is usually performed by means of the electronic feed-back loop. This loop uses a piezoelectric transducer for the displacement of a reference mirror. The light intensity on the photo-detector is described by the equation:

$$I_D = I_L \left\{ R + S + 2\sqrt{RS} \cos \left(\frac{4\pi\delta(t)}{\lambda} - \Phi(t) \right) \right\}, \quad (3)$$

where I_L is the laser power, R is the transmission of the reference channel, S is the transmission of the signal channel, $\delta(t)$ is the displacement of the sample surface, $\Phi(t)$ is the phase factor, λ is the laser wavelength. To improve the stability and sensitivity of the interferometric set-up, heterodyne interferometers are used [15]. In this case, the frequency of one arm is shifted by a radio frequency f_B . The shift is usually obtained by means of an acousto-optic modulator (Bragg cell). The detector receives a signal at this frequency modulated in phase by the ultrasound and low-frequency vibrations. The simple way to detect the radio-frequency signal is to use a commercial spectrum analyser or VHF receiver tuned to one of the sidebands with following square-law detection. Another way is to use a FM demodulation. This schematic provides a signal proportional to the velocity of the surface. It is also possible with a frequency tracker to obtain a signal related to the displacement of the surface. The following equation is derived from formula (3) for small $\delta(t)$:

$$I_D = I_L \left\{ R + S + 2\sqrt{RS} \left[\cos(2\pi f_B t + \Phi(t)) + \frac{4\pi\delta(t)}{\lambda} \sin(2\pi f_B t + \Phi(t)) \right] \right\}, \quad (4)$$

The electronic circuit including radio-frequency mixer and voltage-controlled oscillator for heterodyne interferometer is described in detail in [15]. Then, electric filters are used to separate the useful signal $\delta(t)$ from a low-frequency background.

When the sample surface is not perfectly polished it provides a speckle picture. According to the so called “Antenna theorem”, only one speckle could be detected in a classical interferometry set-up to measure the surface displacement [16]. A large part of laser power is uselessly lost in this case. In addition the speckle picture could be variable if a scan of the sample is performed. This instability provides variations of signal level which could in principle affect the measurement result. For these reasons, the application of the heterodyne interferometers in industry seems to be problematic. To remove the limitation of the interferometry related to the detection of only one speckle, it is possible to match irregular wavefronts of reference and signal channels. The first approach to this is used in Long-path interferometers. It is based on Doppler shift of the scattered light frequency due to the movement of the surface. The principle of it is shown in Figure 112.

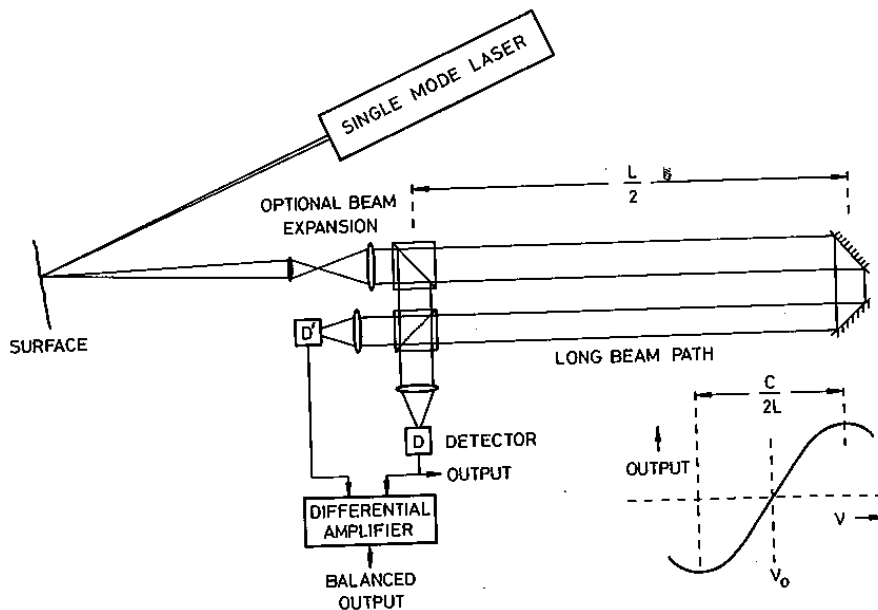


Figure 112 - Long-path interferometer [8]

The surface of the sample is illuminated by a single mode laser. The scattered light is collected by the objective and transformed in a parallel beam which is divided into two parts by a beam splitter. An optical path L of several meters is introduced in one of the beam paths. Then the beams interfere after the second beam splitter to be detected by a balanced photodetector. It has been shown in [8] that the output of the photodetector is proportional to the velocity of the surface u according to the formula:

$$I_D = \frac{4\pi Lu}{c\lambda} I_L \quad (5)$$

It is clear that the light demodulation is obtained in a Long-path interferometer due to the interference of light with itself after some delay. It was expected that this technique would not be sensitive to the optical phase. However the irregular wavefront after the propagation of several meters does not exactly match the initial one. For this reason, the feasibility of Long-path interferometers is still limited.

Another approach to reduce the influence of irregular light scattering has been used in confocal Fabry-Pérot interferometers. Their optical design is shown in Figure 113. All the beams are superimposed after two round trips. It provides the possibility of obtaining an acoustic signal from many speckles. The interferometer with a 90 % reflectivity of mirrors at a 50 cm distance provided 10 MHz bandwidth [14]. The bandwidth could be changed by the changing of the reflectivity of the mirrors.

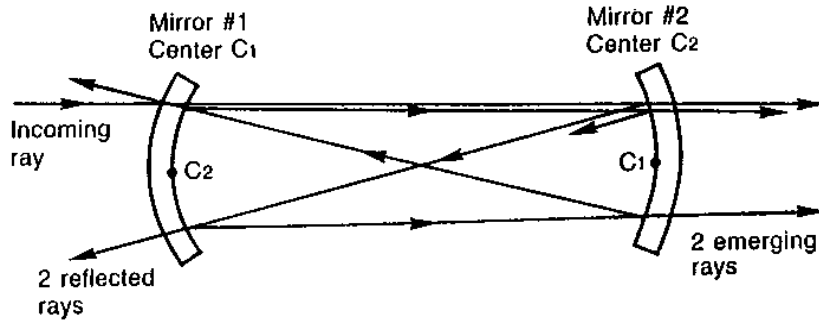


Figure 113 - The design of Fabry-Pérot interferometer [14]

A Fabry-Pérot interferometer allows the effective path length difference to be significantly increased. In comparison, a 50 cm Fabry-Pérot etalon provides 1.5 MHz bandwidth with enough high reflecting mirrors. A long-path interferometer should provide a 50 m path difference to obtain this bandwidth. A significant drawback of the Fabry-Pérot interferometer is the presence of frequency and phase dependence of the response. Indeed, if it is directed to measure the vibration of the surface $\delta(t)=U\cos(2\pi f_u t)$ the output signal is expressed as following [14]:

$$I_D = I_L \left\{ 1 + \frac{4\pi U}{\lambda} S(f_u) \cos(2\pi f_u t + \phi(f_u)) \right\}, \quad (6)$$

where $S(f_u)$ and $\phi(f_u)$ are the amplitude and phase response, respectively. Typical responses are shown in Figure 114 [14].

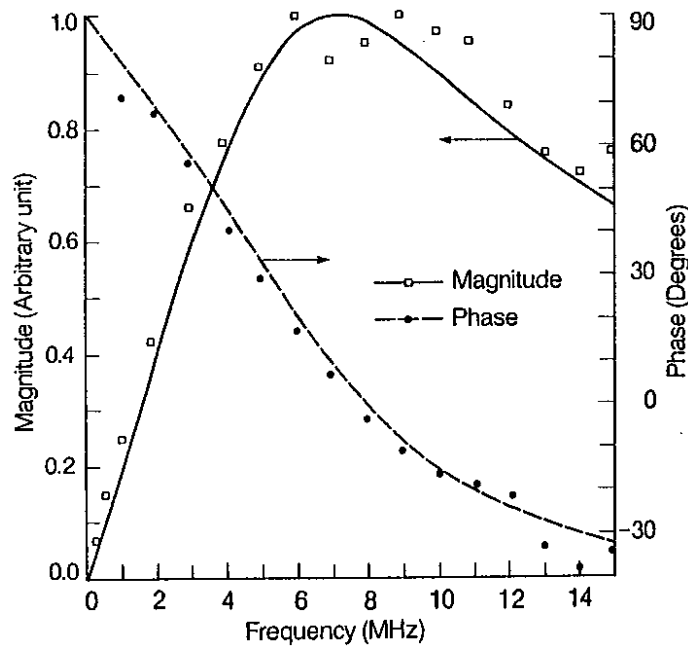


Figure 114 - The ultrasonic frequency response of a Fabry-Pérot interferometer (50 cm base; 10 MHz bandwidth) [14]

It is clear for this reason that the detection of the shape of wide-band ultrasonic pulses could not be performed by a Fabry-Pérot interferometer without distortion. The problem of the adaptation of signal and reference wavefronts in an interferometric system could be solved using two-wave mixing (TWM) in a photorefractive crystal [17]. In this case, the reference beam is created by the diffraction of a pump beam by the hologram written by both pump and signal beams. A heterodyne interferometer with Double Phase Conjugate Mirror (DPCM) is shown in Figure 115.

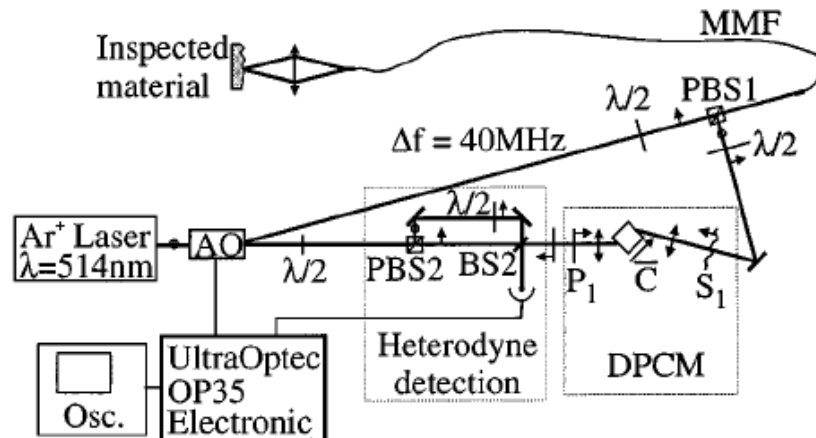


Figure 115 - Set-up of a heterodyne interferometer with Double Phase Conjugate Mirror [17]

PBS1 and PBS2: polarising beam splitters; BS2: beam splitter; $\lambda/2$: half-wave waveplate; MMF: multimode optical fiber; AO: acousto-optic modulator.

The radiation of a single mode argon laser (514 nm) is modulated by an acousto-optic modulator at 40 MHz to provide a corresponding frequency offset between the two beams. One part of the direct beam is directed on the photorefractive crystal BaTiO₃ to provide DPCM. The second part serves as a reference beam for the heterodyne interferometer. The deflected beam is introduced in a multimode optical fibre (MMF). The light scattered on the surface of the inspected material is then introduced into the fibre by the objective. The speckled beam after MMF is coupled in the photorefractive crystal to obtain a signal beam with a plane wavefront for the heterodyne interferometer. This system was tested on aluminium plates with rough surfaces. The limitation of a heterodyne interferometer with DPCM is related to the time response of the photorefractive crystal. It could be improved by choosing a photorefractive crystal with a short turn-on time. The speckle picture must be stable in time. For this reason, a heterodyne interferometer is very sensitive to low-frequency vibrations of large amplitude. These may come from, for example, vibrations of the optical table and the fixation elements of the sample. The industrial application of this kind of interferometer is therefore very problematic.

To our best knowledge, interferometers with DPCM with existing photorefractive crystals are not able to work in noisy conditions. Unfortunately, this is the case when a car of the train moves.

To avoid the problem of the stability of the speckle picture with moving rough surfaces, the multi-channel quadrature (MCQ) interferometer has been proposed [18]. It combines a classical Michelson interferometer schematic and an innovative multi-speckle processing technique. This design was provided by the use of an array of photo-detectors with the following processing of their signals. Each element of the array collects practically one speckle. The optical schematic of a MCQ interferometer is shown in Figure 116(A).

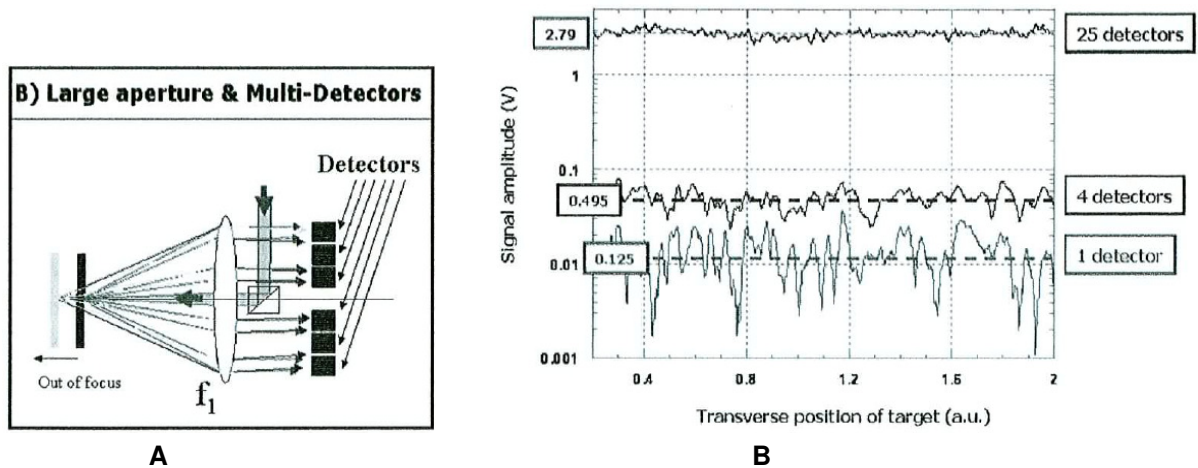


Figure 116 - A: Optical design of a multi-channel quadrature interferometer. f_1 is a collimation lens. B: comparison of quadrature interferometers with 1, 4 and 25 detectors [18].

Averaged amplitude of the signal is marked in square.

The reference beam was expanded to fill the whole area of detection. The demodulation was done in parallel for each channel to provide the output signal. The combination of a quadrature design with the multi-channel schematic allows it not to be sensitive to low-frequency vibrations and to obtain high sensitivity to high-frequency displacements, correspondingly. The comparison of quadrature interferometers with 1, 4 and 25 photo-detectors is shown in Figure 116 (B). The signal amplitude on a rough surface is plotted vs. the position of the sample. It is clear from this picture that the increase in the number of photo-detectors provides amplification of the signal amplitude and improves stability. The increase in amplitude is approximately proportional to the number of elements. The blackouts are already absent for the 4-element detection.

Non-interferometric techniques

Several non-interferometric methods exist for the measurement of the displacements. Ultrasound detection based on beam deflection technique is a simple and reliable method when the detection surface is optically polished [15]. The principle of it is shown in Figure 117.

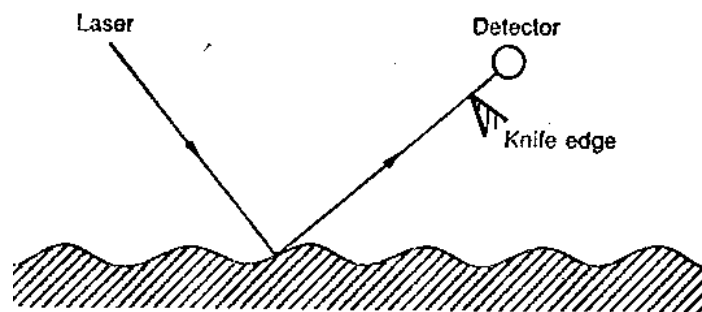


Figure 117 - Beam deflection technique of ultrasound detection [15]

Ultrasonic waves induce local curvature on the surface of the sample under study. Then, a probe laser beam is reflected from the area of surface distortion. The angle of beam deflection is governed by the local slope in the point of reflection. To detect the beam deflection a simple knife edge technique can be used [2]. This technique provides good sensitivity of detection. However, the industrial application of the beam deflection technique is limited by the necessity of using a good polished surface.

Type of interferometer	Influence of surface quality	Frequency bandwidth, MHz	Sensitivity, pm	Perspectives of industrial application
Fabry-Perot Confocal	absent	2-100	3	Applicable in the industry
Heterodyne Michelson	strong	0.01-40	15	Not for industry, Laboratory use only
Photo-refractive interferometer	absent	0.01-300	<3	Not applicable in conditions of ambient acoustic noise
Multi-channel quadrature	absent	0.1-20	subnanometric	Promising for industrial applications
Photo-EMF detector	absent	0.05-100	30	Potentially applicable if sensitivity could be improved. Few commercial systems exist [14]

Table 10 - Comparison of ultrasound detection systems

The application of a laser ultrasound detection system to the non-destructive control of rail demands not only the absence of surface quality influence but also high sensitivity. Moreover, it is necessary to use the system in the quite noisy conditions of a moving car of the train. According to Table 10, the multi-channel quadrature interferometer (MCQ) [18] could satisfy all these conditions. Recently, a new version of such an interferometer was tested by Bossa Nove Tech for measurements on the surface of a rotating disc with a highly diffusive surface [25]. It was clear from this test that the result of ultrasonic measurement does not depend on the speed of the surface displacement in the range 0-10 km/h.

6.1.4 Optical detection of ultrasound for industrial applications.

Commercial availability is an important factor which should be taken into account during the building of systems for non-destructive testing. The parameters of several prospective commercial interferometers available on the market are shown in Table 2.

Company	Model	Type	Wavelength, nm	Sensitivity, nm/Hz ^{1/2}	Bandwidth, MHz
Bossa Nova Tech [25]	Quartet	MCQ	532	10 ⁻⁵	0.1-20
Bossa Nova Tech	Tempo FS200	TWM	532	2 10 ⁻⁷	0.1-120
Tecnar [26]	TWM-1500	TWM	1064	2 10 ⁻⁷	0.0015-15
Tecnar	TWM-1000	TWM	1064	2 10 ⁻⁷	
Tecnar	TWM-1200	TWM	1064	2 10 ⁻⁷	
Tecnar	TWM-1500	TWM	1064	2 10 ⁻⁷	0.003-15
Tecnar	FPC-1000	CFP	1064	2 10 ⁻⁷	0.0015-15
Tecnar	FPC-1200	CFP	1064	2 10 ⁻⁷	
Tecnar	FPC-1500	CFP	1064	2 10 ⁻⁷	0.0015-15

Company	Model	Type	Wavelength, nm	Sensitivity, nm/Hz ^{1/2}	Bandwidth, MHz
Tecnar	FPC-12000	CFP	1064	2 10 ⁻⁷	0.0015-15
Polytec [27]	OFV-5000	H	633		0.001-24
Polytec	OFV-2500	H	633		Up to 24
Lasson [20]	AIR-532-TWM	TWM	532	2 10 ⁻⁷	Up to 125
Lasson	AIR-532-EMF	EMF	532	1.2 10 ⁻⁶	0.1-10

Table 11 - Commercially available interferometric systems

H: heterodyne.

TWM: two-wave mixing heterodyne.

CFP: Confocal Fabry-Perot.

MCQ: Multi-channel quadrature.

Ultrasonic systems including interferometers for detection and powerful pulsed laser for excitation are promising for several areas of industry. They can be used on curved, remote, hot or hardly accessible surfaces. For instance, the confocal Fabry-Perot interferometer has already found application in the production of hot rolled steel [28]. The studies of the processes in high temperature steel have been performed at several laboratories around the world (AEA, IMI, IZFP) [29,30]. The principle of measurement is related to the determination of the size of steel grains from the attenuation of 15 MHz longitudinal ultrasound (Figure 109).

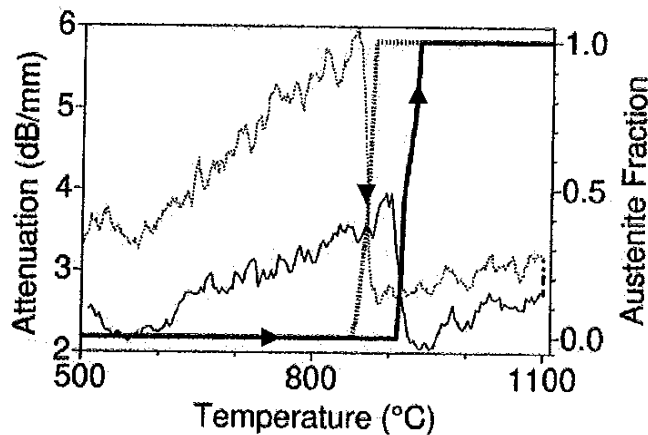


Figure 119 - Attenuation of 15 MHz ultrasound and Austenite of the steel vs. the temperature [29]

Another parameter which is important in the metal industry is the temperature of recrystallisation. The studies of ultrasound velocity in steel with low carbon level have been performed at AEA [31]. It is clear from Figure 120 that the control of recrystallisation is possible if the velocity of ultrasound is measured with a precision of ~0.5 %.

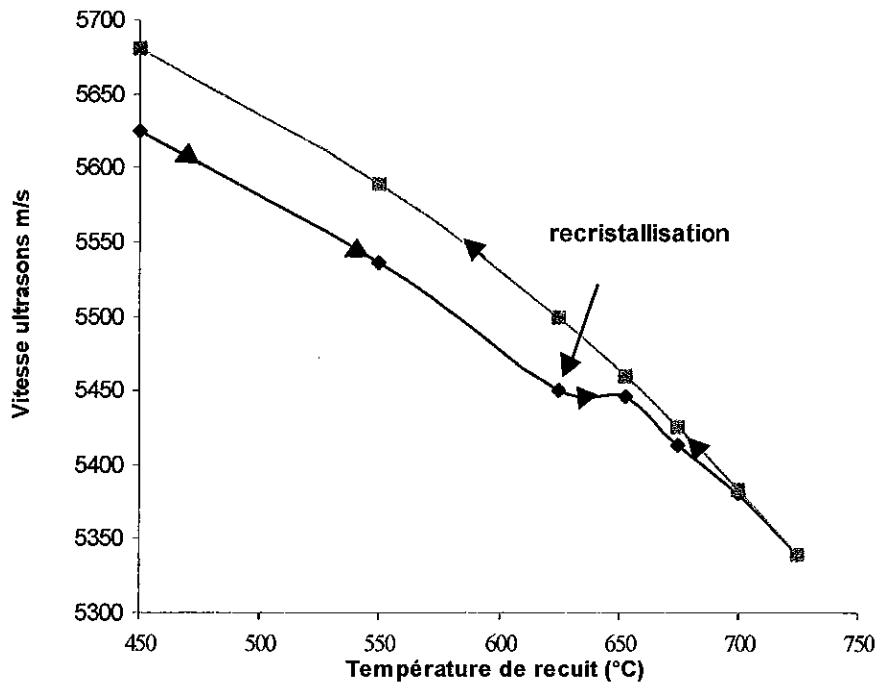


Figure 120 - Ultrasound velocity in steel vs. the temperature [31]

Another parameter of interest in the industry is the thickness of plates and pipes. It is important to keep the thickness stable during the preparation processes. A laser ultrasonic technique was applied to this aim at Algoma Steel and Mannesmann steel producing companies [32]. The schematic of the laser ultrasonic equipment is shown in Figure 121.

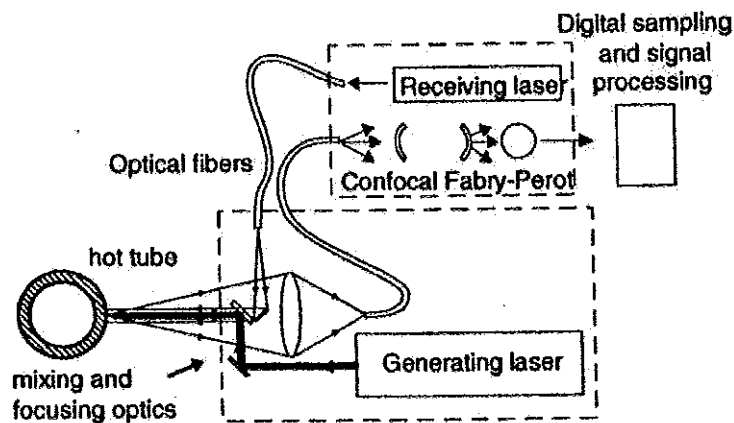


Figure 121 - The schematic of laser ultrasonic equipment used at Algoma Steel company [32]

The ultrasonic testing system included a pulsed laser for the excitation of sound on the wall of the pipe. The short pulse of ultrasound was propagated in the wall and reflected several times to create a set of echoes. From the periodicity of ultrasonic echoes it was possible to assess the thickness of the pipe at a temperature of ~1000 C. Then, laser ultrasonic measurements were compared with the results of tests performed by means of a hand-held thickness gauge (Figure 122).

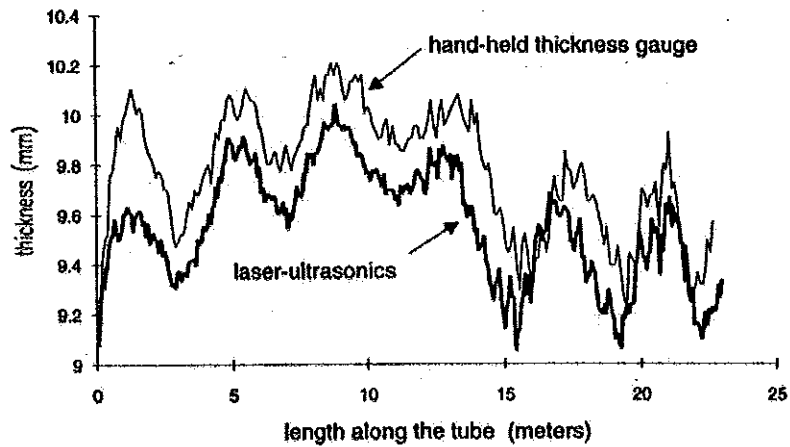


Figure 122 - The thickness profile of pipe wall [32]

Good coincidence between the two measurements was obtained.

During the last 10 years several prototypes of industrial laser ultrasonic systems were installed in aerospace industry (at the McClelland Air Force Base in California, and Aerospatiale and Dassault Aviation in France) [21].

Recently, Bossa Nova Tech developed the system SOPRANO dedicated to industrial applications [25]. This system includes the following elements: MCQ-interferometer Quartet for ultrasound detection; nanosecond Nd:YAG laser (1064nm, 200 mJ); 2D scanner of generation laser; an oscilloscope for data acquisition; PC for storage and processing of data (Figure 123). Being a turn-key system, SOPRANO is aimed on wall thickness measurement of metallic and non-metallic tubes and pipes, defect detection in welding and other applications.

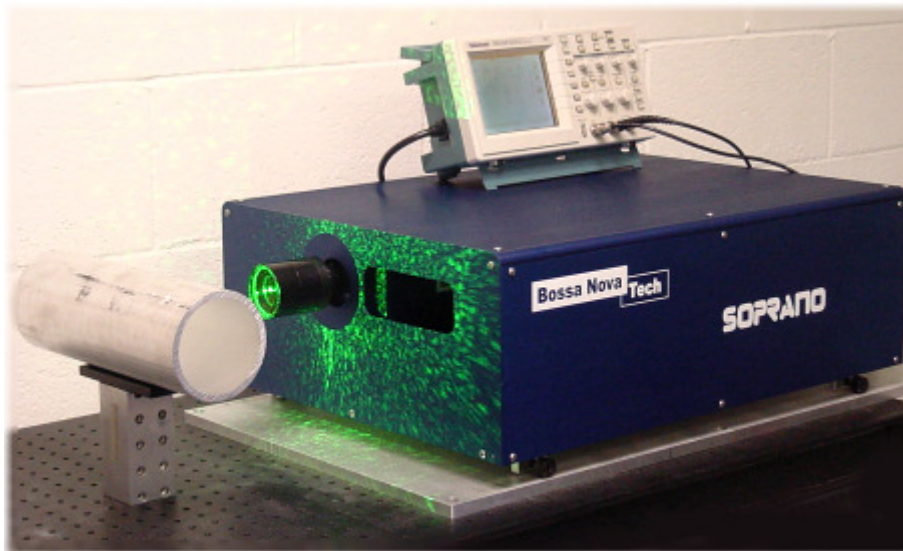


Figure 123 - SOPRANO system [25]

The quartet interferometer is the key element of the system. Important properties of a multi-channel Quartet interferometer are as follows: absence of any stabilisation or compensation system; high sensitivity which is not sensitive to the surface diffusion properties; reliable price. All of these properties make the SOPRANO system attractive for industrial applications.

6.1.5 Laser ultrasonics for rails testing: prototypes

Several non-contact systems for the testing of rails have been developed and successfully tested during the last five years. In 2005 a US Patent named “Laser-air, hybrid ultrasonic testing of railroad tracks” was obtained for the system Laser-Air Hybrid Ultrasonic (LAHU) [33]. It includes a powerful laser source for the excitation of sound and an air-coupled transducer for the detection.

A pulsed Nd:YAG laser (1.06 μm , 10 ns, energy in the range of 0.1-10 J) is used to generate ultrasound as bulk, surface, plate and other guided waves (Figure 124).

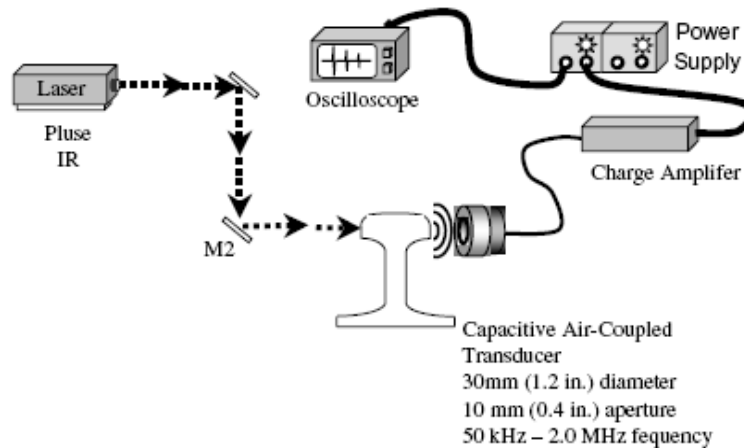


Figure 124 - Laser-Air Hybrid Ultrasonic (LAHU) system [33]

The region illuminated by the laser light can be formed into a circle, rectangle, circle array, rectangle array or other more complex geometrical area configurations. It allows control of the frequency, waveforms and other characteristics of the generated acoustic wave. The laser can work in the thermoelastic, intermediate, ablative or constrained regimes of sound pulse excitation. The constrained regime is obtained by wetting the surface of the rail with a layer of water, oil or grease. Longitudinal, shear and surface waves are then generated simultaneously.

For the contactless detection of ultrasound, capacitive air-coupled ultrasonic receivers with working frequencies in the range 0.05-3 MHz are used. They are capable of detecting ultrasound at distances exceeding 15 cm and are not critically dependent on precise orientation or alignment. The system was optimised for the evaluation of vertical split heads (VSH) and base defects in rails. Corresponding configurations of air-coupled transducers were arranged to detect these defects.

In March 2006 a prototype of the machine for rail inspection was tested by the US Federal Railroad Administration (FRA) in collaboration with the group of researchers at the University of California, San Diego (UCSD) [34]. The principle of this system operation is similar to [33]. It was announced that the system can scan the cracks during the movement at a velocity of 112 km/h. It is certainly much faster than all existing commercially available systems (less than 50 km/h). It gives the location of the defect along the rail, and its depth.

The system consists of a platform the size of a double bed on four small rail track wheels. Pulsed laser on the top of the platform works in the ablation regime of the rail surface to generate strong waves of ultrasound propagating along the rail. An air-coupled transducer (microphone) is positioned at a distance of 30 cm from the excitation source and about 7 cm from the rail surface to detect ultrasound. Then, the computer is used to analyse the signals. This system was designed on the basis of the experimental work performed in the group of F. Lanza di Scalea [1].

The previous two systems used microphones for the detection of the ultrasound wave. The microphone provides a limitation to the frequency range of the detected ultrasound. Conversely, the application of an optical technique of sound detection should significantly broaden this range. This is important for the

improvement in space resolution of cracks detection. Several groups in the world are working on this task. A group working at Brodby, Denmark has developed a Laser Ultrasonic system for Rail Inspection (LURI) [35].

The basic principle of the LURI system is shown in Figure 82. Generation of ultrasound in the rail is performed in the ablation regime by a sufficiently powerful laser. In order to inspect rails during movement with appropriate spatial resolution, the laser operates at sufficiently high repetition rates. Bulk longitudinal, shear, surface-skimming mode and Rayleigh waves are generated in the rail via steel ablation.

The ultrasonic modes are reflected and scattered by the free surface of the rail body and possible flaws inside the rail body or breaks of the surface reach the predetermined receiving point where they are detected by means of a confocal Fabry–Pérot interferometer (CFPI). This kind of interferometer has been chosen since the running surface of the rail is optically rough. For this reason, the scattered light has a speckle pattern that continuously changes during movement of the detection laser and causes speckle noise. The CFPI allows significant suppression of a speckle noise pattern. It is reported that ultrasonic measurements were possible on fast rotating discs at more than 100 km/h.

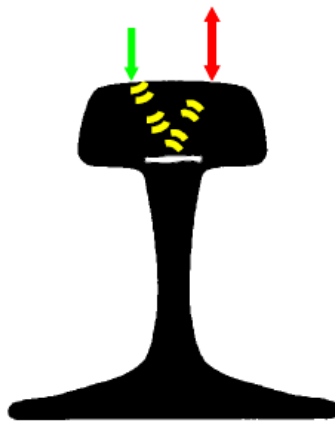


Figure 125 - Basic principle of LURI [35]

A LURI was dedicated to inspect rails of the European profile UIC 60. The dimensions of this profile are: 172 mm in height, 72 mm in surface width and the weight of 60 kg/m. The LURI has been tested on the following types of defect according to the convention of the International Union of Railways (UIC) convention [35]:

- UIC Code 211 – progressive transverse cracking of the head,
- UIC Code 212 – horizontal cracking of the head,
- UIC Code 213 – longitudinal vertical crack in the rail head,
- UIC Code 221.2 – long groove at the running surface,
- UIC Code 2321 – horizontal cracking at the fillet radius between the web and the head of the rail,
- UIC Code 200 – complete vertical (transverse) rail break.

The optical part of the system is mounted on a special vehicle attached to the bottom of a railroad car. The optical equipment includes the two lasers with focusing optics and the CFPI with detectors. All the optical parts are mounted on an acoustically isolated plate which is attached to the frame of the vehicle. The beam is focused to a line on the surface of the rail. The proper lengths of the generating beam spot have been found by means of computer simulations and test experiments. The system currently performs one-rail inspection but may be extended to inspection of both rails. This arrangement of the system allows movement with speeds up to 40 km/h.

Optimal arrangements of pump and probe spots are shown in Figure 83. The arrangement shown in Figure 126 is dedicated for detection of defects with UIC codes 2321, 212, and 211. The arrangement shown in Figure 126B allows testing of defects with UIC codes 213 and 221.2. Both of them are able to detect a complete rail break (defect UIC code 200).

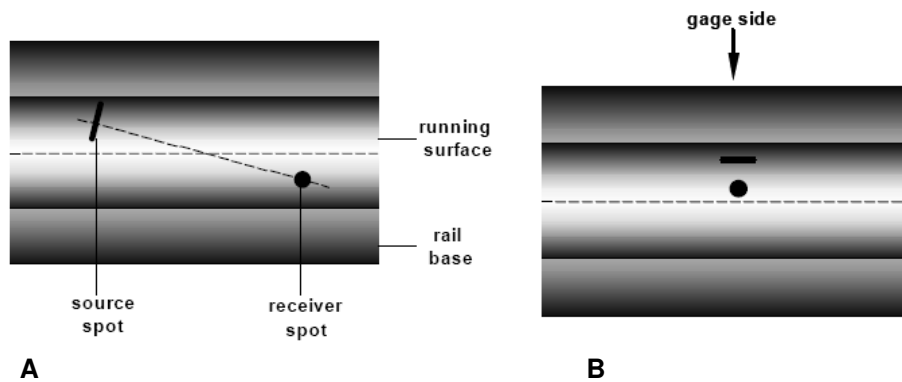


Figure 126 - Optimised configurations of pump and probe for LURI system [35]

Several words should be said about the limitation of speed to 40 km/h for the LURI. This limitation makes the system even slower than traditional testing cars with the transducer wheel. Firstly, the energy and the repetition rate of the generating laser were limited. Secondly, the mechanical design of the railroad car is currently not robust enough to reach higher inspection speeds. Both limitations are not fundamental. There is hope that they would be solved in the future.

6.1.6 Bibliography on laser ultrasonics study

1. F. Lanza di Scalea, P. Rizzo, S. Coccia, I. Bartoli, M. Fateh, E. Viola and G. Pascale, "Non-contact ultrasonic inspection of rails and signal processing for automatic detection and classification", *Insight* **47**, N6, 1 (2005).
2. D. Royer "Génération et détection optiques d'ondes élastiques".
3. Greg Garcia, "U-rail laser-based ultrasonic inspection system prototype "system overview and status", *Railway Track & Structures*, N10, 19 (2006).
4. P. Wilcox, M. Evans, B. Pavlakovic, D. Alleyne, K. Vine, P. Cawley and M.J.S. Lowe "Guided wave testing of rail", *Insight* **45**, 413 (2003).
5. S. Kenderian, B.B. Djordjevic, R.E. Green, D. Cerniglia, "Laser-Air Hybrid Ultrasonic testing of railroads tracks", US Patent application publication 2004/0003662 (2004).
6. G. Alers "Railroad rail flaw detection system based on electromagnetic acoustic transducers", Report DOT/FRA/ORD-88/09, US Department of transportation (1988).
7. V.E. Gusev, A.A. Karabutov, "Laser optoacoustics", NY, AIP (1993).
8. C.B. Scruby, L.E. Drain, "Laser ultrasonics. Techniques and applications", NY, Adam Hilger (1990).
9. M.G. Silk "Research techniques in nondestructive testing", V.3, NY, Academic (1977).
10. J.A. Ogilvy, J.A. Temple "Diffraction of elastic waves by cracks: application to time-of-flight inspection", *Ultrasonics* **21**, 259 (1983).
11. Shi-Chang Woo, Jiyang Wang, Review of quantitative nondestructive evaluation V.21, pp. 1819-1826 (2002).
12. E.P. Rudd, R.K. Mueller, W.P. Robbins, T. Skaar, B. Soumekh, Z.Q. Zhou, "Scanning laser acoustic microscope with digital data acquisition", *Rev. Sci. Instrum* **58**, 45 (1987).
13. D. Royer, E. Dieulesaint, "Ondes élastique dans les solides", Paris, Masson (1999).
14. J.-P. Monchalain, R. Héon, "Laser ultrasonic generation and optical detection with a confocal Fabry-Pérot interferometer", *Materials evaluation* **44**, 1231 (1986).
15. J.-P. Monchalain "Optical detection of ultrasound" *IEEE Transactions on ultrasonics, ferroelectrics and frequency control* **33**, 485 (1986).
16. A. E. Siegman, "The antenna properties of optical heterodyne receivers", *Appl. Opt.* **5**, 1588 (1966).

- 17.P. Delaye, A. Blouin, D. Drolet, J.-P. Monchalain, "Heterodyne detection of ultrasound from rough surfaces using a double phase conjugate mirror" *Appl. Phys. Lett.* **67**, 3251 (1995).
- 18.B. Pouet, S.Breugnot, P. Clémenceau, "An innovative interferometer for industrial laser ultrasonic inspection", *Review of Progress in Quantitative NDE*, Colorado school of mines, Golden, Colorado, July 25-30 (2004).
- 19.M.P. Petrov, S.I. Stepanov, G.S. Trofimov "Non-stationary EMF in the heterogeneously illuminated photoconductor" *Pis. Zh. Tekh. Fiz.* **12**, 916 (1986).
- 20.<http://www.lasson.com/EMF500.htm>.
- 21.A.S. Murfin, R.A.J. Soden, D. Hatrick, R.J. Dewhurst "Laser-ultrasound detection systems: a comparative study with Rayleigh waves" *Meas. Sci. Technol.* **11**, 1208 (2000).
- 22.S.I. Stepanov "Sensitivity of non-steady-state photo electromotive force-based adaptive photodetectors and characterization techniques" *Appl. Opt.* **33**, 915 (1994).
- 23.P.V. Mitchel, G.J. Dunning, S.W. McCahon, M.B. Klein, T.R. O'Meara, D.M. Pepper "Compensated high bandwidth laser ultrasonic detector based on photo-induced EMF in GaAs" *Review of progress in QND* **15A**, 2149 (1996).
- 24.N.A. Korneev, S.I. Stepanov "Non steady-state photo-EMF in thin photoconductive layers" *IEEE J. Quantum. Electron.* **30**, 2721 (1994).
- 25.www.bossanovatech.com
- 26.www.tecnar.com
- 27.www.polytec.com
- 28.M. Dubois, A. Moreau, M. Milizer, J.P. Bussiere "Laser ultrasonic monitoring of phase transitions in steels", *Scr. Mater.* **39**, 735 (1998).
- 29.M. Paul, W. Arnold "Materials characterization at high temperatures using laser ultrasound", *Materials science and engineering*, 87 (1993).
- 30.M. Dubois et al "Laser ultrasonic measurement of microstructure evolution during metal processing", *Intelligent processing of high performance materials*, 11-1 (1998).
- 31.J.H. Tweed, C.B. Scruby "On-line monitoring of metallurgical structure: summary of PMP6 program " *AEAT* **2310**, 16 (1997).
- 32.J.P. Monchalain "Progress towards the application of laser ultrasonics in industry" *Review of progress in QNE* **12**, 495 (1993).
- 33.S. Kenderian, B. Djordjevic, R. Green, D. Cerniglia "Laser-air, hybrid ultrasonic testing of railroad tracks", *US Patent 6945114* (2005).
- 34.*NewScientist.com*, 22 August 2006.
- 35.S.A. Nielsen, A.L. Bardenshtein, A.M. Thommesen, B. Stenum "Automatic laser ultrasonics for rail inspection", *Sensor & NDE Innovation division*, Brøndby, Denmark.
- [36] www-civa.cea.fr.
- [37] B. Marchand, J. Decitre, O. Casula, *Recent Developments of Multi-elements Eddy Currents Probes*, WCNDT 2008.

6.2 APPENDIX 2 – SICOR

The information included here on the Speed Induced Current on Rail (SICOR) method has been included as in May (just prior to the completion of this document) the WP4.4 group became aware of the technique being explored by Deutsche Bahn. Included here is a technical overview of the method written by Rohmann, the German technology developer. No attempt has been made to compare the method, either physically or experimentally, with the techniques which have so far been considered within WP4.4, however, the group believe that this method is worthy of note, particularly as DB, a WP4.4 partner are actively working with it.

SICOR®

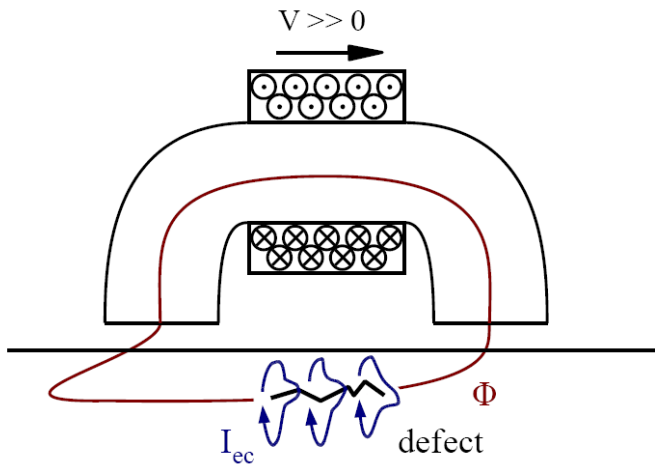
SICOR – Inspection of Railroad Rails in their Track

SICOR is an abbreviation that is made up of the first letters of the English words „Speed Induced Current On Rails“. It describes a new inspection method of railroad rails in their track for open and hidden defects up to a damage depth of approximately 10mm.

The SICOR-principle is based on several physical effects. The effect that magnetic field that penetrate conducting materials may cause electrical currents in those materials is common knowledge. It is referred to as magnetic induction. It requires that the magnetic flux Φ changes within the material or simply put that the density of the lines of magnetic flux in the material changes. In the case before us there are two possibilities for this. Either the strength of the magnetic fields itself changes directly or the conducting material moves in relation to the magnetic field. The second possibility applies to. The magnetic field and the material, in this case the rail, are moving in relation to each other. A dc electromagnet is moved across the rail at a known speed v and a distance d . The movement of the magnet excites magnetic currents I_{ec} inside the conducting material which in turn generate a magnetic field that is acting in the opposite direction of the penetrating magnetic field. Due to the movement of the magnet the magnetic field in the metal and therefore also the field of the induced currents is moved and distorted in such a manner that it is “trailed behind the magnet”. Below this effect is referred to a magnetic trailing effect. Illustration b) depicts this effect.

In addition it is also known that cracks or material separations in metallic materials hamper the formation of induced currents. With SICOR-method magnetic separations such as cracks even in lower layers still affect the formation of the currents depending on how deep the magnetic field penetrates the material. The induced currents in turn generate a magnetic field that as previously mentioned acts in the opposite direction of the original field and interferes with it. Therefore the interaction between both magnetic fields is responsible for a reactive modulation of the resulting total field, if there is a defect in the material.

Another effect has to be taken into consideration to understand the SICOR-method. It is known that magnetizable materials can only be magnetized to a certain degree which depends on the composition of the material and its prior treatment. The material cannot be magnetized beyond this limit the



physical effects. The effect that magnetic field that penetrate conducting materials may cause electrical currents in those materials is common knowledge. It is referred to as magnetic induction. It requires that the magnetic flux Φ changes within the material or simply put that the density of the lines of magnetic flux in the material changes. In the case before us there are two possibilities for this. Either the strength of the magnetic fields itself changes directly or the conducting material moves in relation to the magnetic field. The second possibility applies to. The magnetic field and the material, in this case the rail, are moving in relation to each other.

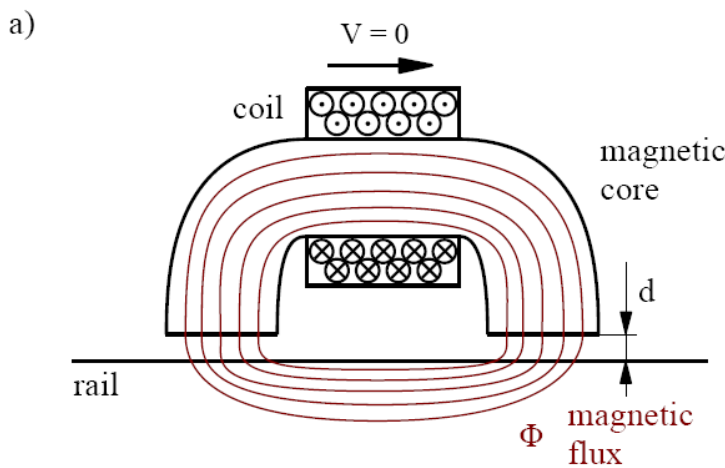


Illustration 1 a) DC electromagnet in a stationary status

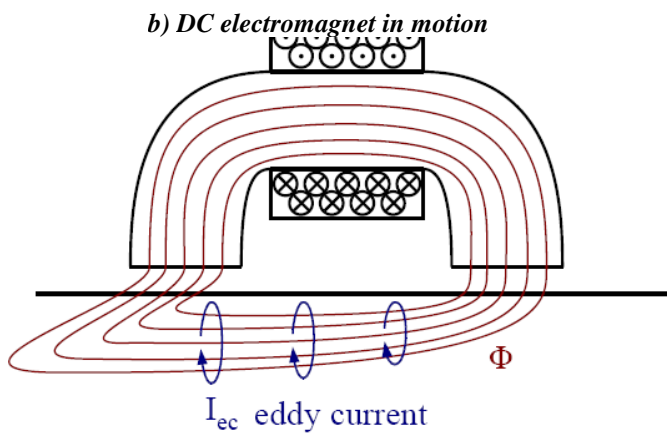


Illustration 2 Influence of a defect on the eddy current

composition of the material and its prior treatment. The material cannot be magnetized beyond this limit the

so-called magnetic saturation and it responds to additional magnetization as if it were not magnetic at all. This means that additional magnetic fields are able to penetrate deeper into magnetically saturated materials. Therefore it depends on the one hand on the strength of the magnetization and on the other hand on the relative speed in interaction with the material defects within the material how much the „rail“ material may be magnetized respectively saturated locally. When using traditional eddy current technology there are limits to detecting deep hidden defects, because there is not always a direct coupling between the eddy current field that is generated by the probe and the defect – even when using bias magnetization. For this reason special probes are used for the SICOR-inspection. These probes evaluate the relative permeability μ_r in a small measuring volume and thus react to the modulation of the resulting total field along the surface of the test specimen that is caused by a defect.

The complex interaction of these effects clearly shows that the SICOR-method is no traditional eddy current inspection, no eddy current inspection using premagnetization and no leakage flux measurement.

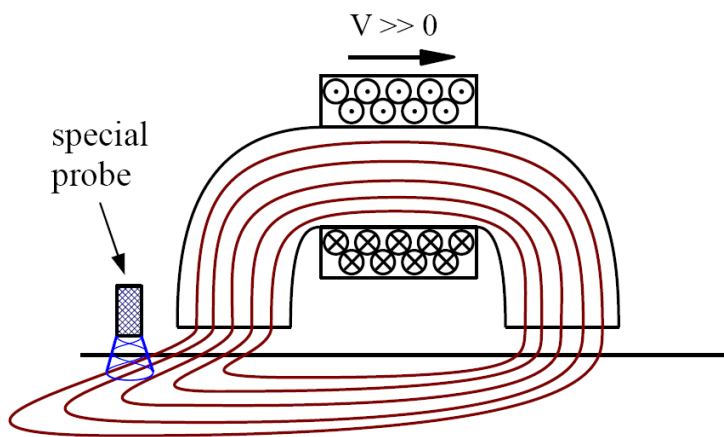


Illustration 3 Position of the special probe in the trailed filed

As the various effects and interactions that distinguish the SICOR-method only occur in a moving system, the SICOR-method cannot be used for static inspections.

Since early 2008 practical tests have been carried on a test stand in Kirchmöser in cooperation with Deutsch Bahn (DB). For this purpose the running surface of a wheelset was adapted to a typical rail profile and equipped with open (OF) and hidden (VF) reference defects as well as various types of squats. The hidden defects were placed at various depths, but always have the same height respectively depth of $d = 10\text{mm}$. The test set-up as shown in illustration 4 permitted initial measurements in the „magnetic trailing field“ under conditions close to reality. These measurements were carried out with ROHMANN's latest eddy current test instrument ELOTEST PL500 that is especially suitable for this application due to its high dynamics and digitizing rate in the low-frequency range. When looking at the rotation of the wheel the measured signals

may be clearly matched to the individual defects. Additionally, the hidden and open defects can be determined based on their depth and may be clearly distinguished based on their signal amplitude and phase position in the impedance plane. Likewise squat-defects were unambiguously identified with regard to the extent of their damage. The tests indicated that the depth resolution of the SICOR-method shows a direct function of the length of the magnetizing yoke, the travelling speed and the applied magnetization. Future joint plans by ROHMANN GmbH and DB propose applying the SICOR-method to actual rails and validating it. This involves mainly the more sophisticated evaluation of squat-defects.

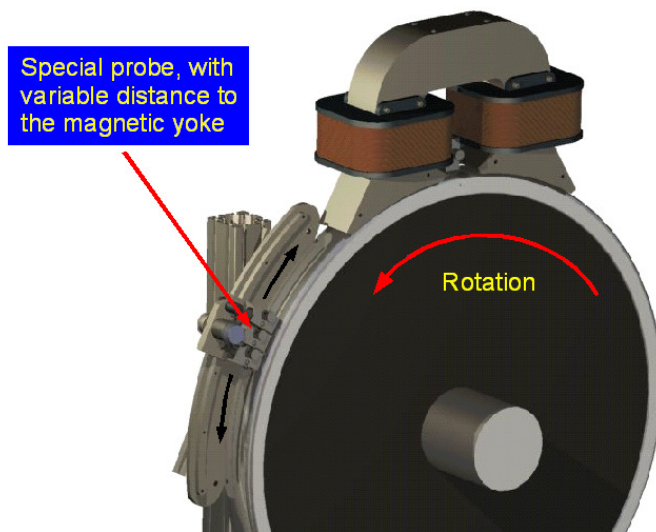


Illustration 4 Test set-up on a DB-test stand in Kirchmöser

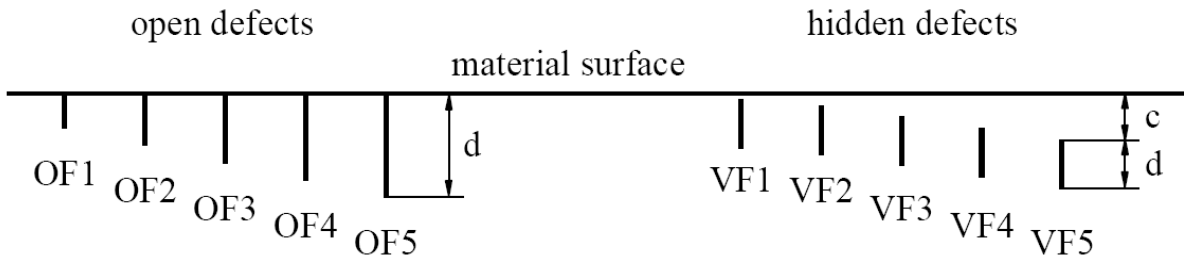


Illustration 5 Drawing of the open and hidden test defects

open defects	depth d	hidden defects	remaining wall thickness c
OF 1	8mm	VF 1	1mm
OF 2	11mm	VF 2	2mm
OF 3	14mm	VF 3	4mm
OF 4	17mm	VF 4	6mm
OF 5	20mm	VF 5	8mm

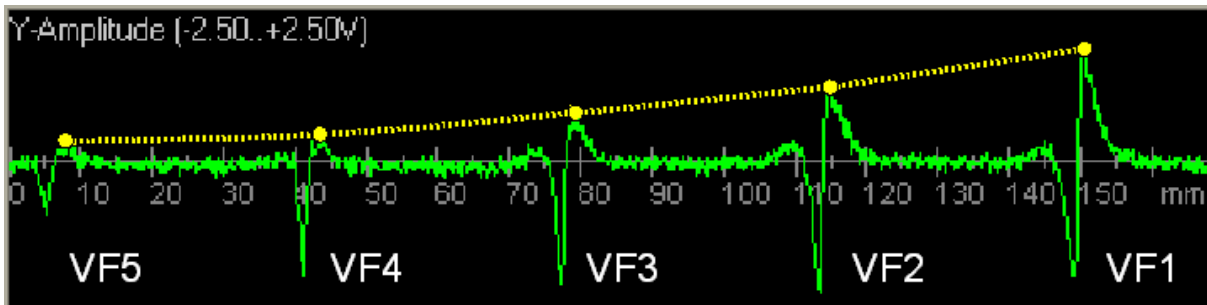


Illustration 6 Typical test result yielded by open defects at a speed of 50kph and 16A magnetizing current (recorded by the ELOTEST PL500 eddy current test instrument)

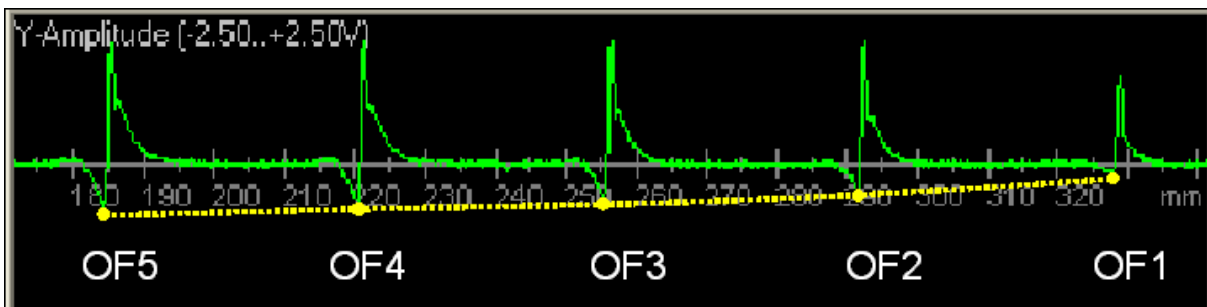


Illustration 7 Typical test result yielded by hidden defects at a speed of 50kph 16A magnetizing current (recorded by the ELOTEST PL500 eddy current test instrument)

ROHMANN GmbH has already applied for a patent for the process described above. You should therefore pass on the confidential information before you only after having consulted ROHMANN GmbH.

6.3 APPENDIX 3– ProRail requirements list

(The requirements list is drawn from document “Operational requirements & wishes: For a detection / inspection system for raildefects for railways” elaborated by Fred Velderman from ProRail as a contribution to WP 4.4)

- 2.1 The detection/inspection system must comply with the EN 13848, as far as applicable.
- 2.2 The detection/inspection system must measure non destructive and contactless.
- 2.3 The area of the railhead that must be measured by the RCF detection/inspection system is specified in the next figure:
The yellow-zone is the zone where surface cracks (like head checks and squats) appear.
The blue-zone is the zone covered by ultrasonic testing.

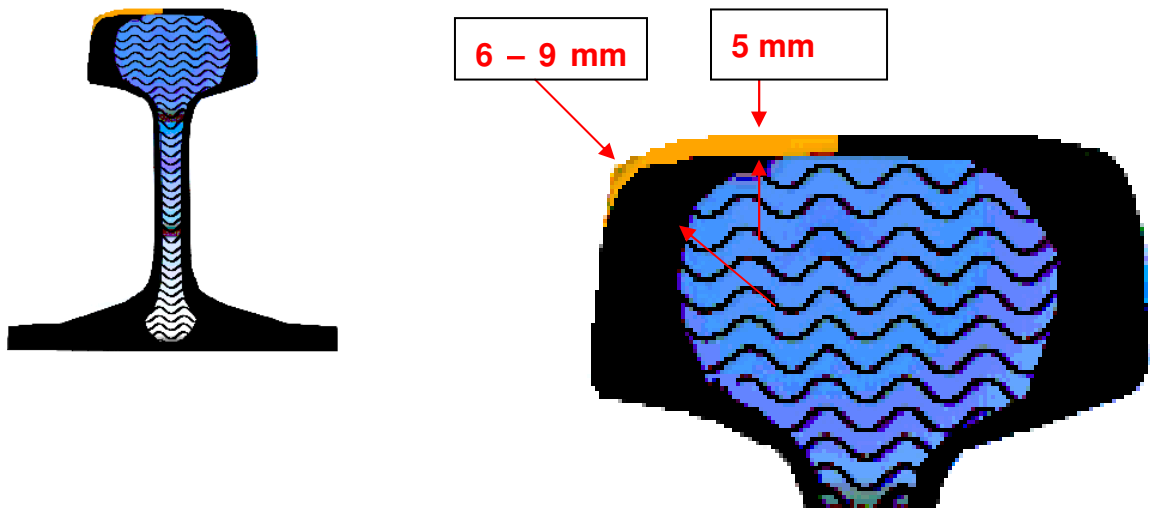


Figure 127 – Rail zones for ultrasonic inspection

- 2.4 The accuracy of the measures crack-depth must be $\pm 1,0$ mm
- 2.5 The hit-rate of the detection/inspection system must be: 95 %
- 2.6 Of the total measured kilometers of track the reviewed percentage must be minimal 95%
- 2.7 The reproducibility of the detection/inspection system must be:
 - for the crack depth : $\pm 1,0$ mm. (concerning the size)
 - for the crack location : ± 100 mm
- 3.1 Operation of the detection/inspection system must comply with the health and safety legislation of the relevant country.
Operation of the detection/inspection system must comply with the health and safety regulations of the relevant railway company.

- 3.2 The detection/inspection system must be operatable within:
Air temperature : -20°C up to $+40^{\circ}\text{C}$
Rainfall : up to 27 mm/h
Fog : visibility must be + 100 m.
Snowfall : visibility must be + 100 m.
Snowcover : when the rail is covered measuring is not possible.
- 3.3 The sensors of the crack detection system which are situated very near to the railhead must fit in the structure gauge of clearance around the railhead.
- 3.4 The detection/inspection system must be suitable to measure the following rail profiles : 46E3
54E1
60E1
- 3.5 The detection/inspection system must be able to measure new and worn railhead profiles.
The detection/inspection system must be able to measure around rail joints.
- 3.6 The detection/inspection system may not influence the signaling system / train management system (ERTMS).
- The detection/inspection system may not influence the energy supply system that is part of the rail frame components (1500V to 25 kV).
- The detection/inspection system must comply to safety level SIL 4 conform Cenelec norm NEN-EN 50129
- 3.7 The detection/inspection system installed in a measuring train must comply with the signalling system of the railway company.
- The detection/inspection system installed in a trolley must not interfere with the signalling system of the railway company.
- 3.8 WISH rather than REQUIREMENT: The minimum speed for inspecting left and right rail in a track is 40 km/hour. For switches: The maximum time for inspecting a 1/15 switch is 15 minutes. The inspection of a switch should take place in two passes: one for each direction of the switch.
- 3.9 Maintenance (repair of adjust of exchange the sensors / system) in case of a breakdown may take maximal 30 minutes.
- Worn parts (such as sensors) must be exchangeable within 15 minutes.
- The calibration must be executable in a simple manner by a third party on the basis of an explicit calibration protocol.
- 3.10 The power supply of the detection/inspection system must be sufficient for continue inspection during 8 hours.
- The time necessary to get the RCF detection/inspection system ready for use may be 15 minutes.

4.1 The results of the measurements must be in a digital protocol.

The results of the measurement must be importable in a decision support system as for instance IRISsys so that they can be matched with the results of other measurements (for instance ultrasonic and geometrical measurements).

4.2 The position of detected defects must be tagged and retraceable.

Locations must be specified by :

- line code or line name (for example : 023 Amsterdam-Utrecht)
- track name (for example: track G)
- kilometer (for example: km 123.345)
- left , right rail or both rails (for example : RR or LR)

Locations must be recorded in the for the railway company specific system

The position of the detected defects must be recorded in GPS-coordinates with an accuracy of ± 3.0 m. (EN 13848-1 par 5)